NOVEL LUMINESCENT NANOSENSORS AND THEIR APPLICATIONS IN QUANTIFYING AND MONITORING ANALYTE GRADIENTS IN BACTERIAL BIOFILMS

by

Megan P. Jewell

A thesis submitted to the Faculty and Board of Trustees of the Colorado School of Mines in partial fulfillment of the requirements for the degree of Doctor of Philosophy (Chemical Engineering).

Golden, Colorado

Date _____

Signed: _____
Megan P. Jewell

Signed: _____
Dr. Kevin J. Cash
Thesis Advisor

Golden, Colorado

Date _____

Signed: _____
Dr. Anuj Chauhan
Professor and Department Head
Department of Chemical and Biological Engineering

ABSTRACT

Bacterial biofilms are complex, heterogeneous communities of bacteria encased in an extracellular matrix of polysaccharides, DNA, protein, and other biopolymers. Biofilms are ubiquitous across bacterial species and are believed to be the default mode of growth for many species. Opportunistic pathogens such as *Pseudomonas aeruginosa* form biofilm infections in the airways of cystic fibrosis patients and in wounds. Because of reasons such as this, investigating the ways different metabolites are utilized is crucial to our understanding, use, and control of these complex microbial communities. In this work, polymeric oxygen nanosensors are presented as both a research tool for quantifying oxygen dynamics with enhanced resolution as well as a potential clinical tool for evaluating antibiotic efficacy *in vitro.* These nanosensors can determine 3-dimensional oxygen variation through both space and time and monitor metabolic changes from administration of antibiotics. Potassium-selective nanosensors that utilize the unique photomechanism of triplet-triplet annihilation upconversion are also detailed as a potential solution to overcome issues of signal crosstalk in imaging-based monitoring. These upconversion sensors have a potassium-specific response with a response midpoint of 0.82 mM K^+ and no measurable crosstalk with typical downconversion probes (demonstrated with a GFP-producing bacterial biofilm). The development of these nanosensors provides new tools and methods to investigate the biochemical dynamics within bacterial biofilms. The oxygen nanosensors let us monitor 4D dynamics for oxygen whereas prior approaches have been limited in spatial and temporal resolution, and the upconversion sensors allow for monitoring of ion dynamics without interference from traditional fluorescent reporters in these biological systems.

TABLE OF CONTENTS

LIST OF FIGURES

LIST OF TABLES

ACKNOWLEDGEMENTS

I would like to thank my advisor, Professor Kevin Cash, for his support and mentoring during my graduate school career. Dr. Cash encouraged the pursuit of topics I found interesting and worthwhile, and allowed me to turn some of those ideas into parts of the work presented here. He also generously tolerated some of my more half-baked ideas and solutions as well. In addition, I have to thank the past and present members of the Cash Lab - specifically Dr. Anne Galyean, Dr. Mark Ferris, and undergraduate students Alex Dailey, Meredith Greer, Tabitha Kalin, and Tony Tien – for their advice and help over the past few years. I would also like to thank the members of my thesis committee, Professors Susanta Sarkar, Keith Neeves, Joseph Samaniuk, and C. Josh Ramey for their guidance and input. I must also thank the Chemical and Biological Engineering Department here at Colorado School of Mines for their support during my time here.

I would like to thank my parents, Garry and Karen Jewell, my brother Matt, and my "big sis" Kacee for their love and support throughout the years. Thank you for never building fences around me, and for not rolling your eyes too hard when I decided that 4 years of college wasn't enough. I want to thank my Colorado family, Nicholas, Ron, and Velvet Rorrer for all of their support, kindness, and reassurance that graduate school doesn't last forever. A tremendous thank you to my boyfriend Matthew Osmond for being a steadfast shoulder to lean on, a wonderful sounding board, and my best friend. I'm glad you do the dishes.

Finally, I wish to thank Children's Hospital Colorado for the grant that supported part of this work, the Colorado Office of Economic Development and International Trade, and the Chemical and Biological Department at the Colorado School of Mines for financial support.

CHAPTER 1

AN INTRODUCTION TO BIOANALYTICAL SENSORS

In research and in clinical environments, important decisions and conclusions are made based on analytical data collected from sensors. Sensors comprise a large field of tools that produce a signal in response to an analyte.[1] A sensor is distinct from a label or probe, both of which are commonly used in biomedical research and diagnostics. To be a sensor, the device must detect something in its environment and report it out in a quantitative manner. The focus of this work is bioanalytical sensors, which are chemically-based sensors that are used in a biological environment. In order to be a relevant and useful tool, a sensor should be reversible, sensitive, selective, biocompatible, and respond faster than the analyte changes.[2]

All sensors consist of a recognition element and a transduction element, which can be either the same component in the device (coupled) or separate components (decoupled).The most common signal transduction methods in biological research are mechanical, electrical, and optical. Mechanical sensor mechanisms such as microcantilevers,[3] acoustic wave sensors,[4] and gravimetric sensors[5] have all been well-reviewed elsewhere[6] and are not the focus of this work.

One common group of sensors that have been well studied are electrochemical sensors, which report a change in an electrical property (e.g. potential, current, resistance) in response to a change in analyte.[2, 7-9] For *in vitro* purposes these often take the form of microelectrodes, whereas implantable devices are available for *in vivo* applications. One major issue with electrochemical sensors such as these are their invasiveness. Microelectrodes are disruptive to the *in vitro* environment they are measuring in, especially when measuring gradients.[8, 10, 11] Implantable

devices often invoke a foreign body response that prevent the device from being able to sense anything.[2]

The primary alternative to electrochemical reporters are optical sensors. Optical sensors are appealing because they are minimally invasive, easier to miniaturize, and can be read remotely, all of which make it easier to study systems at small scales.[2, 12] Optical sensors are characterized by the change of an optical property (e.g. absorbance, fluorescence emission, decay time) in response to an analyte.[12] Examples of well-known optical sensors range from traditional colorimetric pH indicators to ELISAs for proteins and antibodies, and more recently genetically encoded indicators like GCaMP.[13]

There are several ways to group sensors based on their design. One such grouping is based on whether the measured quantity is converted directly into a reportable signal.[14] The recognition element is, as the name suggests, the part of the device that recognizes the analyte of interest, and the transduction element is what turns that recognition into a quantifiable output. In a sensor with a coupled mechanism (also known as a direct sensor), the component that recognizes the analyte also produces the observed output. In the examples provided, the observed output is a change in an optical property such as luminescence or absorption. The majority of direct sensors detect physical properties such as pressure, temperature, or humidity, although there are a select few chemical species/properties that can be sensed directly. For example, many examples of optical sensors that measure pH and oxygen directly exist.[12, 15] These are the two most common chemical species for which direct sensors exist, and much indirect sensing relies on direct mechanisms for them. pH sensing is discussed in more detail below as it underlies the ionophore-based method.

There are many mechanisms by which oxygen may be sensed directly, such as electrochemical (the Clark electrode), pressure-based, and optical. Within optical methods are

absorbance or chromogenic indicators and luminescence indicators.[16] Common examples of absorbance-based indicators are hemoglobin or methylene blue. Luminescent indicators are a much larger class of oxygen-sensitive probes that range from organic dyes to metal-ligand complexes to conjugated polymers.[15] Nearly all oxygen sensors (including those detailed in Ch 3 and Ch 4) are based on the luminescence quenching properties of oxygen. Luminescence quenching is caused by the physical collision between the excited state luminescent probe molecule and molecular oxygen, which occurs naturally in a triplet electronic state. Collisional quenching is reversible, nondestructive of the probe, and only change the intensity or decay time of the indicator. It is governed by the Stern-Volmer equation, which relates luminescent intensity and oxygen concentration in the following linear manner:

$$\frac{I_0}{I} = 1 + K_{SV}[O_2] \tag{1.1}$$

Where I_0 and I are the intensities of the probe in either the absence or presence of oxygen, K_{SV} is the Stern-Volmer constant, and $[O_2]$ is the concentration of oxygen (can be expressed in concentration units or as partial pressure). The Stern-Volmer constant is often found experimentally for a given system, as it is a function of the indicator lifetime, the diffusivity and permeability of the indicator's support matrix (e.g. a polymer or solvent), and potential quenching by other components of the oxygen sensor (e.g. a plasticizer).

In addition, species such as metal organic frameworks (MOFs) show ability to distinguish between volatile organic compounds such as ethanol and acetone.[17] Materials like these have potential as direct sensors, but often suffer from a lack of selectivity (e.g. responding to H_2O or CO_2 when sensing O_2).

Because of issues such as limited analyte choice, most optical bioanalytical sensors contain a recognition element that is distinct from the signal transduction element. These sensors are said

to have a decoupled mechanism and are known as indirect or complex sensors. Indirect sensors comprise the majority of sensors designed for biological targets. These include materials such as metal and metal oxide nanoparticles and films that have been surface-functionalized with a biological recognition element such as aptamers, peptides, and enzymes.[18, 19]

One subset of optical sensors that takes advantage of the selectivity and generalizability of decoupled mechanisms are ionophore-based optical sensors (IBOS).[12] IBOS use an indirect sensing scheme in which the extraction of the analyte (e.g. cation) by an ion-selective ligand (ionophore) causes the release of an equivalent number of protons to maintain electroneutrality. The protons released are donated by a proton carrier (pH sensitive indicator) whose optical properties change with protonation degree. These components are all contained in a hydrophobic plasticized polymer matrix that can be cast as a film or emulsified into nanoparticle form. Figure 1.1 is a visual schematic of this process.

Each of the three labeled steps in Figure 1.1 corresponds to an equilibrium equation below:

$$zH^+(aq) + I^{z+}(org) \overset{K_{exch}^{H^+I^{z+}}}{\longleftrightarrow} zH^+(org) + I^{z+} \tag{1.2}$$

$$nL(org) + I^{z+}(org) \overset{\beta_{L_nI^{z+}}}{\longleftrightarrow} L_nI^{z+}(org) \tag{1.3}$$

$$zIndH^+(org) \overset{K_a}{\leftrightarrow} zInd^0(org) + zH^+(org) \tag{1.4}$$

In all equations, z is the charge of the target cation, H^+ is a proton, I^{z+} is the target cation, L is the ionophore, n is the complexing coefficient of the ionophore, Ind is the pH indicator, (aq) and (org) refer to the aqueous and organic phases, and K_a, $\beta_{L_nI^{z+}}$, and $K_{exch}^{H^+I^{z+}}$ are equilibrium

constants (acid dissociation constant of the pH indicator, ionophore binding constant, and ion exchange constant, respectively).

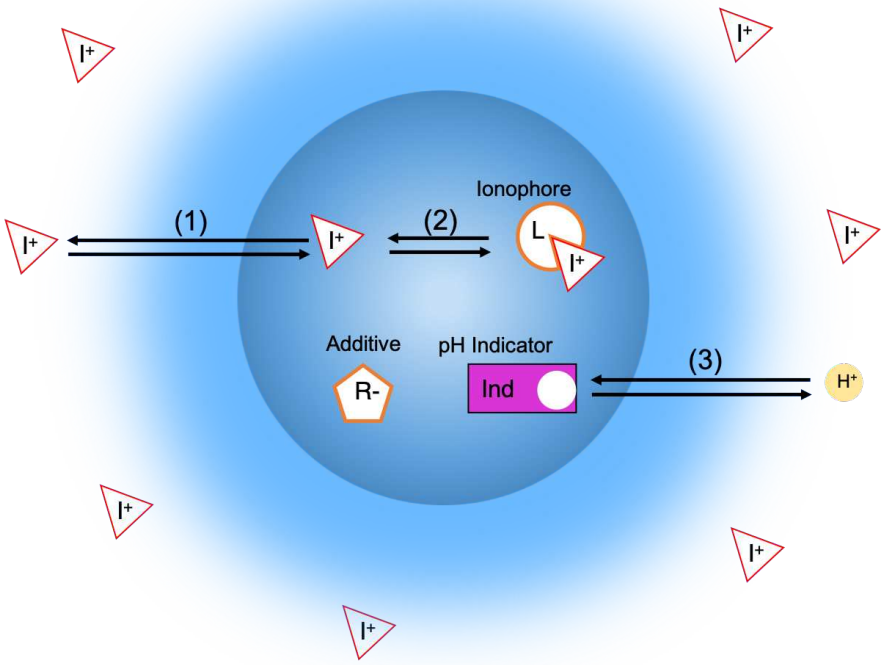

Figure 1.1 Schematic representation of the ionophore-based exchange process. Here, an ion (I^+) is extracted by an ion-selective ionophore (L). In order to maintain electroneutrality, protons are extracted from the sensor phase. This causes the visible change in the pH-sensitive indicator (Ind). R- is the charge-balancing additive.

From these equilibrium equations, others[12, 20] have shown that the target cation activity (a_I) can be related to the degree of protonation of the pH indicator and the degree of protonation can then be related to the fluorescence of the sensor by Equations 1.5 and 1.6:

$$a_I = \frac{(a_H)^z}{zK_{overall}} \left[\frac{R_T - (1-\alpha)Ind_T}{\left\{L_T - \frac{n}{z}[R_T - (1-\alpha)Ind_T]\right\}^n} \right] \left(\frac{\alpha}{1-\alpha}\right)^z \tag{1.5}$$

$$F = (1-\alpha)\left(F_{prot} - F_{deprot}\right) + F_{deprot} \tag{1.6}$$

In these equations, a_I is the target cation activity, a_H is the activity of the proton in the aqueous phase, z is the charge of the target cation, $K_{overall}$ is the overall exchange constant, R_T is the total additive concentration, Ind_T is the total amount of pH indicator in the organic phase, L_T is the total amount of ionophore in the organic phase, n is the complexing coefficient of the ionophore, and (1-α) is the protonation degree of the indicator. F, F_{prot}, and F_{deprot} are the fluorescence intensity of the sensor, the fluorescence intensity of the protonated state of the pH indicator, and the fluorescence intensity of its deprotonated state, respectively.

These IBOS nanosensors have been applied to both *in vitro*[31,32] and *in vivo*[22,23] applications. These fluorescence signals can be plotted against the log of the analyte concentration (Figure 1.2) to produce a sigmoidal response curve that can be fit to the 4-parameter equation:

$$I = \frac{Bottom+(Top-Bottom)}{\left(1+10^{(logEC50-log[K^+])*HillSlope}\right)} \tag{1.7}$$

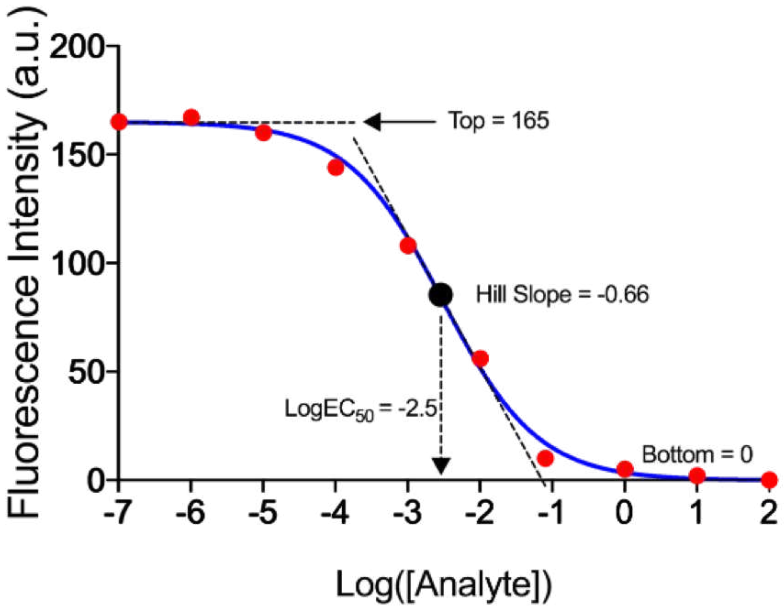

Figure 1.2 An example dose-response curve where the fluorescence of the nanosensor is recorded over a range of analyte concentrations on a log scale.

Here, the four parameters used to fit the curve are the bottom (minimum fluorescence intensity), top (maximum fluorescence intensity), Hill Slope (slope of linear range), and $\log EC_{50}$ (the log value of the concentration at which the sensor has gone through 50% of its response).

In this work, the optical sensor mechanisms discussed in this introduction are used to study biochemical gradients within biofilms of *Pseudomonas aeruginosa*, an opportunistic human pathogen known to cause chronic and recalcitrant biofilm infections. This expands and improves upon work that has been done previously on using bioanalytical sensors to image and quantify dynamics within bacterial biofilms, which are reviewed in Chapter 2. These methods are crucial to both expanding our understanding of microbial communities as well as providing avenues for the development of new clinical tools to aid in better control of the serious issues that can arise from human-biofilm interaction.

CHAPTER 2

A REVIEW OF CHEMOSENSORS AND BIOSENSORS FOR MONITORING BIOFILM DYNAMICS

This chapter is modified from a paper currently pending submission[1]

2.1 Introduction

Biofilms are aggregates of bacteria that exist within a self-created matrix of various extracellular polymeric substances.[21] These aggregates exist in nearly all ecosystems, from the human gut and mouth to salt marshes to water pipes. In all of these systems, biofilms play a key role in the physical and chemical functions of the system. For example, in the oral microbiome biofilms called plaques can cause cavities and gum disease.

There have been many literature reviews that collect information related to this review. Much work has been done on the detection of and imaging of biofilms. These have been reviewed by Fischer et al.[22] and Neu and Lawrence,[23] respectively. The use of biofilms as sensors themselves has also been extensively discussed elsewhere.[24, 25]

Bacteria that exist within biofilms exhibit properties that differ in many critical ways from their planktonic counterparts. Microbes that are situated closely to one another are capable of behaviors that a single cell or even free-floating cells of multiple species are not capable of, such as resistance to antibiotics, survival in an aerobic or anaerobic environment, or evasion of host immune response. One difference that is incredibly important to the global healthcare community is the enhanced antimicrobial resistance of biofilms. Many of the World Health Organization's (WHO) high priority multidrug-resistant pathogens are known to be biofilm-forming human

[1] Pending submission

colonizers. This, along with environmental biofilm ubiquity, places an urgency and importance on the understanding of biofilm mechanisms and behaviors.

There are many challenges for accurate and dynamic sensing in biofilms. A major issue is the spatial and sample-to-sample heterogeneity of biofilms. Because biofilm growth and structure are affected by considerations such as environmental nutrient availability, inoculum age, and presence of multiple species, the phenotypes and behavior exhibited by individual biofilms of nominally identical strains can be widely varied.[26, 27]

In addition, biofilms contain phenotypically distinct subpopulations[28] that are often physically segregated along with various channels for the movement of nutrients, oxygen, and other important molecules.[29] Thus, sensors that can only capture limited spatial information are unable to fully capture the internal environment of the biofilm and risk missing crucial dynamics. Invasiveness of sensors is another issue related to spatial considerations. Many sensors require insertion into the established biofilm to make measurements or consume the target analyte as part of the sensing mechanism. This can be disruptive of the process being monitored, especially in cases such as monitoring signaling molecules, which are often short range and diffusion limited.

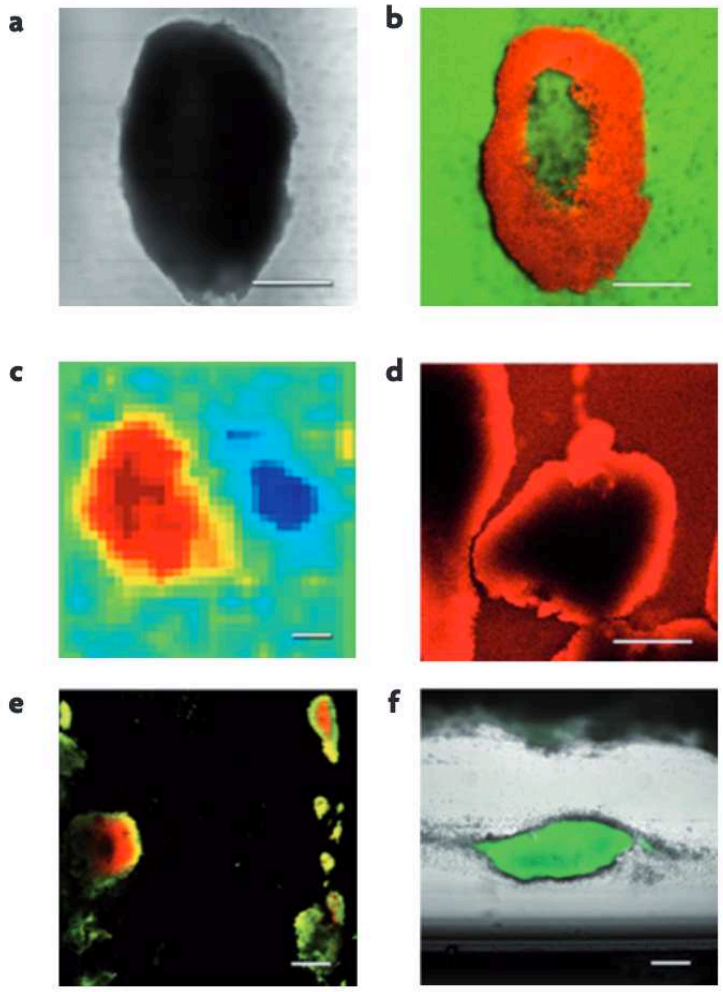

Figure 2.1 A recurrent theme in the study of microbial biofilms is their inherent microscale heterogeneity. The physical, chemical and biological heterogeneity that can develop even in a single-species biofilm is shown. All of these patterns were imaged using the same reactor system — glass capillary flow cells containing *Staphylococcus epidermidis* biofilms. In each panel, the colour or greyscale variation reflects the heterogeneity for a different property. a) Transmission-mode confocal scanning laser microscopy shows an isolated cell cluster (dark grey) surrounded by fluid (light grey). b) The same cell cluster as in a) imaged using fluorescence-mode confocal scanning laser microscopy (biomass, red; fluid, green) shows a hollow centre. c) Magnetic resonance microscopy image that shows measurements of water velocities and reveals complex flows; red and blue indicate velocities that are in opposite directions. d) Confocal scanning laser microscopy image showing chemical gradients that developed during a transient diffusion study which imaged the progressive inward diffusion of the red fluorescent dye rhodamine B (a video of the entire sequence can be viewed on Montana State University's Center for Biofilm Engineering website); e) An immunofluorescence image of cells that were pulse labelled with bromodeoxyuridine. DNA synthetic activity (green) was shown to be localized at the periphery of cell clusters (red). f) Confocal scanning laser microscope image taken during treatment with chlorine. This disinfectant permeabilizes cells at the periphery of cell clusters (dark grey), but leaves more deeply embedded cells (green) intact. The scale bars represent 100 microns. Figure and caption adapted from Stewart et al.[26]

2.2 Oxygen Sensing

Molecular oxygen is perhaps the most commonly sensed analyte in biofilms. This is because of its common use by organisms in their metabolism, especially among some of the most heavily utilized microbial model organisms such as *E. coli, B. subtilis,* and *P. aeruginosa.* Even in studies involving anaerobes, being able to identify regions of hypoxia and anoxia has importance.[30]

2.2.1 Microelectrodes

The Clark electrode (a membrane-covered platinum electrode)[31] remains the exemplar for electrode detection of oxygen.[32] It has been in use for many decades, sometimes predating the use of the word biofilm, such as in work by Whalen and Bungay.[33] Many groups still use the oxygen microelectrode to monitor oxygen in biofilms as it is a well-established, well understood, and commercially available technology. Beyenal et al. have used oxygen microelectrodes to monitor the effects of hyperosmotic agents on *S. aureus* biofilms.[34] Additionally, the group has used oxygen microelectrodes to monitor photosynthetic activity in *Chlorella vulgaris* algal biofilms.[35]

Other groups have attempted to improve upon the oxygen microelectrode. Moya et al.[36] produced a microfabricated sensor array for profiling oxygen in biofilms. This array of MEMS-produced microelectrodes was able to provide spatial information as well as real-time measurement of dissolved oxygen profiles in a heterotrophic aerobic biofilm.

2.2.2 Planar optodes

Planar optodes are an increasingly popular method of monitoring oxygen, especially in imaging applications. These are polymeric films impregnated with oxygen-sensitive luminescent probes that can be applied to surfaces to provide 2-dimensional spatial information at the external side of the investigation volume as well as continuous temporal information. Commercially

available oxygen-sensitive films along with bench-scale designs have been extensively reviewed elsewhere.[16]

Moβhammer et al. developed a system for simultaneous ratiometric imaging of pH and oxygen in a photosynthetic microbial mat.[37]An optode-based method was used by Staal and coworkers to image 2-dimensional O_2 dynamics in a membrane-fouling simulator.[38] This approach was able to be used ratiometrically without the need for an additional reference dye. The same group also produced a thin film optode of iridium (III) coumarin complexes suspended in polystyrene that measures oxygen dynamics using lifetime-based microscopic imaging.[39] Thar et al. have used ruthenium-based and metalloporphyrin-based planar optodes to simultaneously image oxygen and GFP-producing kanamycin resistant *P. putida* biofilms. Sasaki et al. produced an oxygen-sensitive thin film for monitoring a *P. aeruginosa* biofilm that also used bacteria (specifically *Photobacterium kishitanii* suspended in sodium alginate) as the dissolved oxygen probe.[40] A major limitation presented by planar optodes is that they are limited to external 2-dimensional spatial information. As most biofilms are on the order of 10-100 μm thick and exhibit depth-related oxygen gradients, this method can only provide partial information of oxygen dynamics, although it is a relatively fast and simple-to-use method in comparison to methods that can provide more detailed information.

2.2.3 Nano/micro-particles

In an attempt to overcome many of the problems associated with microelectrodes and planar optodes, much attention has been paid to micro- and nano-sized oxygen sensitive particles. Most of the work has been focused on engineered tissue scaffolds,[41, 42] but several groups have leveraged these technologies in bacterial biofilms as well. Acosta et al. immobilized an oxygen-sensitive ruthenium complex and a reference probe to the surface of silica microparticles. These

silica microparticles were then infused into a live *S. aureus* biofilm and used to image oxygen within the biofilm.[43] Jewell and coworkers have also implemented nanoparticle oxygen sensors to measure oxygen within biofilms of *P. aeruginosa*.[44] These polymeric nanoparticles are smaller than the bacteria and easily incorporated into the biofilm matrix, providing a detailed method of examining oxygen gradients and dynamics.

2.3 pH sensing

Another important and commonly measured analyte is pH. Most biological processes are sensitive to pH, and in bacterial biofilms pH is dynamically altered by these processes. pH is of particular interest to those studying oral biofilms, which reduce the pH near the tooth surface and cause dental caries.

2.3.1 Microelectrodes

Much like with oxygen, pH microelectrodes are a well-established technology with many of the same advantages and limitations. Joshi et al. use pH changes as an analogue of metabolic interactions between *S. mutans* and *S. gordonii* in an artificial hydrogel biofilm.[45] The biofilms are monitored with a 25 μm microprobe and using this data the authors were able to generate a 2D spatial map of pH microenvironment. Bause et al. developed an iridium-based pH sensor for monitoring biofilms and liquid cultures.[46] They cite iridium oxide's faster response, wide pH range, and biocompatibility as improvements over other pH electrodes.

2.3.2 Nanoparticles and probes

In order to probe pH changes at the biofilm-tooth interface, Parvinzadeh Gashti and coworkers demonstrated a microfluidic platform with pH imaging.[47] Silver core-silica shell nanoparticles decorated with FITC were immobilized on the surface of the PDMS microfluidic device and tested under a variety of conditions before being used to monitor *Streptococcus*

salivarius biofilms. Schlafer et al. improve upon the use of fluorescent dye C-SNARF-4 to ratiometrically map pH by demonstrating its use for 3-dimensional mapping as opposed to just 2-dimensional mapping.[48] The methods for using this dye to map extracellular pH in biofilms is provided in a JoVE article by the same authors.[49] Dige and coworkers use this method to monitor pH in dental biofilms collected from patients as they are provided sucrose or starved of it.[50] Guo et al. utilize a relatively new technology, pH-sensitive green fluorescent proteins (pHluorins) to investigate acid production by oral biofilm species *Streptococcus mutans.*[51]

2.4 Temperature and heat

Production of heat and the subsequent change in temperature are often used as an analogue for metabolic changes in bacterial biofilms. There have been several instances of dynamic thermal monitoring in bacterial biofilms.

In order to simultaneously monitor biohydrogen production and the resulting temperature change caused by this production, Chen et al. designed fiber Bragg grating sensors.[52] These sensors recorded a change of approximately 1.1°C in a biofilm of 165 μm thickness. By monitoring the phase and amplitude shifts in a thermistor-monitored heater, Reyes-Romero et al. were able to monitor the evolution of *Enterococcus faecalis* biofilms over the course of several hours.[53]

Instead of monitoring temperature changes, the Maskow group uses chip-calorimetry to monitor the eradication of biofilms with bacteriophages[54] and antibiotics.[55] This method can provide information such as cell-specific heat production during infection and enduring persister cell activity.

2.5 Ions

Cations and anions play many different roles within biological systems, from electron acceptors to signaling. De Beer and coworkers improved on nitrite microelectrodes in order to

monitor biofilms in complex environmental samples and *in* situ in operating bioreactors such as those found in wastewater plants.[56] Biofilms of species such as *Rhodobacter ferrooxidans* are capable of oxidizing various heavy metals such as iron and copper. Hao et al. utilize fluorescent probes for Fe^{3+}, Cu^{2+}, Zn^{2+}, and Hg^{2+} to monitor heavy metal ion sorption into the extracellular polymeric substance of *R. ferrooxidans* biofilms.[57] Iron acquisition and storage plays an important role in biofilm survival. Shumi and coworkers using a ferric chemosensor in a microfluidic device to spatially map the distribution of ferric ions in *S. mutans* biofilms.[58] There is also emerging interest in the use of cations such as potassium by biofilms as electrochemical signaling elements. With this increased interest have come the use of both potassium-sensitive dyes[59] and genetically encoded fluorescent ion biosensors.[60]

2.6 Other analytes

There have been chemosensors and biosensors used in biofilms to sense a wide variety of molecules other than those listed above. These other analytes include signaling molecules such as homoserine lactone, cyclic di-GMP, electron acceptors like fumarate and acetate, H_2O_2, and even more generic targets such as redox potential and metabolic activity.

N-acyl homoserine lactone (HSL) is an important quorum sensing molecule in bacterial biofilms. Das et al. use a rhodamine derivative-Cu^{2+} complex to spatially resolve HSL production in *P. aeruginosa* and *S. aureus* biofilms.[61] Struss and coworkers demonstrate a colorimetric bacterial cell-based sensor for detecting HSL that are dried onto filter paper for ease of use.[62]

Another important signaling molecule is cyclic di-GMP. There have been several examples of RNA-based biosensors for c-di-GMP, both fluorescent[63] and electrochemical.[64] Dippel et al. have also demonstrated a c-di-GMP biosensor based on a bioluminescence resonance energy transfer mechanism.[65]

Both fumarate and acetate function as terminal electron acceptors in biofilms. Microelectrode sensors for both have been demonstrated for measuring depth profiles of fumarate[66] and acetate[67] depth profiles in *Geobacter sulfurreducens* biofilms.

Scanning electrochemical microscopy, in addition to its use in pH detection, has also been used to map hydrogen peroxide concentration[68] and redox-active pyocyanin[69] across a biofilm in 3-dimensional space. Redox potential in biofilms has also been investigated using on-line Raman spectroscopy[70] and a fluorescent redox dye.[71]

Beyond these analytes, there has been some work in monitoring the dynamics of general metabolic activity (usually associated with growth) in biofilms. Ibarlucea et al. use nanowire sensors to monitor both growth and antibiotic response.[72] Ishiguro and coworkers use the dye resazurin, which is converted into the fluorescent molecule resorufin in the presence of bacterial metabolites, to monitor the metabolic activity of various periodontopathic bacteria.[73] Fiber optic sensors were used by Zhong et al. to monitor both microalgal biofilm growth and phenol degradation in a *Chlorella vulgaris* biofilm.[74] Paredes and coworkers integrate label-free microelectrode biosensors into 96-well plates as a method for monitoring the growth of biofilms of *S. aureus* and *S. epidermidis.*[75]

Because of the ubiquity of bacterial biofilms in the natural environment and infectious disease, there is much interest in studying the dynamic behaviors within these microbial communities. Sensors for analytes within biofilms must be able to contend with large variations in spatial structure and phenotype while still being able to capture crucial dynamics with limited disruption of the biofilm. Much work has been done in the field of sensing in 3-dimensional biological constructs, but this chapter has been a review of selected works that attempt to meet or improve upon this criteria for sensing specifically in bacterial biofilms.

CHAPTER 3

LUMINESCENT NANOSENSORS FOR RATIOMETRIC MONITORING OF THREE-DIMENSIONAL OXYGEN GRADIENTS IN LABORATORY AND CLINICAL *PSEUDOMONAS AERUGINOSA* BIOFILMS

This chapter is modified from a paper published in *Applied and Environmental Microbiology*[1]

Megan P. Jewell,[2] Anne A. Galyean,[3] J. Kirk Harris,[4] Edith T. Zemanick,[4] and Kevin J. Cash[5]

3.1 Abstract

Bacterial biofilms can form persistent infections on wounds and implanted medical devices and are associated with many chronic diseases, such as cystic fibrosis. These infections are medically difficult to treat, as biofilms are more resistant to antibiotic attack than their planktonic counterparts. An understanding of the spatial and temporal variation in the metabolism of biofilms is a critical component toward improved biofilm treatments. To this end, we developed oxygen-sensitive luminescent nanosensors to measure three-dimensional (3D) oxygen gradients, an application of which is demonstrated here with *Pseudomonas aeruginosa* biofilms. The method was applied here and improves on traditional one-dimensional (1D) methods of measuring oxygen profiles by investigating the spatial and temporal variation of oxygen concentration when biofilms are challenged with antibiotic attack. We observed an increased oxygenation of biofilms that was consistent with cell death from comparisons with antibiotic kill curves for PAO1. Due to the spatial and temporal nature of our approach, we also identified spatial and temporal inhomogeneities in

[1] Reprinted with permission. © American Society for Microbiology, *Appl. Environ. Microbiol.* 85, 2019, e01116-19.
[2] Primary author and Ph.D. Candidate
[3] Co-author, postdoctoral researcher. Obtained initial results.
[4] Co-author, collaborating researcher.
[5] Corresponding author and Ph.D. advisor

the biofilm metabolism that are consistent with previous observations. Clinical strains of *P. aeruginosa* subjected to similar interrogation showed variations in resistance to colistin and tobramycin, which are two antibiotics commonly used to treat *P. aeruginosa* infections in cystic fibrosis patients.

Biofilm infections are more difficult to treat than planktonic infections for a variety of reasons, such as decreased antibiotic penetration. Their complex structure makes biofilms challenging to study without disruption. To address this limitation, we developed and demonstrated oxygen-sensitive luminescent nanosensors that can be incorporated into biofilms for studying oxygen penetration, distribution, and antibiotic efficacy—demonstrated here with our sensors monitoring antibiotic impacts on metabolism in biofilms formed from clinical isolates. The significance of our research is in demonstrating not only a nondisruptive method for imaging and measuring oxygen in biofilms but also that this nanoparticle-based sensing platform can be modified to measure many different ions and small molecule analytes.

3.2 Introduction

While the bulk of bacterial understanding has come from planktonic bacteria, where bacteria grow independently in solution, natural biofilm growth is "a major mode of microbial life".[76] The biofilm microenvironment contains three-dimensional (3D) chemical gradients, and this chemical heterogeneity is associated with complex physiological heterogeneity with the potential to influence various pathogenic and antimicrobial-resistant behaviors.[21, 26] *Pseudomonas aeruginosa* is the most common infectious pathogen in the lungs of patients with cystic fibrosis.[77] Chronic infection typically results in biofilm formation, which advances lung damage and often leads to respiratory failure.[78] Unfortunately, treatment of *P. aeruginosa* infections can be difficult due to natural antibiotic resistance.[79] There is frequently a lack of correlation between planktonic

antibiotic susceptibility tests and biofilm-based infections.[80] Thus, the ability to observe the internal biochemical microenvironment as antibiotics alter the biofilms would provide useful information for researchers. Spatial heterogeneity exists in other biological systems as well. Other biofilms, such as those found in pipes[81] and the natural environment,[82] all exhibit spatial heterogeneity where the ability to measure metabolites, such as oxygen, would be beneficial. Sulfate-reducing bioreactors, a passive wastewater treatment approach, show spatial heterogeneity in metabolites and community distribution.[83] Models of the human trabecular meshwork[84] and intestinal crypts[85] display similar levels of heterogeneity that would also benefit from a way to investigate and understand complex 3D environments. While chemical sensors are an advancement in the investigation of biofilms, they have been limited to measuring pH gradients,[45, 86] oxygen,[33, 38, 86, 87] or specific metal ions.[57, 88] Microelectrodes have also been used to measure spatial distributions of gradients and concentrations in biofilms for a wide range of analytes.[10, 26, 33, 56, 89-91] However, the spatial resolution is limited by the physical tip size, and the insertion of the microelectrode directly into the biofilm intrinsically disturbs the biofilm physical structure.[92] Furthermore, this approach becomes difficult for frequent sampling and prohibitive for measurements spanning a heterogeneous sample. The majority of microelectrodes are only capable of producing one-dimensional (1D) measurements in the z-dimension. Kenney et al.,[93] Acosta et al.,[42] and others[94-96] have detected and mapped gradients of oxygen and pH in two-dimensional (2D) and 3D cell culture scaffolds. In order to capture temporal dynamics in addition to 2D spatial information, planar oxygen optodes are also used, but the information they provide is limited to the optode-biofilm interface.[39, 97, 98] However, 2D approaches cannot capture depthwise changes in samples, and other 3D options require particles that are large and potentially invasive. Oxygen is an important analyte of interest because it can be used as a measure of metabolic activity.[34]

Acosta et al. demonstrated the use of silica microparticles for measuring oxygen in bacterial biofilms.[43] Many attempts to image or measure other analytes in biofilms have resulted in two-dimensional maps, limiting spatial understanding.[37-39, 97] Nanosensors are a technology which can overcome the limitations of current measuring methods by enabling continuous spatiotemporal monitoring of analyte concentrations in growing biofilms. These nanosensors are a tunable family of sensors that are designed for uninterrupted monitoring of *in vitro* or *in vivo* physiological parameters. The nanosensors are highly plasticized hydrophobic polymer nanoparticles which respond to changes in analyte concentration by altering their optical properties.[99] These nanosensors (~200nm diameter) are useful in locations like biofilms where other techniques, like microelectrodes, fail due to size. Like microelectrodes, nanosensors have been developed for a variety of analytes, including pH, ions like K^+ and Li^+, and small molecules and metabolites, like oxygen and histamine. These polymer nanosensors can be fabricated with a variety of fluorescent emitters, such as quantum dots,[100] carbon dots,[101] or organic dyes.[102] In addition, sensor response properties, including dynamic range and response midpoint, can be controlled through sensor formulation.[103] In this study, we report the development of our oxygen-sensitive luminescent nanosensor (O_2NS) technology for monitoring oxygen spatiotemporal gradients and demonstrate its utility by monitoring the metabolism of both laboratory and clinically derived *P. aeruginosa* biofilms and the biofilm response to antibiotic attack.

3.3 Materials and Methods

3.3.1 Materials

High-molecular-weight poly(vinyl chloride) (PVC), bis(2-ethylhexyl) sebacate (BEHS), tetrahydrofuran (THF), dichloromethane (DCM), and phosphate-buffered saline (PBS) were purchased from Sigma-Aldrich (St. Louis, MO, USA). Platinum (II) meso-

tetra(pentafluorophenyl)porphine (PtTFPP) was purchased from Frontier Scientific (Logan, UT, USA). 1,2-Dipalmitoyl-sn-glycero-3-phosphoethanolamine-N-[methoxy(polyethylene glycol)-750] ammonium salt in chloroform (PEG-lipid) was purchased from Avanti Polar Lipids (Alabaster, AL, USA). 4-Di-16-ASP (4-[4-(dihexadecylamino)styryl]-N-methylpyridinium iodide) (DiA) was purchased from Thermo Fisher Scientific (Waltham, MA, USA).

3.3.2 Nanosensor fabrication

A total of 30 mg of polyvinyl chloride (PVC) was weighed into a 2-ml vial and combined with 66µl of BEHS. In a separate vial, 5 mg of Pt(II) meso-tetra(pentafluorophenyl)porphine (PtTFPP) and 0.2 mg 4-Di-16-ASP (4-[4-(dihexadecylamino)styryl]-N-methylpyridinium iodide) (DiA) were dissolved in 500µl of tetrahydrofuran (THF). The THF and dissolved dyes were then added to the PVC/BEHS mixture and vortexed for 1 min until all solids were dissolved. A total of 750µl of dichloromethane (DCM) was then added to the vial, and the mixture was vortexed thoroughly. The optode cocktail was then stored at 4°C until use. To fabricate nanosensors from the optode cocktail, 2 mg PEG-lipid (80µl of a 25-mg/ml solution in chloroform) was dried in a 4-dram scintillation vial and then resuspended in 5 ml of PBS (pH 7.4) with a probe tip sonicator (Branson Digital Sonifier 450; Branson Ultrasonics Corporation, Danbury, CT) for 30 s at 20% intensity. A total of 125µl of the optode cocktail mixture was injected into the PBS/PEG-lipid solution under probe tip sonication (3 min, 20% intensity). Following sonication, excess polymer was removed by filtration via a 0.22-µm syringe filter (Pall Corporation, Port Washington, NY).

3.3.3 Nanosensor characterization

Oxygen-sensitive nanosensors were calibrated on an Avantes AvaSpec-ULS2048L StarLine versatile fiber-optic spectrometer (Apeldoorn, the Netherlands) with a 100-µm slit width. O_2NSs were sealed in an airtight screw top quartz cuvette (Starna Cells, Atascadero, CA), and the

oxygen content of the sample was altered by bubbling a compressed air/N_2 mixture through the cuvette for 30 min. The O_2NS sample was then excited with a 450-nm laser diode, and spectra were collected at various concentrations of oxygen. A linear regression of ratiometric signals was performed in GraphPad Prism 7 software (La Jolla, CA). Values were fit to the Stern-Volmer relationship describing collisional quenching of an excited species where the quencher Q is molecular oxygen. In the equation below, I_f^0 is the ratiometric fluorescence intensity in the absence of oxygen, I_f is the ratiometric fluorescence intensity at the given concentration of oxygen [Q], and K_{SV} is the Stern-Volmer constant.

$$\frac{I_f^0}{I_f} = 1 + K_{SV}[O_2] \tag{3.1}$$

The ratiometric mode is a method of internal self-calibration that is made possible by the comparison of emission at two different wavelengths.[104] In this case, I_f refers to the ratio of the oxygen-sensitive fluorescence intensity of PtTFPP at 650 nm and the insensitive fluorescence intensity of DiA at 585 nm (I_{650}/I_{585}). This allows the sensors to overcome limitations, such as concentration variation or heterogeneity of the local microenvironment, which will impact both fluorescent peaks similarly, while oxygen will only impact one of the peaks.[105, 106] O_2NSs were calibrated in alginate hydrogels on a Zeiss LSM780 confocal microscope. Hydrogels with embedded O_2NS were fabricated according to Fletcher et al.[107] Briefly, 0.5 ml of 3 wt% alginate was mixed with 200µl of O_2NS and 40µl of 0.1 M $CaSO_4$. The mixture was cast between two glass plates to produce hydrogels of 380µm thickness, which was measured with a micrometer. The resulting hydrogels were placed into chamber slide wells and covered with 500µl of PBS. Images were taken under ambient conditions (21% O_2 or 6.65 mg/liter dissolved O_2 at the lab elevation of 5,750 ft above sea level) and under oxygen deficiency (0% O_2 or 0 mg/liter dissolved O_2). Chamber

slide wells were deoxygenated with 10 mM glucose and 2 IU/ml glucose oxidase, as described by Baumann et al.[108] The average intensities of the biofilms in the images at 0% O_2 and 21% O_2 were then used in a linear regression to determine the Stern-Volmer constant K_{SV}. In both calibration scenarios, the intensities of the PtTFPP signal at 650 nm and the intensities of the reference dye (DiA) signal at 585 nm were divided to form a ratiometric signal. The ratiometric signal at 0 mg/liter dissolved oxygen (DO) was then divided by the ratiometric signal at each concentration to create a linear calibration curve. The linear Stern-Volmer relationship between I_f^0/I_f and oxygen concentration was used to fit the calibration data.[109] Image analysis was performed in Matlab using the Batch Image Processor. The image stack was transformed into a 3D array in Matlab with dimensions of 1,024 by 1,024 by the number of slices in the image stack containing 8-bit brightness values (intensity values, 0 to 255). These slices were converted via the Stern-Volmer calibration curve function into DO values in milligrams per liter, which could be extricated and graphed. Dynamic light scattering (DLS), zeta potential via phase analysis light scattering (PALS), and mobility measurements were performed on a Brookhaven zetaPALS instrument with Particle Solutions software v2.2 (Brookhaven Instruments Corporation, Holtsville, NY).

3.3.4 Biofilm construction and growth

3.3.4.1 *P. aeruginosa* PAO1 (ATCC 15692)

Biofilm construction and growth procedures were adapted from methods by Kirchner et al.[110] Briefly, *P.aeruginosa* strains were plated onto Luria Bertani (LB) agar (Sigma-Aldrich, St. Louis, MO, USA) from frozen stocks and incubated at 37°C for 24 h. One colony was pulled and dispersed in 1 ml of LB broth and incubated for 24 h at 37°C. Liquid culture was diluted to an optical density at wavelength of 600 nm (OD_{600}) of 0.05. Biofilms of PAO1were grown statically in a 16.7% vol/vol solution of oxygen nanosensors in PBS mixed with LB broth (Sigma-Aldrich).

A total of 600µl of O_2NS + LB was added to each well of a 4-well LabTek chamber slide and then inoculated with 5µl of liquid *P. aeruginosa* culture at an OD_{600} of 0.05. Chamber slides were placed in a humidity chamber and incubated for 72 h at 37°C.

3.3.4.2 *P. aeruginosa* clinical strains

Respiratory samples collected for clinical care were processed by the clinical microbiology laboratory at Children's Hospital Colorado using standard CF Foundation guidelines for culture. *P. aeruginosa* isolates were frozen and shipped to study investigators at the Colorado School of Mines. All three clinical strains are deidentified and in the manuscript are labeled as clinical strain 1 (CS1), CS2, and CS3. With all three of the provided isolates, we expanded and grew the biofilms as detailed above with the PAO1 samples.

3.3.4.3 Biofilm characterization

Three biofilms of PAO1 were grown as described above, namely, one containing no polymer nanoparticles, one containing polymer nanoparticles with no fluorescent components, and one containing O_2NS. The FilmTracer LIVE/DEAD biofilm viability kit (Thermo Fisher Scientific) was used for biofilm viability. A total of 12µl of SYTO9 green fluorescent nucleic acid stain (3.34 mM in dimethyl sulfoxide [DMSO]) and 12µl of propidium iodide (20 mM in DMSO) were added to 4 ml of PBS, and 400µl of the resulting solution was added to each well of the chamber slide and incubated at room temperature for 15 min in the dark. The solution was then aspirated, and each well was washed 2 times with sterile PBS. A total of 400µl of 10% formalin was added to each well and incubated for 30 min in the dark. Formalin was then aspirated, and each well was washed 2 times with PBS. A final volume of 200µl PBS was added to each well before imaging. Three regions of interest containing the entirety of the biofilm were chosen for

each sample containing no nanoparticles (n=4 images) or containing blank polymer nanoparticles (n=3) or O_2NS (n=3).

3.3.4.4 Antibiotic testing

All antibiotic testing was performed on live biofilm samples that had not been stained or fixed prior to imaging. A total of 10µl of 10 mg/ml tobramycin in PBS was added to the 490µl of PBS already present in the chamber slide well, for a final tobramycin concentration of 4 mg/ml (62). This was administered to each biofilm sample, and images were taken every 5 min for 2 h.

For comparison, a final colistin concentration of 512µg/ml was administered to each biofilm sample in a similar manner, and images were taken every 5 min for 2 h. Here, colistin was administered as colistin sulfate as opposed to the prodrug colistimethate sodium.

3.4 Results

3.4.1 Method development: sensor design and characterization

Figure 3.1a illustrates the sensor mechanism, where at low O_2 concentrations, both the platinum porphyrin [platinum (II) meso-tetra(pentafluorophenyl)porphine (PtTFPP)] and the reference dye (4-[4-(dihexadecylamino)styryl]-N-methylpyridinium iodide) (DiA) luminesce. At higher O_2 concentrations, oxygen collides with the PtTFPP molecule and quenches the luminescence via nonradiative decay. The fluorescence intensity of the platinum porphyrin PtTFPP (650 nm) decreases as the sample is exposed to increasing oxygen up to 21% in a linear manner (Fig. 3.1b). The peak of the DiA reference dye (585nm) remains constant with respect to oxygen concentrations. Physical properties of these nanosensors, as determined by dynamic light scattering (DLS) and phase analysis light scattering (PALS), were an effective diameter of 163.4 ± 1.5 nm, a polydispersity of 0.15 ± 0.02, a zeta potential of -11.5 ± 1.34 mV, and a mobility of -0.90 ± 0.10 µm-s^{-1}/V-cm^{-1}. Values are listed as the arithmetic means and standard deviations. A

Stern-Volmer constant, K_{SV}, that allows for back calculation of oxygen concentration was determined. K_{SV} for the O_2NS was found to be instrument-specific, and thus, the O_2NS was calibrated for each instrument used. The intensities of the PtTFPP signal at 650 nm and the intensities of the reference dye (DiA) signal at 585 nm were divided to form a ratiometric signal. The ratiometric signal at 0 mg/liter dissolved oxygen (DO) was then divided by the ratiometric signal at each concentration to create a linear calibration curve. The linear Stern-Volmer relationship between I_f^0/I_f and oxygen concentration was used to fit the calibration data (Fig. 3.1c), where I_f^0 is the ratiometric fluorescence intensity in the absence of oxygen and I_f is the ratiometric fluorescence intensity at the given concentration of oxygen. Calibration was also performed on the confocal scanning laser microscope used to obtain results from all microscopy experiments. Measurements were taken under ambient conditions (21% O_2 conditions/6.65 mg/liter DO) and 0 mg/liter DO to form a two-point calibration curve (Fig. 3.1d).

As an initial test to determine if sensors function in the biofilm matrix, dead biofilms were imaged before and after deoxygenation with glucose and glucose oxidase. As can be seen in Fig. 3.2, the ratiometric signal increases as the oxygen in the biofilm decreases. These results indicate that the sensors function similarly in the complex matrix of the biofilm in comparison with how they function in solution and in simpler matrices, such as alginate (see Fig. A.1 in the supplemental material).

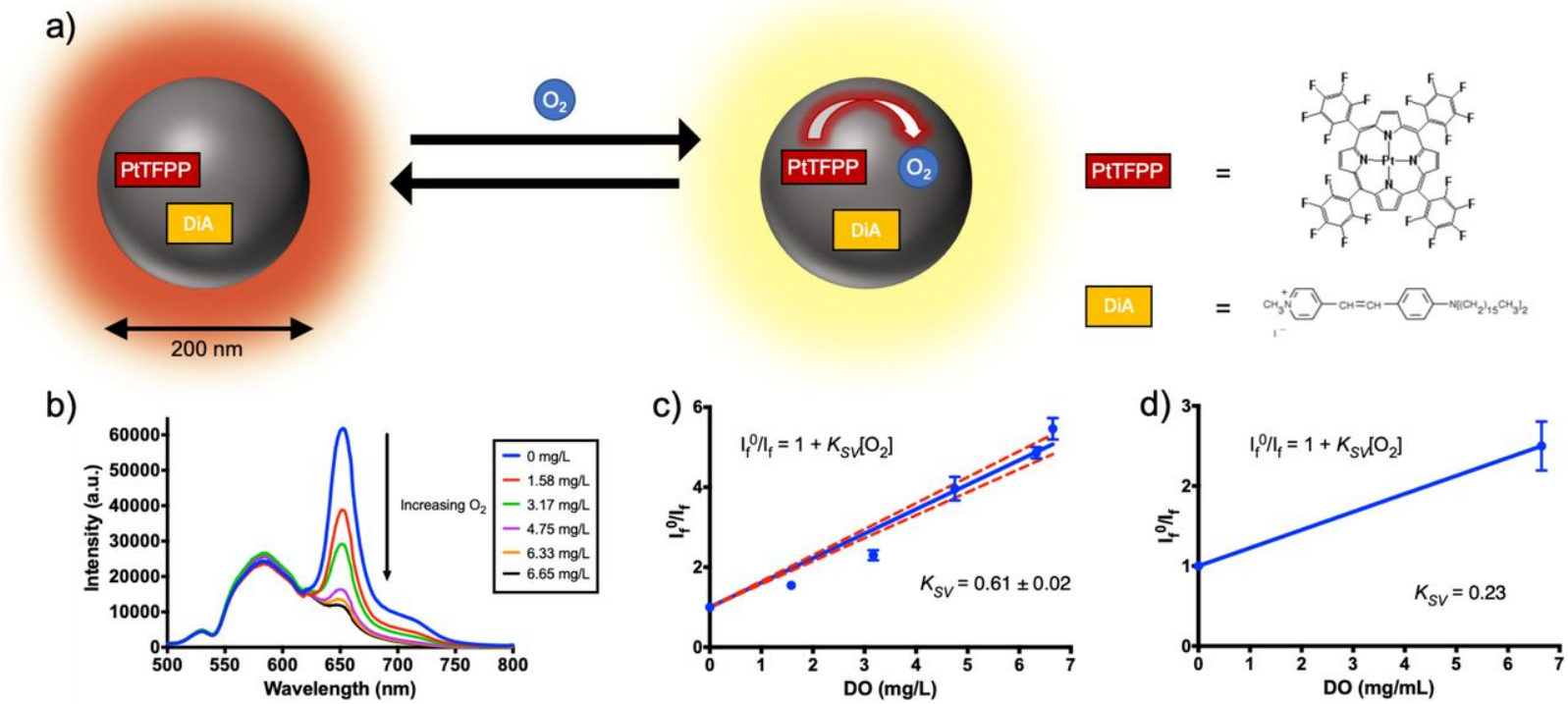

Figure 3.1 (a) Schematic of nanosensor components coloaded into the nanoparticle matrix and luminescence quenching mechanism in response to increasing oxygen concentrations. (b) Fluorescence spectra for ratiometric oxygen nanosensors. Excitation occurs at 450 nm and produces the spectra shown under different oxygen concentrations. As oxygen concentrations increase, the platinum porphyrin peak at 650 nm decreases and the reference peak at 585 nm is insensitive to changes. This ratiometric sensor response allows us to calculate oxygen concentrations without complications resulting from variable nanosensor concentration. Normalized ratiometric calibration curves for oxygen nanosensors demonstrate effective sensing of oxygen concentration changes using both a spectrometer (c) and a confocal microscope (d) (used in remaining figures).

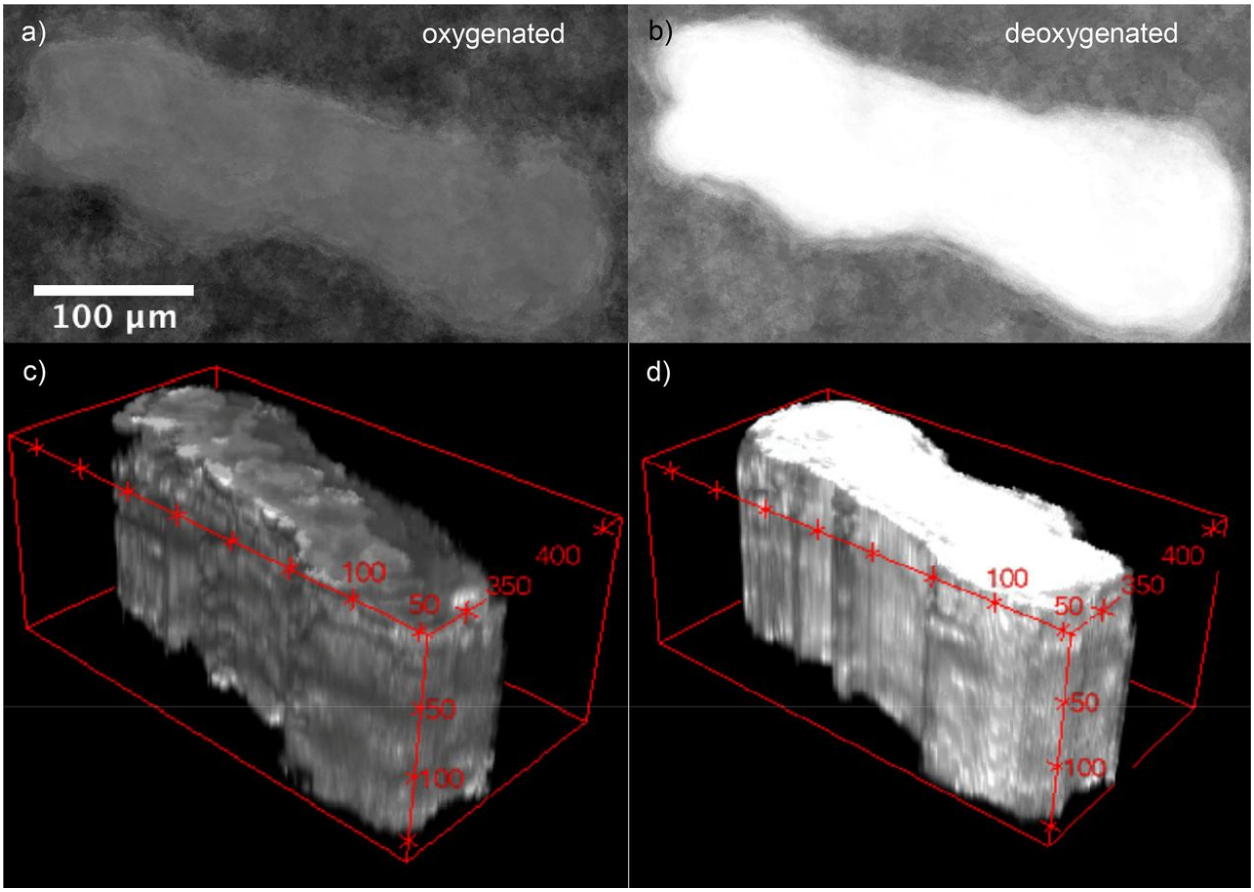

Figure 3.2 Biofilms killed with colistin before (panels a and c) and after (panels b and d) the addition of glucose and glucose oxidase. (a and b) Average ratiometric intensity z-projections of data used to calibrate O_2NS in the confocal microscope. (c and d) The 3D images show that oxygen concentration is uniform through the biofilm. This finding demonstrates that the nanosensors respond to oxygen concentrations as expected even in the complex biofilm environment.

3.4.2 Example application: measuring antibiotic-induced metabolic changes

Ratiometric signal data can be used to render 3D images of biofilms so that their structure can be visualized along with information about oxygen concentration within the biofilm (Fig. 3.3).

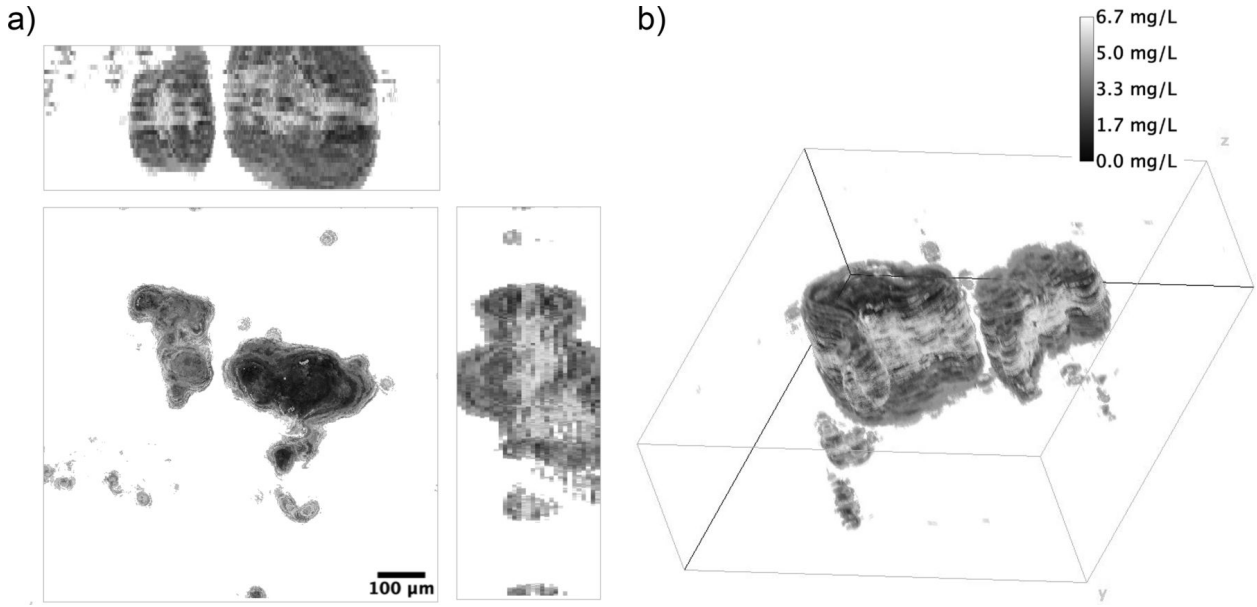

Figure 3.3 The 2D orthogonal (a) and 3D (b) views of a live P. aeruginosa PAO1 biofilm created using ratiometric intensity data. Raw confocal images of the PtTFPP (O_2 sensitive) and DiA (reference) signals were processed and divided in ImageJ to produce a stack of images of the ratiometric intensity that recapitulates oxygen concentration throughout the biofilm.

The 2D projections of the raw 3D images (before ratiometric division) can be seen in Fig. A.2 in the supplemental material. In addition, quantitative information on the oxygen concentration at an arbitrary location within the biofilm can also be determined via Matlab processing and graphed in a manner similar to data obtained from oxygen microelectrodes. This can be seen in Fig. 3.4. At four locations within the biofilm, oxygen concentration values were extricated from the Matlab array and graphed versus depth. There is large variation in oxygen concentration between locations, such as location 3 (a large central area with high DO concentrations) and location 4 (low DO concentrations throughout).

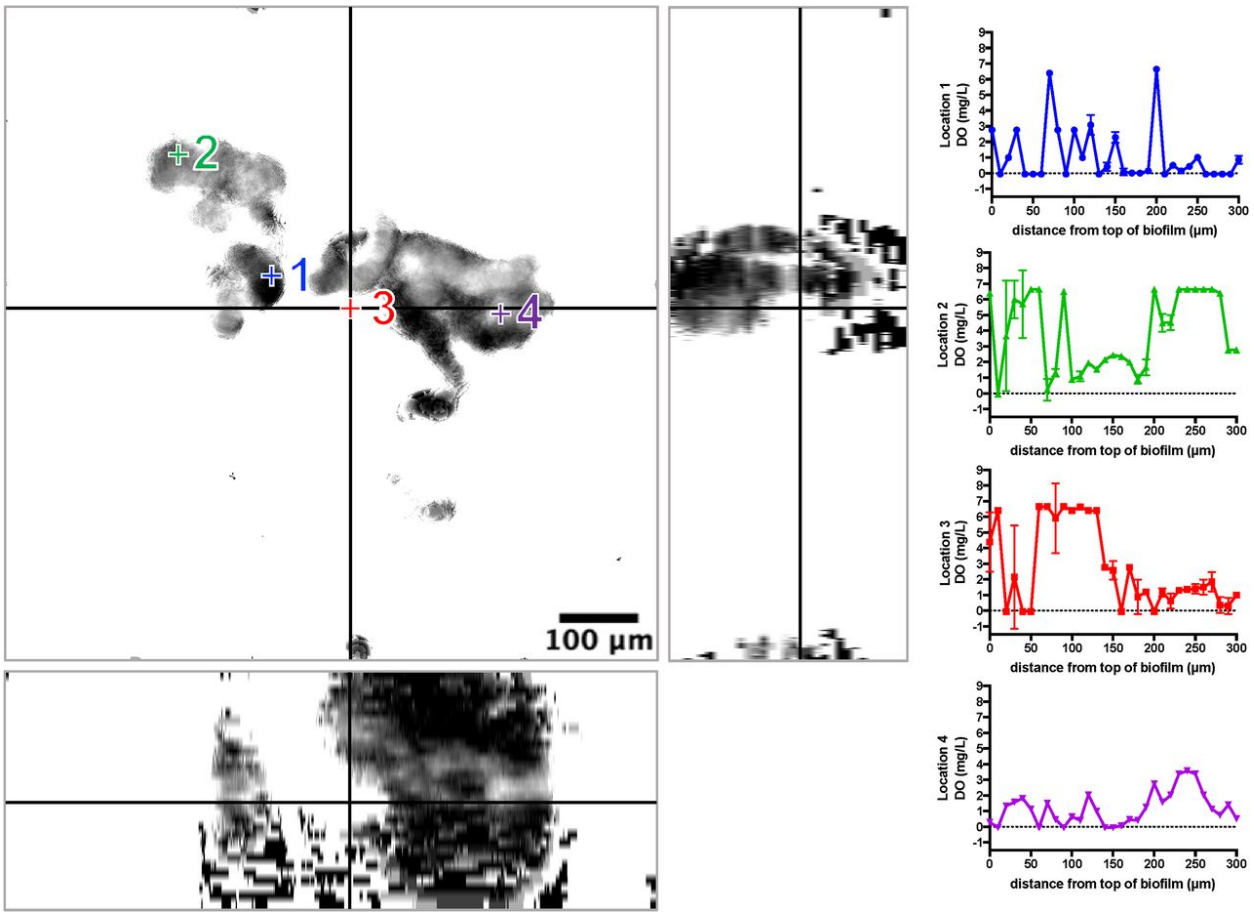

Figure 3.4 Location versus oxygen concentration plot (right) of PAO1 image (left). Four locations across the biofilm were chosen for graphing, and error bars represent standard error of $n = 9$ pixels surrounding the chosen location. The four locations were chosen arbitrarily and show large spatial variation. Location 3, whose representative orthogonal views are shown, has a large gap in the center that has DO concentrations close to those in the surrounding medium. This finding highlights the massive spatial differences in biofilm oxygen concentrations.

The location in the biofilm we chose for temporal analysis (location 4 in Fig. 3.4) has an oxygen concentration of 1 mg/liter before the addition of colistin, with concentrations at or approaching 6 mg/liter at the edges of the biofilm, which can be seen in Fig. 3.5. This finding is consistent with a diffusion limitation of oxygen into the center of the biofilm as the bacteria consume it. As colistin penetrates the biofilm, oxygen concentration also increases, indicating cell death. The center of the biofilm takes the longest amount of time to approach the surrounding oxygen concentration, which can be seen in Movie A.1 in the supplemental material.

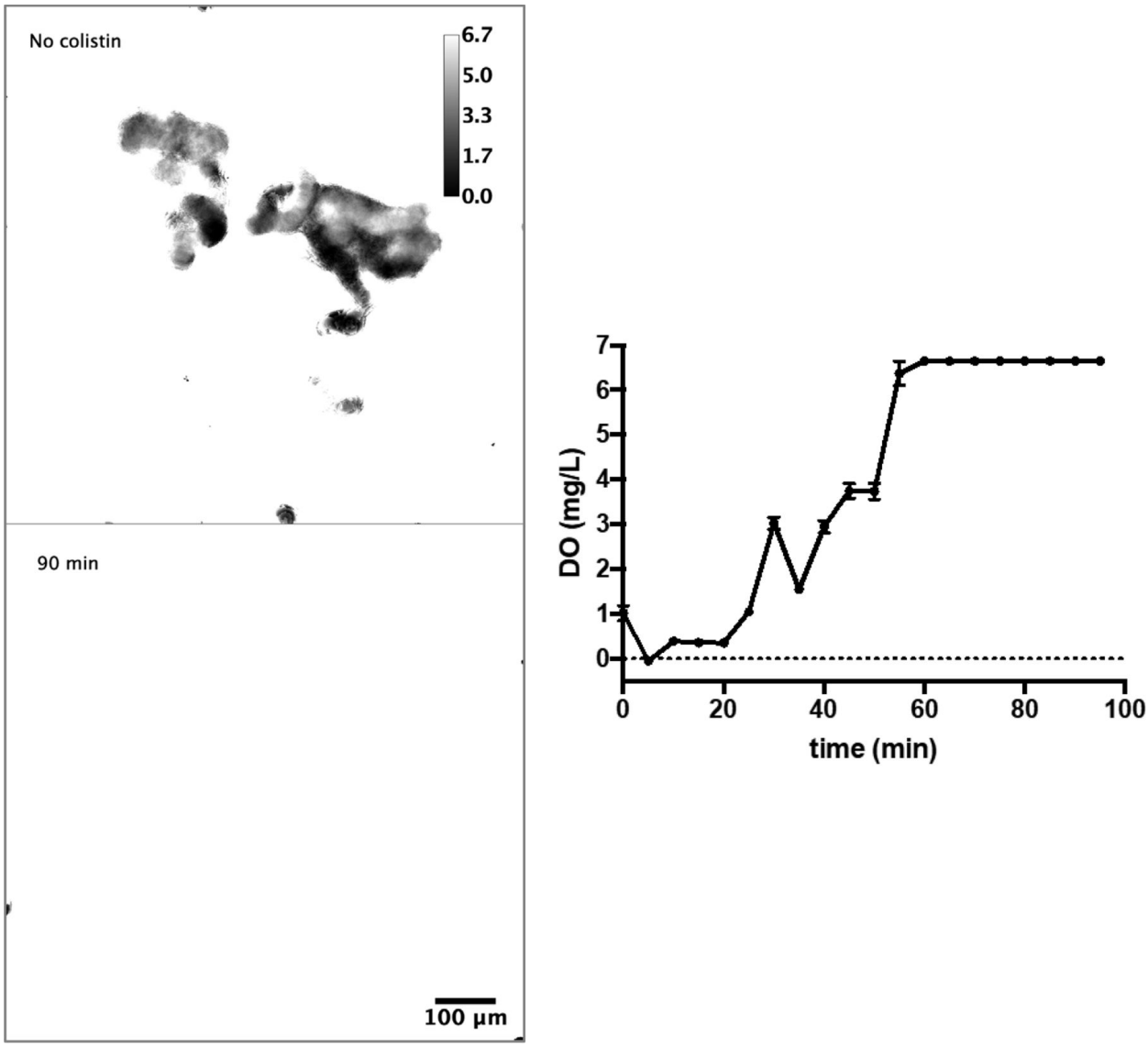

Figure 3.5 Time lapse of oxygen concentration within PAO1 biofilm after the addition of 512 µg/ml colistin. Oxygen concentration within the biofilm reaches ambient values by 60 minutes. Error bars represent a standard error of $n = 9$ pixels surrounding the chosen location.

In clinical strain 1 (CS1), there is an overall higher concentration of oxygen than in PAO1, indicating lower metabolic activity or improved oxygen transport (Fig. 3.6). After the addition of colistin sulfate, the majority of the biofilm reaches an internal oxygen concentration approaching ambient conditions (indicating no metabolic activity) after 30 min.

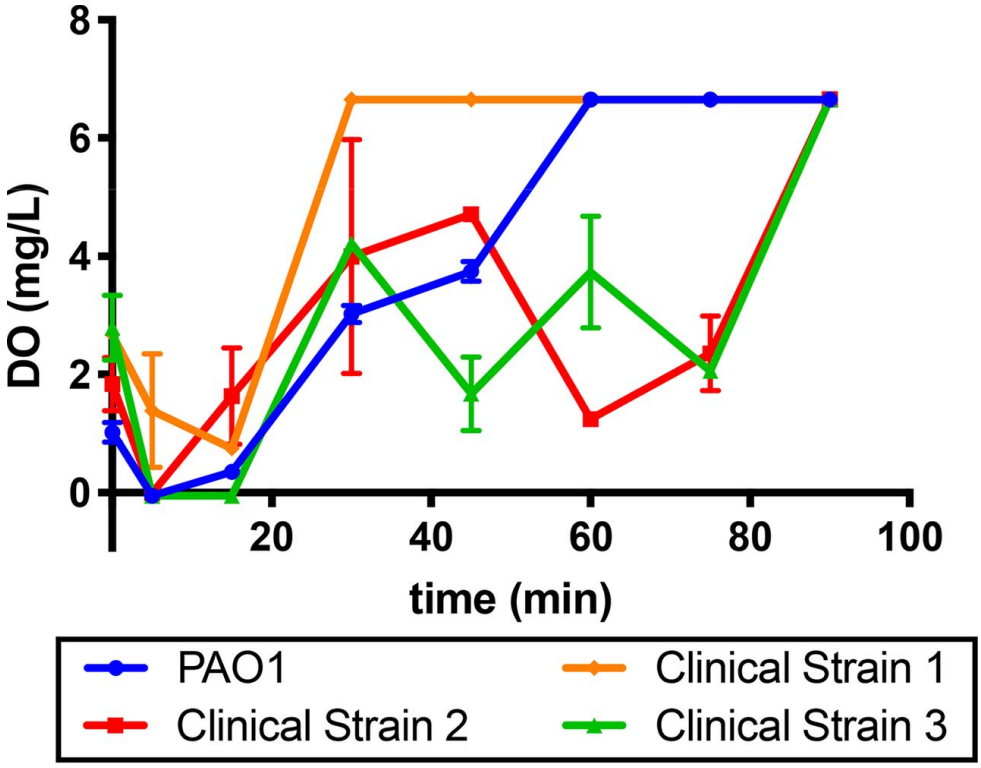

Figure 3.6 Local oxygen concentrations over time within biofilms of P. aeruginosa strain PAO1 and three clinical strains after the addition of 512 μg/ml colistin. Error bars represent a standard error of $n = 9$ pixels surrounding the chosen location.

However, there is a small region that maintains an oxygen concentration below 1 mg/liter (see Fig. A.3 and A.4 in the supplemental material), indicating that there is continued aerobic respiration in this region. This is potentially a spatially inhomogeneous area occupied by cells with resistance to colistin. CS2 shows similar oxygen concentrations near the beginning of the experiment but maintains concentrations of ~5 mg/liter for the majority of the observations. The oxygen concentration does not appear to increase until the 90-min mark, which could indicate a delayed reaction to or resistance to colistin. CS3 shows large differences in structure compared with that of PAO1 (Movie A.2 in the supplemental material) and the other two clinical strains (Movies A.3 and A.4 in the supplemental material) tested. In addition, there is a large increase in metabolic activity (indicated by a decrease in oxygen concentration) a few minutes after the

addition of the colistin sulfate. After this initial change, oxygen concentration is variable over 90 min but is never above 4 mg/liter DO, indicating sustained metabolic activity within the biofilm. For PAO1 and CS1 samples, plating after experiments showed minimal or no growth (see Fig. A.5 in the supplemental material), which supports the assumption of cell death when observing increased oxygen concentration within the biofilms. In the case of CS2 and CS3, both of which demonstrate sustained oxygen consumption after antibiotic addition, plating after experiments shows growth similar to plating before experiments. This supports the hypothesis that low oxygen concentration (high oxygen consumption) is indicative of active cell metabolism. In addition to the ability to observe differences in clinical samples, our approach also enables the measurement and observation of biofilm responses to different antibiotics. The effect of two different antibiotics (colistin and tobramycin) on oxygen concentration in PAO1 biofilms can be seen in Fig. 3.7.

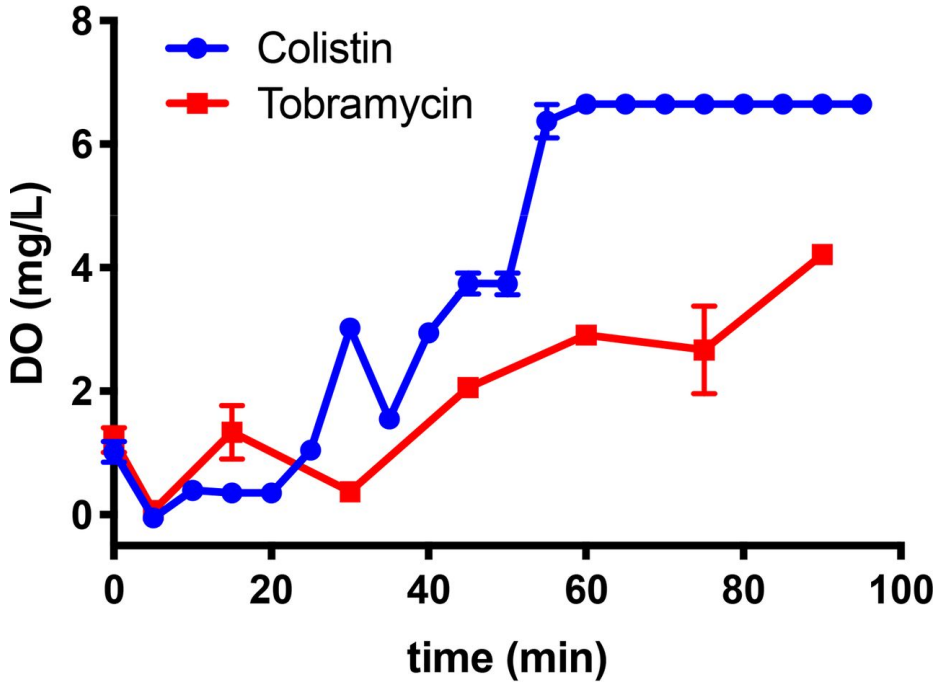

Figure 3.7 Comparison of the effects of different antibiotics (4 mg/ml tobramycin and 512 µg/ml colistin) on oxygen concentration within PAO1 biofilms. Error bars represent a standard error of n = 9 pixels surrounding the chosen location.

3.5 Discussion

3.5.1 Method development: sensor design and characterization

Our nanosensor-based approach is a method to spatiotemporally monitor analyte heterogeneity and gradients in 3D systems, such as biofilms. Our approach utilizes nanosensors which are significantly smaller than the bacteria rather than larger, potentially minimizing impacts on biofilm growth while still maintaining the ability to monitor extracellular analyte concentrations. This is possible as the size of the nanosensors is small enough to not measurably impact growth, but the approximately 160nm diameter of the nanosensors ensures that the particles are entrapped in the extracellular polysaccharides (EPS) of the biofilm and do not leak into the surrounding medium substantially. Along with the comparison of LIVE/DEAD viability staining of biofilms with and without oxygen nanosensors (see Fig. A.6 in the supplemental material), this suggests that the addition of nanosensors to growth medium does not significantly impact biofilm structure or bacterial activity. Fabrication is straightforward, which enables quick application for monitoring analytes in a variety of settings. Because these sensors can be calibrated in a variety of matrices and equipment, they are adaptable to many different applications, including biofilms of other species, cell culture scaffolds, hydrogels, and other systems where 3D monitoring is valuable. In addition, the polymeric nanoparticle platform described here is adaptable to a wide variety of analytes that might be of interest in biological systems, including oxygen, glucose, ions, and small molecules. The O_2NS we developed responds linearly to oxygen concentration, which is consistent with previously reported observations.[111] Lee and Okura note that the oxygen-sensitive metalloporphyrin used here (PtTFPP) demonstrates excellent linearity in the range of interest, but the response does become nonlinear at oxygen concentrations greater than 21 mol% in the gas phase.[111] The DiA exhibits minimal change at different oxygen concentrations, although

photobleaching begins to occur near the end of the 90-min observation periods used in the above-described experiments (Fig. A.2).

In our current implementation, the biofilm is grown with nanosensors in the medium. This makes the technique directly applicable to *in vitro* interrogation of bacterial isolates as we showed here, which were grown in such a manner as to mimic the microaggregate structure[112, 113] of biofilm infections found in the lungs of cystic fibrosis (CF) patients. However, due to the negligible diffusion of the nanosensors into the biofilm, this approach is not currently suitable for *ex vivo* or *in situ* biofilm samples. In addition, imaging was performed with confocal microscopy. These points limit nanosensors as a tool for scientific research rather than a rapid-use clinical tool. However, with a consideration to such research applications, the fabrication and use of these nanosensors build upon equipment already present in many laboratories and core facilities. This technique is not necessarily faster than culture-based techniques for antibiotic screening applications since biofilm growth (up to 72 h for mature biofilms) is required. However, the use of nanosensors is well suited for research applications (i.e. measuring metabolism of subpopulations and biofilm homogeneity) that cannot be addressed with current tools.

3.5.2 Example application: measuring antibiotic-induced metabolic changes

The ability to differentiate between the three clinical strains demonstrates the value of this approach. Using these oxygen nanosensors, it is possible to obtain information about the entire biofilm and not just a single point or a few points within it. Biofilms formed by PAO1 have a microaggregate structure (biofilms <100μm in size) similar to what is seen in the lungs of cystic fibrosis patients.[29, 112, 113] In these biofilms, we see spatial variations (Fig. 3.4) in dissolved oxygen concentration and secondary structures that are reminiscent of liquid and nutrient transport channels like those observed by Wilking et al.[29] and others.[114, 115] It is also possible to see parts of

the biofilm that are either not surface attached or loosely attached to the surface, which would be lost with the physical disruption of monitoring with the standard microelectrode-based measurements. In the case of the first clinical strain, we show that this technique can elucidate areas of different metabolism (Fig. A.4). If one were to interrogate this biofilm with a microelectrode, only measuring a small area (approximately 50μm by 50μm) would obscure the heterogeneity of the biofilm as a whole. This localization of persistent oxygen consumption could indicate the presence of antibiotic-resistant cells or persister cells within the biofilms. In the cases of clinical strains 2 and 3, this approach is able to distinguish responses to antibiotic attack as opposed to only demonstrating resistance. We note different rates of DO concentration variation between the two, with these variations occurring on measurable time scales (around 15 minutes for CS3 and 40 minutes for CS2). CS3 also had remarkably different architecture, producing a larger structure than those seen in PAO1 and the other clinical strains tested. This highlights our ability to individually profile these strains with improved measurements over traditional approaches. The ability to obtain information on spatial homogeneity of biofilm metabolism could be elevated with the addition of sensors for other analytes. Two-dimensional maps can provide x-y spatial information on biofilms but are unable to provide z axis information. Because biofilms have a complex, three-dimensional structure with channels for the movement of nutrients, water, and oxygen, the complete understanding of dynamics within the system requires three-dimensional information. Our approach allows us to rapidly gather all spatial information, and we are able to do so without disturbing the structure. Temporal information is limited only by the imaging equipment's ability to capture data. Similar to any confocal microscopy experiment, we can increase time resolution at the expense of spatial resolution or with more advanced imaging hardware.

Both antibiotics used in this study were chosen for their relevance to clinical therapy for CF patients. Tobramycin belongs to the aminoglycoside class of antibiotics and shows the greatest antipseudomonal activity of the aminoglycosides.[116] Because of this, it is a common choice for combination therapy in CF patients.[117] Colistin is a polymyxin antibiotic that is often used to treat *P. aeruginosa* airway infections in CF patients. Polymyxins are popular, as they usually retain activity against multidrug-resistant strains of *P. aeruginosa*.[118] Kill curves in *P. aeruginosa* PAO1 biofilms as well as clinical strains have been demonstrated by Hengzhuang et al. using the Calgary biofilm device method,[119] and our sensors were able to recapitulate these data with a finer time resolution. The results obtained from O_2NS measurements in Fig. 3.7 are consistent with the kill curves obtained by Hengzhuang et al.[119] using the modified Calgary biofilm device method, although our results also provide information on the structure of the biofilms and spatial distribution of high- and low-oxygen concentration regions within the biofilm. Calculations[120] and experimental data[30] from micro-electrodes show that oxygen should penetrate *P. aeruginosa* biofilms attached to surfaces to a depth of 60 to 70μm, but this assumes diffusion into a uniform biofilm. We note in Fig. 3.4 that there is considerable spatial variation within the biofilm. Therefore, we chose a point near the center of the larger aggregate for temporal analysis, which presumably has the largest diffusion barrier.

3.6 Conclusions

Here, we used polymeric oxygen-sensitive nanosensors to monitor the response of lab and clinical *Pseudomonas aeruginosa* biofilms to antibiotic attack with three-dimensional spatial data collection and 5-min temporal resolution. The nanosensors' small size, rapid response, and ratiometric signal allow for detailed interrogation of clinical samples to obtain antibiotic susceptibility information as well as data from which pharmacodynamic parameters can be

determined. Additionally, these oxygen nanosensors enable the elucidation of biofilm heterogeneities that microelectrodes and other techniques cannot capture, such as microaggregate size and shape, localization of oxygen consumption, and even biofilm features which are not surface attached. We are able to measure differences in the response of three clinical samples to antimicrobial attack and overall metabolism via changes in oxygen concentration. This approach for biofilm monitoring is straightforward to implement for *in vitro* spatial and temporal monitoring of biofilm metabolism, and future work will focus on the addition of the nanosensors to preexisting biofilms. The sensor platform's adaptability and ease of manufacture enable the monitoring of multiple or different analytes within the biofilm structure in future work as well.

3.7 Acknowledgements

This work was supported by Children's Hospital of Colorado Research Institute, the Office of Research and Technology Transfer at Colorado School of Mines, and start up funds from Colorado School of Mines. Imaging experiments were performed in the University of Colorado Anschutz Medical Campus Advance Light Microscopy Core supported, in part, by NIH/NCATS Colorado CTSI grant number UL1 TR001082. The contents of the paper are the authors' sole responsibility and do not necessarily represent official NIH views. We thank the Children's Hospital of Colorado (CHCO) sample bank for providing the clinical isolates.

CHAPTER 4

ANTIBIOTIC SUSCEPTIBILITY TESTING IN BIOFILMS USING OXYGEN NANOSENSORS

This chapter is modified from a paper currently pending submission[1]

Megan P. Jewell,[2] Alexa David,[3] and Kevin J. Cash[4]

4.1 Abstract

In clinical environments, many serious antibiotic-resistant infections are caused by biofilm-forming species. This presents issues when attempting to determine antimicrobial dosing as traditional antibiotic susceptibility tests (ASTs) are designed around planktonic bacteria and thus offer information that is not relevant to the biofilm phenotype present in the patient. Even the popular Calgary biofilm device may provide inaccurate minimum biofilm inhibitory concentrations (MBICs) and can be time- and material-intensive. In this work, we present a method utilizing oxygen-sensitive nanosensor technology to monitor the oxygen consumption dynamics of living biofilms as they are exposed to antibiotics. This method provides information on the MBIC as well as the minimum biofilm eradication concentration (MBEC) in a manner that requires fewer materials and is more reflective of biofilm behavior than a traditional AST.

4.2 Introduction

In the past two decades, multi-drug resistant infections have arisen as a serious concern for worldwide health.[121] Of the species considered by the World Health Organization as critical and high priority pathogens,[122] many are also known to form biofilms that contribute to chronic

[1] Pending submission
[2] Primary author and Ph.D. Candidate
[3] Co-author and undergraduate researcher
[4] Corresponding author and Ph.D. Advisor

infectious disease states.[28] Among these are *Pseudomonas aeruginosa, Staphylococcus aureus, Acinetobacter baumanii,* and enterococcal species.[122] Biofilms have many unique mechanisms which contribute to their recalcitrance and resistance to antimicrobials. These mechanisms and phenotypic variations can arise without exposure to antimicrobial agents and have been extensively reviewed elsewhere.[123, 124] Inherent resistance can then be exacerbated by current issues such as antibiotic use without a prescription/self-medication and sub-inhibitory concentrations in food, water, and the environment from agricultural use.[125]

Pseudomonas aeruginosa is the most common reported bacterial infection in the lungs of patients with cystic fibrosis.[77] Chronic infection results in biofilm formation, which advances lung damage and often leads to respiratory failure.[126] Despite recent advances in biofilm research and improved antibiotic treatment regimens, no cure has been identified for these chronic biofilm infections[127] which are the primary cause of mortality in cystic fibrosis patients.[128] Considering the severity of *P. aeruginosa* infections in cystic fibrosis patients, knowledge of important structural analytes and finding alternative treatment regimens are urgent research priorities in the biomedical field.[129] Unfortunately, treatment of *P. aeruginosa* infections can be difficult due to natural antibiotic resistance.[79]

Traditional antibiotic susceptibility tests (ASTs) such as liquid culture tests or the disk diffusion method often take 1-2 days after initial growth for accurate results,[130, 131] and there is often a lack of correlation between planktonic ASTs and biofilm-based infections.[80] The minimum inhibitory concentration (MIC) for the growth of bacteria is typically defined with respect to agar or broth dilution methods as the concentration of antimicrobial at which no visible growth is observed. Growth is usually quantified as a change in turbidity or optical density at $\lambda = 600$nm.

Several biofilm models have been developed and offer different information about biofilm susceptibility. The MBEC assay system (formerly known as the Calgary biofilm device)[123] is often used to define important antimicrobial parameters such as the minimal biofilm inhibitory concentration (MBIC),[132, 133] but can predict therapeutic success at concentrations that do not work or can amplify selection of resistant mutants.[80] Pharmacokinetic/pharmacodynamic flow cell models can provide information on the spatial and temporal dependence of various antibiotics. Unfortunately, even these biofilm susceptibility assays performed are limited as they often require staining or fixing, which can kill the biofilm or destroy structure.[80]

As oxygen is fundamental to metabolism in nearly all organisms, the detection and monitoring of oxygen is the focus of a large subset of the bioanalytical sciences. Of the many options available (reviewed extensively by Wang and Wolfbeis),[16] the most attractive options for monitoring microbes are optical methods. Unlike electrochemical and pressure-based methods, optical oxygen sensors offer advantages such as no consumption of the oxygen, reversibility, ease of miniaturization, and the potential for non-invasive measurements. In this work, we use an established platinum-centered porphyrin as the luminescent oxygen-sensitive probe along with an oxygen-insensitive reporter to control for variation in sensor concentration within the heterogeneous structure of the biofilm. These dyes are suspended in a heavily plasticized polymer matrix which is miniaturized into nanoparticles via nanoemulsion. The mechanisms of oxygen sensing for both the porphyrin dye and the polymeric nanosensors have been described elsewhere by Lee and Okura[111] and Jewell et al.[44] These oxygen-sensitive nanosensors (O_2NS) are small (approx. 150nm) and easily incorporated into the extracellular space of a growing biofilm by the bacteria. Through monitoring oxygen consumption, a proxy for metabolism, we can ascertain the

impact of antibiotics on the bacteria in the biofilm and determine the sensitivity of the specific strain to the antibiotic used.

4.3 Materials and Methods

4.3.1 Materials

High-molecular-weight poly(vinyl chloride) (PVC), bis(2-ethylhexyl) sebacate (BEHS), tetrahydrofuran (THF), dichloromethane (DCM), and phosphate-buffered saline (PBS) were purchased from Sigma-Aldrich (St. Louis, MO, USA). Platinum (II) meso-tetra(pentafluorophenyl)porphine (PtTFPP) was purchased from Frontier Scientific (Logan, UT, USA). 1,2-Dipalmitoyl-sn-glycero-3-phosphoethanolamine-N-[methoxy(polyethylene glycol)-750] ammonium salt in chloroform (PEG-lipid) was purchased from Avanti Polar Lipids (Alabaster, AL, USA). 4-Di-16-ASP (4-[4-(dihexadecylamino)styryl]-N-methylpyridinium iodide) (DiA) was purchased from Thermo Fisher Scientific (Waltham, MA, USA).

4.3.2 Oxygen sensor fabrication

A total of 30 mg of polyvinyl chloride (PVC) was weighed into a 2-ml vial and combined with 66 µl of BEHS. In a separate vial, 5 mg of Pt(II) meso-tetra(pentafluorophenyl)porphine (PtTFPP) and 0.2 mg 4-Di-16-ASP (4-[4-(dihexadecylamino)styryl]-N-methylpyridinium iodide) (DiA) were dissolved in 500µl of tetrahydrofuran (THF). The THF and dissolved dyes were then added to the PVC/BEHS mixture and vortexed for 1 min until all solids were dissolved. A total of 750µl of dichloromethane (DCM) was then added to the vial, and the mixture was vortexed thoroughly. The optode cocktail was then stored at 4°C until use. To fabricate nanosensors from the optode cocktail, 2 mg PEG-lipid (80µl of a 25-mg/ml solution in chloroform) was dried in a 4-dram scintillation vial and then resuspended in 5 ml of PBS (pH 7.4) with a probe tip sonicator (Branson Digital Sonifier 450; Branson Ultrasonics Corporation, Danbury, CT) for 30 s at 20%

intensity. A total of 125 µl of the optode cocktail mixture was injected into the PBS/PEG-lipid solution under probe tip sonication (3 min, 20% intensity). Following sonication, excess polymer was removed by filtration via a 0.8-µm syringe filter (Pall Corporation, Port Washington, NY). Sensors were then concentrated ~10x via ultrafiltration (Amicon Ultracel) and sterilized via filtration with a 0.22-µm syringe filter.

4.3.3 Biofilm growth

Pseudomonas aeruginosa strains PAO1 (ATCC 15692), PGO2330 (ATCC BAA-2108), PGO2396 (ATCC BAA-2113), and PGO2401 (ATCC BAA-2114) were purchased from the American Type Culture Collection and used without further alteration. Growth of biofilms was adapted from Harrison et al.[134] Initially, a first subculture of the strain of interest of *P. aeruginosa* was plated on lysogeny broth (LB) agar from frozen stocks. A 2nd subculture was plated from the initial plate in order to ensure a monoculture.

From this 2nd subculture, a standardized inoculum for the entire 96-well plate was created. 1.5 ml of sterile PBS was transferred to a culture tube, and several colonies of *P. aeruginosa* were dispersed in the PBS. The OD_{600} of this solution was adjusted to 0.05 by either addition of more colonies or addition of more sterile PBS. 1 ml of the bacterial suspension was then transferred to a 50-ml conical vial and mixed with 29 ml of sterile LB broth. 180 µl of the inoculum was added to each well of a 96-well plate. 20 µl of concentrated oxygen nanosensors (O_2NS) were also added to each well except for Column 12, for a final volume of 200 µl per well. Column 12 had 20 µl of PBS added instead and served as a control. A 96-well qPCR plate (Roche) was placed in the inoculated 96-well plate and wrapped with parafilm to prevent moisture loss. The plate was then incubated in an orbital shaker-incubator for 10h at 37°C and 125 RPM. 80 µl of the remaining inoculum was then serially diluted 6 times (DF = 10 for each step), and 10 µl of each dilution was

spotted onto a gridded LB agar plate and incubated at 37°C for 24h. These plates were used to determine the mean viable cell count (MVCC) for the starting inoculum.

4.3.4 Antibiotic plates & data analysis

Antibiotic challenge plates were created by serially diluting antibiotic stock solutions over 10 columns (DF = 2 for each step) in a 96-well plate. These stock solutions were made by dissolving the antibiotic (colistin, tobramycin, imipenem, or ampicillin) in sterile PBS at a concentration of 1 mg/ml. Each well had a final volume of 200 µl to ensure full submersion of the plate lid biofilms. The two end columns (Columns 1 and 12) of the 96-well plate contained 200 µl of sterile PBS and served as controls. A 96-well rinse plate was also prepared where each well contained 200 µl of sterile PBS – this served as the initial reading for later data analysis. After the initial reading, biofilm lids were exposed to the antibiotic challenge plate and read every 3 minutes for 24h to capture the dynamics of the oxygen nanosensors. The static peak of the DiA reference dye was read at 585nm along with the dynamic peak of the oxygen-sensitive platinum porphyrin dye at 650nm. Both dyes were excited at 485nm and plates were read in a Synergy H1 microplate reader (BioTek, Winooski, VT, USA).

Raw kinetic data was normalized to a rinse reading – in initial reading of the ratiometric intensity in PBS to control for the basal oxygen consumption of the biofilm's logarithmic phase growth. Then, the slope of the initial 5h (the antibiotic response phase) is found via linear regression. This slope is then plotted vs. concentration to produce the dose-response curves presented in the Results & Discussion section. In order to determine the MIC, the deviation between the upper plateau (the 'top' value) and the sigmoidal curve fit was calculated in Microsoft Excel, and Solver was used to find the antibiotic concentration where the dose-response equation deviated from the upper plateau by 1 standard deviation.

4.3.5 MIC test strips

MIC test strips (MTS) for colistin (0.016 μg/ml – 256 μg/ml) and tobramycin (0.016 μg/ml – 256 μg/ml) were purchased from Liofilchem, Inc. (Waltham, MA, USA). MTS were used according to directions from the manufacturer. Briefly, well-isolated colonies from an overnight agar plate of the *P. aeruginosa* strain of interest were suspended in sterile PBS to a McFarland standard of 0.5 (OD_{600} = 0.08-1). This inoculum was streaked over the entire agar surface with a sterile swab three times to ensure complete coverage. The MTS was applied to the agar surface with sterile forceps and the plate was then incubated at 37°C for 24h. Results were read manually using the scale on the test strip to determine the minimum inhibitory concentration (MIC) to within a 2-fold dilution.

4.4 Results and Discussion

Using our oxygen nanosensors, we are able to monitor oxygen concentration and consumption within bacterial biofilms. Figure 4.1 shows the change in ratiometric intensity of the O_2NS in the biofilms over 24h. For a biofilm that has not been challenged with an antimicrobial (labeled 'PBS w/ O_2NS'), the increase in O_2NS intensity (and by extension, the change in oxygen consumption by the biofilm) is indicative of growth. Biofilm growth plateaus by hour 10 as the bacteria reach a nutrient limitation within the microtiter wells. Variation in O_2NS signal can be seen after this as some of the biofilm detaches and attempts to disperse. In a biofilm that has been challenged with an antimicrobial, the increase in oxygen consumption along with the rate of increase are a combination of growth and metabolic response to the antimicrobial agent.

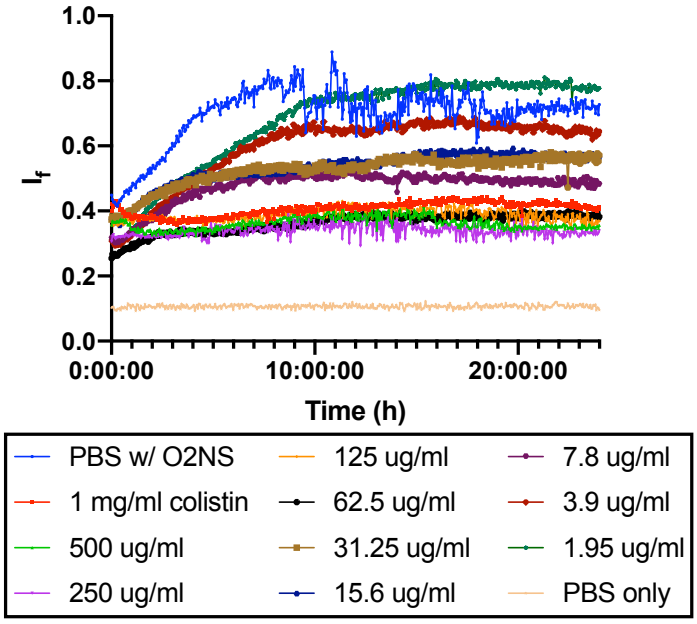

Figure 4.1 Kinetic ratiometric intensity data for *P. aeruginosa* PAO1 that has been challenged with serial 2-fold dilutions of colistin sulfate in phosphate buffered saline (pH = 7.4).

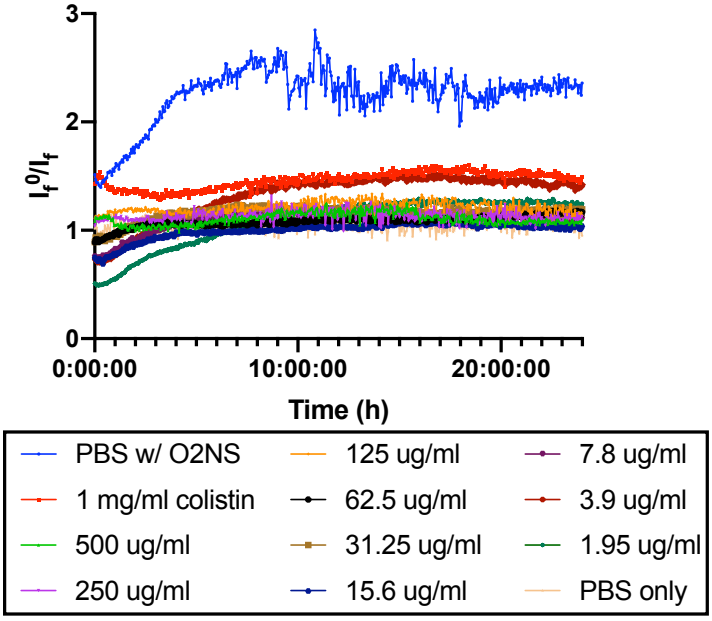

Figure 4.2 Normalized kinetic ratiometric intensity data for *P. aeruginosa* PAO1 that has been challenged with serial 2-fold dilutions of colistin sulfate in phosphate buffered saline (pH = 7.4). Data was normalized to an initial reading of each biofilm well submerged in PBS containing no antibiotic.

This kinetic data (equivalent to a kill curve from an MBEC microtiter assay) can then be normalized to the ratiometric intensity of the initial biofilm as a way to account for this post-incubation growth. This normalized data can be seen in Figure 4.2, where it can be seen that changes in oxygen consumption are nearly complete by hour 5.

Figure 4.3 is the dose-response curve of *P. aeruginosa* PAO1 created using this normalized kinetic data. For each tested concentration of colistin, the initial slope of the antibiotic response was determined via a linear regression of the data for 0 h to 5 h. The slopes were plotted against antibiotic concentration on a log 2 scale to achieve the sigmoidal dose-response relationship.

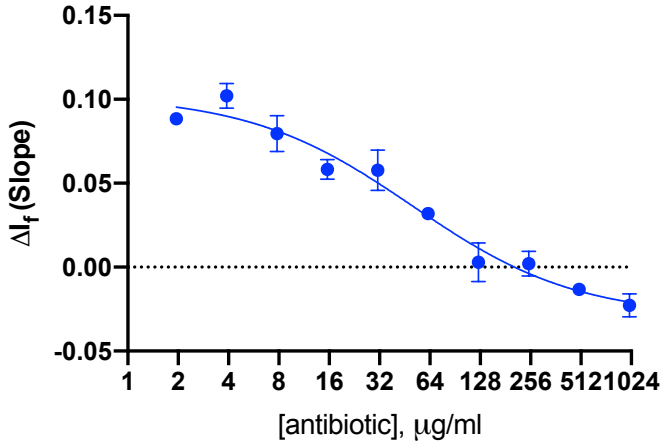

Figure 4.3 Dose-response relationship for colistin sulfate and *P. aeruginosa* PAO1 biofilms as determined by the rate of change of oxygen consumption of the biofilms after exposure to antibiotic. Here, error bars represent standard deviation and $n = 4$ biological replicates.

In this method, an equivalent minimum inhibitory concentration definition would be the upper end of the dynamic range as this is the concentration where a measurable change in the output is seen. Mechanistically, this would correspond to the concentration that causes a measurable decrease in the oxygen consumption rate of the biofilms. Here, a 'measurable decrease' was taken to mean a deviation from the upper plateau ('Top') value by 1 standard deviation. This value and other important parameters are graphed in Figure 4.4.

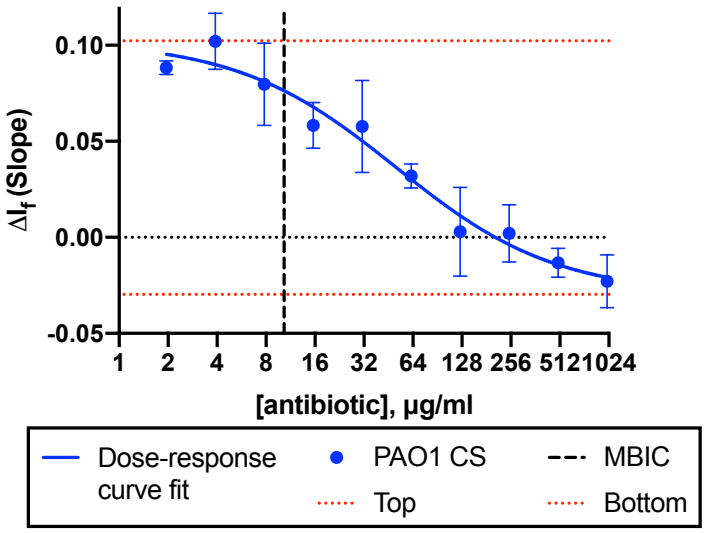

Figure 4.4 Dose-response curve for colistin sulfate and *P. aeruginosa* PAO1 biofilms. Also plotted are the upper and lower plateaus for the sigmoidal curve fit, along with the minimum biofilm inhibitory concentration (MBIC) of 10 µg/ml.

Thus, the minimum biofilm inhibitory concentration (MBIC) of the tested antimicrobial agent can be determined from the dose-response relationship found using this method. The MIC values as determined by a commercially available epsilometer test (also known as a MIC test strip or MTS) produced by Liofilchem can be found Table 4.1 along with MBIC values determined using the O_2NS method detailed in this work. In nearly all cases, the MBIC was determined to be significantly higher than the value reported by the MTS, which are accurate to within one 2-fold dilution.

We applied our new method for MBIC determination on other clinically relevant strains of Pseudomonas aeruginosa with varying sensitivity to colistin and tobramycin. The BAA-2108 strain is listed by ATCC as being of intermediate susceptibility, and the MTS value of 4 µg/ml is within one 2-fold dilution of the Clinical and Laboratory Standards Institute (CLSI) breakpoint of 8 µg/ml and matches the European Committee on Antimicrobial Susceptibility Testing (EUCAST) value of 4 µg/ml. However, the MBIC was determined to be >256 µg/ml as the biofilms grown

using BAA-2108 exhibited only minimal response even at high concentrations of tobramycin, which lead to an ambiguous dose-response curve fit.

MTS are used on lawns of bacteria grown on agar plates, and although agar colonies are sometimes referred to as "colony biofilms," the difference in exposure to nutrients and other environmental factors (especially submersion) leads to different phenotypic behavior between agar plate colonies and the microaggregates and submerged biofilms more likely to be found in the human body. In contrast, the O_2NS-embedded biofilms are grown submerged in inoculated media, and the biofilm-covered surface is then removed and tested to ensure that only the response of bacteria within the biofilm is observed. These increased MBIC values are consistent with other work that has shown up to 1000-fold increased resistance to antimicrobials when biofilms were compared to their planktonic counterparts.

Table 4.1 MIC and MBIC values for wild-type PAO1 and antibiotic-resistant strains BAA-2108, BAA-2113, and BAA-2114 as calculated using commercially available MIC agar test strips and O_2NS. All values are reported in μg/ml.

MIC/MBIC values (μg/ml)	PAO1	BAA-2108	BAA-2113	BAA-2114
Colistin (MTS)	4	2	2	3
Colistin (O_2NS)	10	4	23	13
Tobramycin (MTS)	2	4	1.5	2
Tobramycin (O_2NS)	6	> 256	21	24

In addition to MTS, MIC values are also able to be determined via broth dilution methods and disk diffusion methods. While cost effective, these methods are time and labor intensive, and only provide information on planktonic cells. MBIC values can also be determined via MBEC microtiter assay, which can be material-intensive in addition to time and labor requirements, as each time point on the kinetic kill curve requires a new set of incubated biofilms and a new

microtiter plate of antibiotic dilutions. The O_2NS method requires only a rinse plate and one microtiter plate of antibiotic dilutions.

Figure 4.5 shows the collected dose-response curves for each strain tested against colistin sulfate and tobramycin. All strains showed a response to both antibiotics within the range of dilutions tested, with the exception of BAA-2108, which showed only minimal response at very high concentrations of tobramycin. This is consistent with ATCC's determination that this strain is of intermediate resistance to tobramycin. ATCC did not provide any information on the susceptibility of any of the strains to colistin, but all exhibited a response to colistin in the O_2NS method and the MTS values were within one 2-fold dilution of the CLSI and EUCAST values for susceptibility of 2 μg/ml.

This method and analysis are most robust for antimicrobials which exhibit primarily concentration dependence. That is, the time which the biofilm is exposed to the MIC is a secondary factor to the MIC itself. This includes drug classes such as the aminoglycosides and polymyxins, which include tobramycin and colistin, respectively. Antibiotics such as the carbapenems and penicillins are instead dependent on exposure time to a concentration above the MIC as well as the MIC. This presents issues in a limited volume like a microtiter plate as the antimicrobial is depleted, which can confound the dose-response curve and produce the bell shape seen in Figure 4.6. For this figure, strain BAA-2114 biofilms were exposed to serial 2-fold dilutions of imipenem (a carbapenem) and ampicillin (a penicillin) in the same manner as tobramycin and colistin.

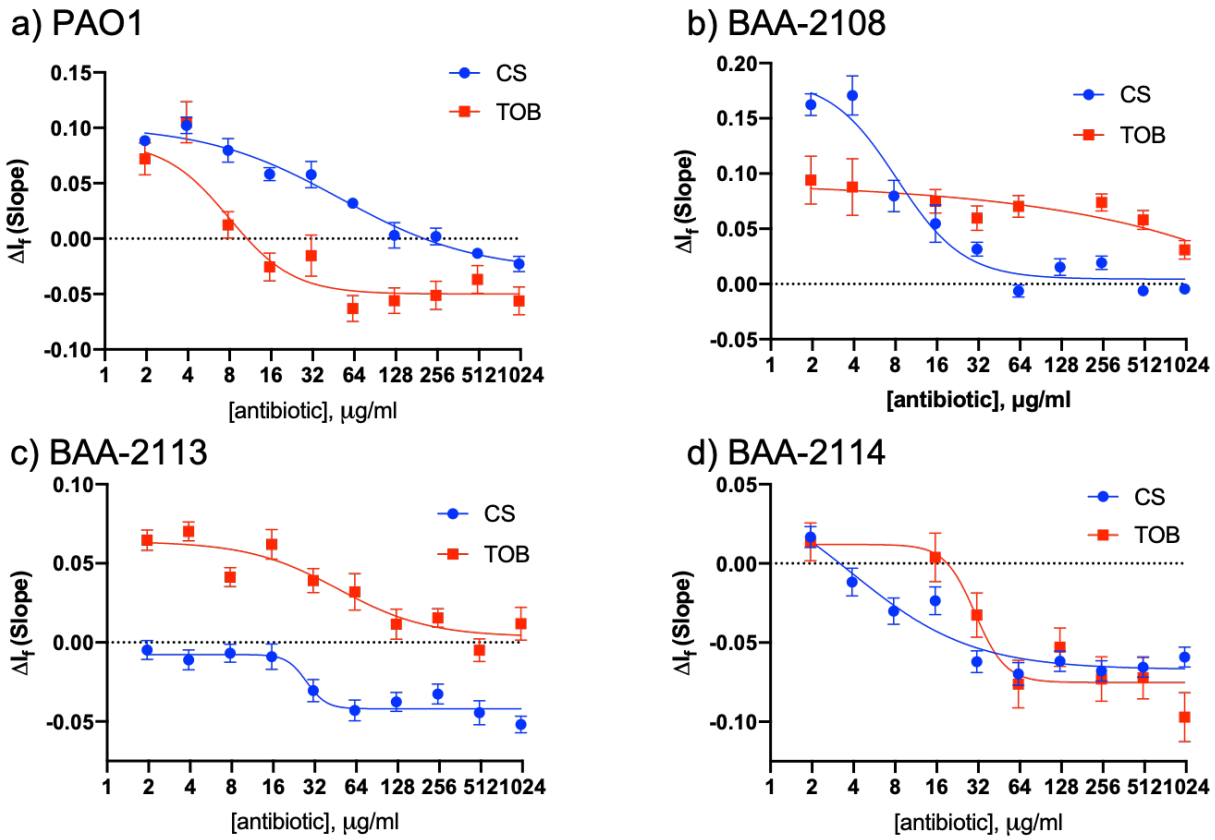

Figure 4.5 Dose-response curves for *P. aeruginosa* strains exposed to colistin sulfate (CS) and tobramycin (TOB). Strains tested and analyzed were: a) PAO1, b) BAA-2108, c) BAA-2113, and d) BAA-2114.

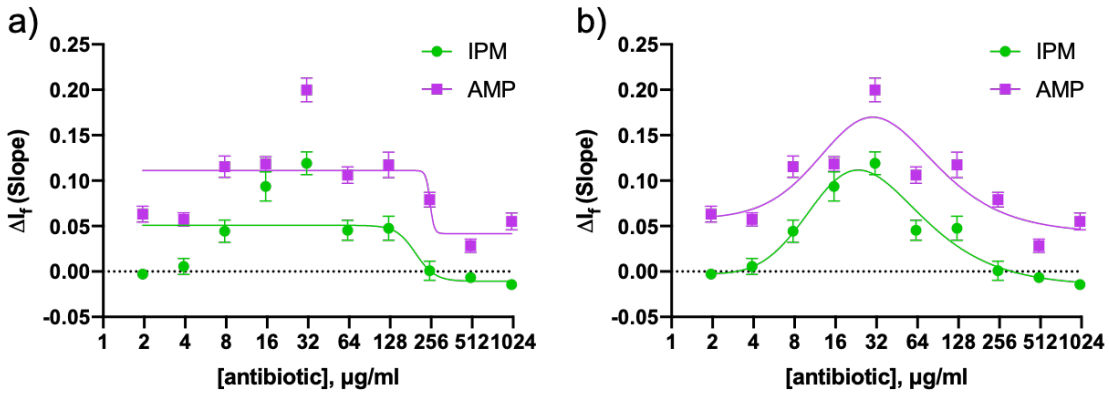

Figure 4.6 Data and attempted dose-response curve fits of *P. aeruginosa* BAA-2114 response to imipenem (IPM) and ampicillin (AMP).

Strain BAA-2114 is reported by ATCC to be resistant to ampicillin and susceptible to imipenem. However, the unexpected response, especially at lower microtiter concentrations of the antibiotic makes fitting any sort of known dose-response equation difficult and unreliable. The major difference here is, again, that imipenem and ampicillin are dependent on both the concentration they are exposed to *and* the length of time they are exposed to that concentration. The latter criterion is difficult to control for in a small fixed volume such as the microtiter well. Attempts to account for this are the subject of future work.

4.5 Conclusions

Here, we have demonstrated a method of antibiotic susceptibility testing utilizing oxygen-sensitive polymeric nanosensors that is less material-intensive and more reflective of biofilm dynamics than traditional antibiotic susceptibility tests. Both the kill curve time-based dynamics and the static MBIC parameter can be found using this method, although further refining and automation of the statistical analysis involved in these calculations should be considered before any attempts at clinical translation. This method is currently only able to test antibiotics that are primarily concentration dependent, such as the polymyxins, aminoglycosides, and fluoroquinolones. Future work to account for exposure time dependence would expand the usefulness of the method to other major classes of antimicrobials, such as penicillins, cephalosporins, and carbapenems. Tests with clinical samples (which are often not monocultures) would also improve the usefulness of this method as an *in vitro* reflection of *in vivo* behavior.

4.6 Acknowledgements

This work was supported by the Office of Research and Technology Transfer at Colorado School of Mines, the Colorado Office of Economic Development and International Trade, and start

up funds from Colorado School of Mines. The authors would like to thank Tony Tien for his help in the maintenance of the lab's growing *P. aeruginosa* strain collection.

CHAPTER 5

TRIPLET-TRIPLET ANNIHILATION UPCONVERSION-BASED NANOSENSORS FOR FLUORESCENT DETECTION OF POTASSIUM

This chapter is modified from a paper accepted for publication[1]

Megan P. Jewell,[2] Meredith D. Greer,[3] Alexandra L. Dailey,[3] and Kevin J. Cash[4]

5.1 Abstract

Typical ionophore-based nanosensors use nile blue-derived indicators called chromoionophores which must contend with strong background absorption, autofluorescence, and scattering in biological samples that limit their usefulness. Here, we demonstrate potassium-selective nanosensors that utilize triplet-triplet annihilation upconversion to minimize potential optical interference in biological media and a pH-sensitive quencher molecule to modulate upconversion intensity in response to changes in analyte concentration. A triplet-triplet annihilation dye pair (platinum (II) octaethylporphyrin and 9,10-diphenylanthracene) was integrated into nanosensors containing an analyte binding ligand (ionophore), charge-balancing additive, and a pH indicator quencher. Nanosensor response to potassium was shown to be reversible and stable for three days. In addition, the nanosensors are selective against sodium, calcium, and magnesium (selectivity coefficient in $\log_{10}$ units of -2.2 for calcium, -2.0 for sodium, and -2.4 for magnesium), three interfering ions found in biological samples. The lack of signal overlap between the upconversion nanosensors and GFP, a common biological fluorescent

[1] In press. Reprinted with permission from *ACS Sens.* 2020, 10.1021/acssensors.9b02252 © 2020 American Chemical Society.
[2] Primary author and Ph.D. Candidate
[3] Co-author and undergraduate researcher
[4] Corresponding author and Ph.D. Advisor

indicator, is demonstrated in confocal microscope images of sensors embedded in a bacterial biofilm.

5.2 Introduction

Selective and tunable ion detection and imaging in biological and environmental samples is essential in a range of investigations. Sensors that are capable of continuous and long-term monitoring of biological processes, both *in vitro* and *in vivo*, allow for interrogation to answer basic research questions and monitor health in a clinical setting. The many potential analytes of interest and the development of sensors for them have been extensively reviewed and summarized elsewhere.[1, 2, 15, 135-137] In particular, Ruckh and Clark discuss the importance of continuous physiological monitoring of analytes such as sodium, potassium, and glucose for conditions such as renal failure and diabetes.[2] Sensors for detection of other electrolytes like calcium and lithium are discussed in reviews by Søndergaard et al.[135] and Rong et al.[1]

Ionophore-based optical sensors (IBOS) are a class of indirect ion-selective optical sensors that have been used to measure a wide range of analytes *in vitro,*[138, 139] *in situ,*[140] and *in vivo*.[141, 142] These sensors utilize a mechanism similar to ion-selective electrodes (ISEs), and are well described elsewhere.[7, 12] Typically, IBOS are composed of a pH indicator, an analyte-binding ligand (ionophore), and a charge-balancing additive suspended in a highly plasticized hydrophobic polymer matrix which is surrounded by a lipid layer. As the target ion binds to the ionophore, the pH indicator is deprotonated in order to maintain electroneutrality within the polymer matrix. Based on well-established ion exchange theory,[12] this change in protonation can be monitored via absorbance or fluorescence measurements. Because the recognition element (ionophore) is decoupled from the signaling element (pH indicator), nanosensors for different ions are easily created without the need to design new recognition mechanisms.[8] Thus, the potassium-selective

nanosensors described here can easily be made selective for another ion by exchanging the ionophore and other components are also able to be substituted.[143]

The signaling elements utilized by most IBOS are nile-blue derivative pH indicators (chromoionophores).[8] Some methods that avoid pH cross-reactivity are also utilized.[144, 145] Recent work in ionophore-based nanosensors has included the use of silicon-based particles[146] as well as carbon dots (aka graphene quantum dots)[147-149] as signaling elements as well. However, these dyes, and indeed most fluorescent dyes, must contend with strong background absorption, autofluorescence, and scattering in biological samples which can significantly limit their application.[150] Our solution to some of these issues are materials with the unique property of upconversion. These materials exhibit an anti-Stokes shift under excitation that allows their signal to be easily distinguished from the autofluorescence and background interference of biological tissues and samples.[136] Lanthanide-based upconversion, which has been used extensively as a biological imaging component,[151-153] and is well described,[154, 155] utilizes lanthanide ions doped into a crystalline lattice as emissive centers. There are several reports of lanthanide-based bulk optodes capable of sensing pH, Pb^{2+}, K^{+}, Na^{+}, Ca^{2+}, and Cu^{2+}.[156, 157] However, there are several drawbacks to lanthanide-based upconversion materials. The primary drawback is the relatively low upconversion efficiency, which then requires relatively high power density excitation for any substantive imaging.[154] Another drawback for use on the nanoscale is the size of lanthanide-based materials. Because these materials are sensitive to surface deactivations, the high surface-to-volume ratio of nanoparticles can decrease upconversion efficiency.[158] Although core/shell structures can mitigate this problem, many lanthanide particles used in sensing are on the order of hundreds of nanometers in size,[156, 157, 159, 160] which precludes their use in polymeric nanoparticle systems like our IBOS, which are only 100nm in diameter.[101, 103]

An alternate upconversion mechanism, which we utilize in this work, is triplet-triplet annihilation upconversion (TTA-UC). As opposed to the inorganic lanthanide-based system, TTA-UC utilizes organic molecules known as sensitizers and emitters to produce upconversion luminescence. In this process, the sensitizer absorbs excitation light and populates its first singlet excited state. After intersystem crossing to the triplet state, there is triplet-triplet energy transfer between the sensitizer and emitter.[161] Triplet-triplet annihilation occurs between two excited emitter molecules, and this energy populates the first singlet excited state of one of the emitter molecules, which then produces delayed fluorescence.[161] Common examples of sensitizer dyes are metal-centered porphyrins, and commonly used emitters are high luminescence quantum yield dyes such as 9,10-diphenylanthracene or BODIPY.[154] In comparison to lanthanide systems, TTA-UC requires relatively low power excitation[154] and can be wavelength tuned by choice of sensitizer and annihilator. The sensitizer-annihilator dye pairs are organic dyes that are often commercially available, soluble in the organic phase, and able to be implemented into IBOS. TTA-UC has been utilized in several forms as a biological imaging agent.[154] There are *in vivo*[162-167] and *in vitro*[153, 168-170] examples that have overcome the problem of oxygen quenching of TTA-UC. However, TTA-UC has found limited application in sensing platforms. Thus far, it has been limited to Borisov et al.[171] creating a polymer optode film to directly sense oxygen. However, there are already numerous optical oxygen sensing platforms available.[15, 137] To our knowledge, there have been no reports of TTA-UC used in a more general sensing platform such as those based on ionophores. TTA-UC is not inherently sensitive to ion concentration, so in this work it is coupled with a pH-sensitive quencher dye that modulates the signal that has been utilized previously to gate other optically static systems.[101, 172, 173]

5.3 Materials and Methods

5.3.1 Materials

Poly(vinyl chloride), high molecular weight (PVC), tetrahydrofuran (THF), dichloromethane (DCM), Sodium tetrakis[3,5-bis(trifluoromethyl)phenyl]borate (NaBARF; Selectophore™), 2-dodecyl-2-methyl-1,3-propanediyl bis[N-[5′-nitro(benzo-15-crown-5)-4′-yl]carbamate] (Potassium ionophore III, Selectophore™), and platinum (II) octaethylporphyrin (PtOEP), bis(2-ethylhexyl) sebacate (DOS/BEHS, Selectophore™), and soybean oil were purchased from Sigma Aldrich (St. Louis, MO, USA). 9,10-diphenylanthracene (DPA) was purchased from Acros Organics. 1,2-dipalmitoyll-sn-glycero-3-phosphoethanolamine-N-[methoxy(polyethylene glycol)-750] ammonium salt in chloroform (PEG-lipid) was purchased from Avanti Polar Lipids (Alabaster, AL). 2-[4-(2-hydroxyethyl)piperazin-1-yl]ethanesulfonic acid (HEPES; Molecular Biology grade), 2-amino-2-hydroxymethylpropane-1,3-diol (TRIS; 2M), potassium chloride (KCl), hydrochloric acid concentrate (HCl; 10N, ACS certified), and sodium hydroxide concentrate (NaOH; 10N, ACS certified) were purchased from Fisher Scientific (Waltham, MA, USA). Blueberry-C6-ester-652 was purchased from Berry & Associates, Inc. (Dexter, MI, USA).

5.3.2 Nanosensor fabrication

57.4 mg of polyvinyl chloride (PVC) was weighed into a 2 ml vial and 38.4 µl of soybean oil was added. This vial was then vortexed for 1 minute. In a separate vial, 2.9 mg of 9,10-diphenylanthracene (DPA), 0.185 mg platinum octaethylporphyrin (PtOEP), 1 mg potassium ionophore III (KI3), 1 mg Blueberry-C6-ester-652 (Blueberry), and 1 mg NaBARF were dissolved in 585 µl of tetrahydrofuran (THF). The THF and dissolved dyes are then added to the PVC/soybean oil mixture and vortexed thoroughly for 1 minute. This mixture of components

(PVC, soybean oil, and dyes suspended in solvent) - called the optode cocktail (a precursor for optode formation) - was then stored at 4°C.

Nanosensors were prepared in a manner similar to that described in Billingsley et al.[174] The optode cocktail was spread on a glass surface and allowed to dry for at least 30 minutes. The dried optode film was then transferred to a 4 dram scintillation vial that was charged with 3 ml HEPES/Tris solution (10 mM HEPES/ 6mM TRIS buffered at pH = 7.4) along with 5 mg (25 mg/mL in 200 µl chloroform) of 1,2-dipalmitoyl-sn-glycero-3-phosphoethanolamine-N-[methoxy(polyethylene glycol)-750] ammonium salt in chloroform (PEG-lipid). The vial was agitated by hand to ensure the optode was suspended in the PEG-lipid/chloroform phase. The solution was then emulsified with a probe-tip sonicator (Branson) at 40% amplitude for 3 min. The emulsification was then filtered with a 0.8 µm Supor Membrane filter (Pall Corporation) to remove excess components.

5.3.3 Nanosensor characterization

The nanosensors' fluorescent response was calibrated in KCl test solutions prepared at double the desired final concentration in HEPES/Tris buffer solution (pH = 7.4). 300 µl of nanosensor solution and 300 µl of KCl test solution were mixed in screw-top quartz cuvettes (Starna Cells, Atascadero, CA) to achieve the desired final analyte concentration. Response curves were generated by collecting fluorescence intensity with an excitation of 532 nm and an emission of 435 nm. Values were normalized between the endpoint responses. A four-parameter logistic response curve was applied with GraphPad Prism 7 software (GraphPad, La Jolla, CA, USA) to determine response characteristics.

Fluorescence measurements were performed on an Avantes StarLine spectrometer (Avantes, Louisville, CO) and absorbance measurements were performed on a Synergy H1

microplate reader using Nunc™ MicroWell™ 96-Well Optical-Bottom Plates with Polymer Base (Nalgene Nunc International, Roskilde, Denmark). All fluorescence measurements were performed with 532 nm laser excitation from a 5mW laser (Z-Bolt, Clackamas, OR) through a 600 µm fiber (Avantes) unless otherwise stated. Dynamic light scattering, zeta potential, and mobility measurements were performed on a Brookhaven zetaPALS with Particle Solutions software V 2.2 (Brookhaven Instruments Corporation, Holtsville, NY). For reversibility measurements, nanosensors were concentrated ~10x via ultrafiltration (Amicon Ultracel) and immobilized in microdialysis tubing (MWCO 13kDa, Spectrum Laboratories) on the bottom of a 4-well LabTek Chamber Slide using underwater epoxy.[102] The chamber slide was placed on the microscope stage and solutions of either 10^{-8} M or 2 M KCl in HEPES/Tris (pH = 7.4) were exchanged 3 times each, with washes of HEPES/Tris between each exchange. Nanosensors were excited at 514 nm and emission from 400-450 nm was recorded as single images using a Zeiss LSM780 confocal microscope (Zeiss, Switzerland). Images were analyzed using ImageJ.

Upconversion nanosensor (UCNS) shelf stability was monitored over 4 days. 24 batches of UCNS were synthesized as described above and homogenized to obtain the necessary volume. The nanosensors were stored in the dark at room temperature. On days 1, 2, 3, and 4 triplicate 300 µl aliquots were combined with 300 µl KCl in HEPES/Tris (pH = 7.4) solution to produce a response curve. Nanosensor photostability was performed using the Avantes StarLine spectrometer and Starna screw top cuvettes. Fresh UCNS were prepared as described and 600 µl was injected into the cuvettes. Emission at 435 nm with continuous excitation at 532 nm was monitored every 20 s for 60 min. To test temperature and oxygen sensitivity of UCNS, 300 µl nanosensors were mixed with 300 µl KCl test solutions in screw-top quartz cuvettes. Measurements were made at room temperature and ambient oxygen concentration. Then, the

mixtures were either incubated at 37°C for 20 min or deoxygenated with N_2 for 20 min and measurements were made again.

5.3.4 Embedded nanosensor imaging

UCNS were prepared as described above and concentrated ~10x via ultrafiltration (Amicon Ultracel). Traditional downconversion nanosensors (KNS) were prepared as described in Dubach et al.,[175] swapping out potassium ionophore III for sodium ionophore X. The nanosensors were then concentrated ~10x via ultrafiltration. Biofilms growth procedures were adapted from methods by Kirchner et al. [110] and Jewell et al.[44] Briefly, *P. aeruginosa* strain PAO1 were plated onto Luria Bertani (LB) agar (Sigma-Aldrich, St. Louis, MO, USA) from frozen stocks and incubated at 37°C for 24 h. One colony was dispersed in 1 ml of LB broth and incubated for 24 h at 37°C. Liquid culture was diluted to an optical density (OD_{600}) of 0.05. Biofilms were grown statically in a 16.7% vol/vol solution of either UCNS or KNS in 10 mM HEPES/6mM Tris buffer mixed with LB broth (Sigma-Aldrich). A total of 600 µl of nanosensors + LB was added to each well of a 4-well LabTek chamber slide and then inoculated with an inoculation loopful of liquid *P. aeruginosa* culture at an OD_{600} of 0.05. Chamber slides were placed in a humidity chamber and incubated for 24 h at 37°C.

5.4 Results and Discussion

We chose the TTA-UC pair of PtOEP and DPA based on previous work by Islangulov et al.[176] and others[177-179] on embedding TTA-UC sensitizers and emitters in polymer films, polymer nanoparticles, and microemulsions. Our first step was optimizing the formulation of the TTA-UC system in our sensor matrix materials. Figure B.1 shows that using a platinum centered porphyrin (PtOEP) combined with DPA produced stronger upconversion luminescence than the similar palladium-based system (PdOEP/DPA) in the chosen PVC/soybean oil matrix when added at the

same concentrations. The soybean oil acted as both the plasticizer (replacing the more traditional DOS) and a protectant against oxygen quenching (Figure B.2).[162] However, the soybean oil's ability to scavenge oxygen radicals was not indefinite, which was seen in a loss of response by Day 3 after synthesis (Figure B.3).

Both PtOEP and DPA were incorporated into the ionophore-based nanosensor platform. Figure 5.1 illustrates the overlap of the TTA-UC emission spectrum and the absorbance spectra of the protonated and non-protonated states of the Blueberry dye.

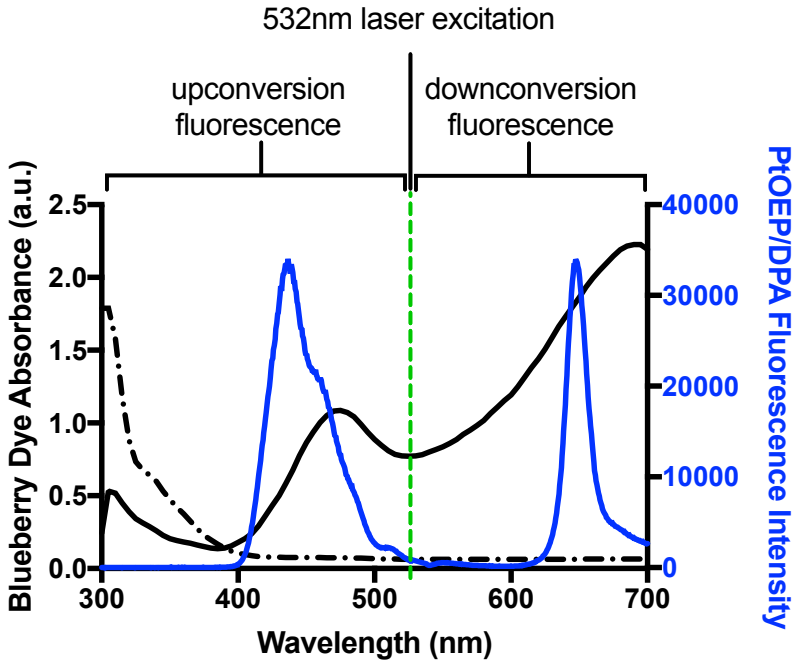

Figure 5.1 Blueberry dye absorbance spectra (black) in either protonated (black, dash-dot) or deprotonated (black, solid) state. TTA-UC spectra of PtOEP/DPA (blue) at 532 nm excitation shows excellent overlap between Blueberry dye absorbance peaks at 690 nm and 480 nm.

The mechanism of ion exchange for a system that contains Blueberry as the pH indicator are described in detail elsewhere.[180] The sensor mechanism is shown in Figure 5.2, where at low K^+ concentrations, the Blueberry dye is protonated (low absorbance) and the upconversion signal is not quenched. At higher K^+ concentrations, K^+ ions bind to the ionophore and protons from the

Blueberry dye are displaced to maintain electroneutrality. The deprotonated Blueberry has an absorbance peak at 480nm that overlaps with the PtOEP emission at 435 nm, gating the upconversion fluorescence. Previous work by Sahari et al.[172] determined that the apparent pK_a of Blueberry is 7.85, which is within the relevant range for biological applications.

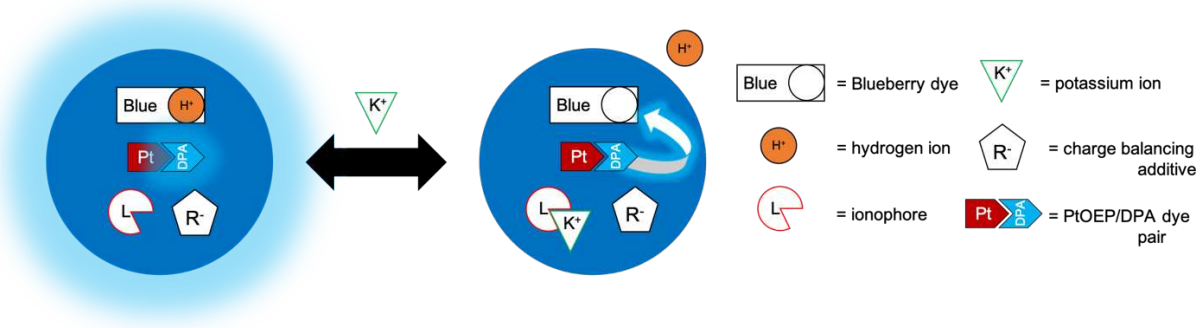

Figure 5.2 Schematic of nanosensor components co-loaded into the nanosensor matrix and fluorescence gating mechanism in response to decreasing potassium (K^+) concentrations.

Emission spectra of TTA-UC nanosensors fluorescence response to K^+ concentration in oxygenated conditions at 532 nm excitation (Figure 5.3) was calibrated from 10^{-8} M to 1 M K^+. The sensors have a response midpoint of 60 µM K^+ and a linear range of 8 µM to 260 µM. When deoxygenated, the UCNS have a response midpoint of 0.82 mM K^+. In deoxygenated conditions, the sensors have a linear range of 0.09 mM to 3.8 mM. The normalized response can be seen in Figure B.4. This difference in response may be because of differences in overall brightness or batch-to-batch variability.

Solutions of sodium, calcium, and magnesium chloride salts (0 M – 0.1 M) in HEPES/Tris were also tested (Figure 5.4) to evaluate UCNS selectivity and resulted in a response midpoint of 9.3mM $CaCl_2$ and 7mM for NaCl. Comparison of Ca^{2+} with the response midpoint for K^+ resulted in a selectivity coefficient (in $\log_{10}$ units) of -2.2. When comparing with the response midpoint for Na^+, the selectivity coefficient is -2.0.

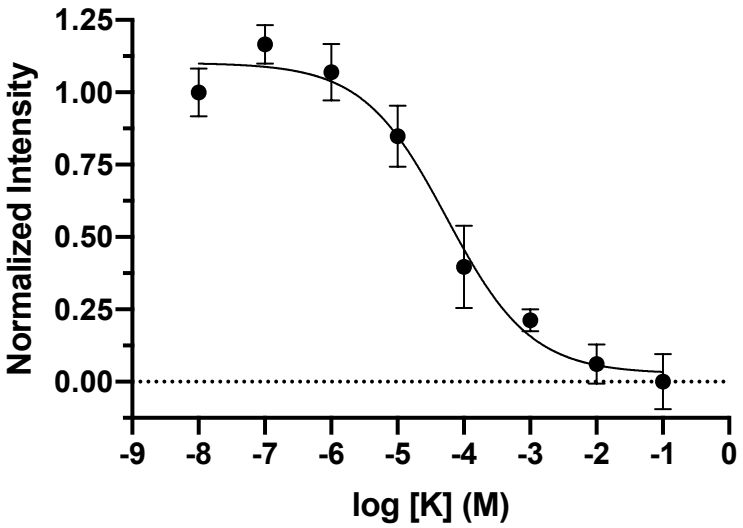

Figure 5.3 Normalized fluorescence intensity of UCNS response to KCl solution buffered in HEPES/Tris (pH = 7.4).

This is slightly larger than was found in optodes synthesized using potassium ionophore III by Shortreed et al.[181] Sahari et al.[172] noted increased selectivity for K^+ over Na^+ in K^+-selective nanosensors containing Blueberry dye that utilized traditional downconversion fluorescence. This indicates that there may be an interaction between K^+ ions and Blueberry. Compared with prior work,[146] the selectivity against calcium and magnesium for these sensors is slightly diminished, potentially as a results of the upconversion signaling groups. These sensors are thus selective against potentially interfering ions most commonly found in biological systems. This does not include potential interference from H^+ ions as the mechanism demonstrated here is inherently pH-dependent. However, as demonstrated in Figures 5.3 and 5.4, in a well-buffered *in vitro* environment these sensors respond primarily to K^+. These sensors could be made pH insensitive through the use of solvatochromic dyes as others have shown.[148, 149, 182, 183]

Figure B.11 shows a small temperature sensitivity at lower concentrations (increased intensities) that can be accounted for as long as calibration is performed under similar, controlled conditions. Similarly, there is some oxygen sensitivity that remains (Figure B.12) even with the

use of soybean oil as an oxygen scavenger. This prevents use in systems with a dynamic oxygen concentration, e.g. organoids, where oxygen is significantly diffusion limited. Potential improvements might include addition of another oxygen scavenger, such as BSA-dextran[162] or hyperbranched polyphosphates.[184]

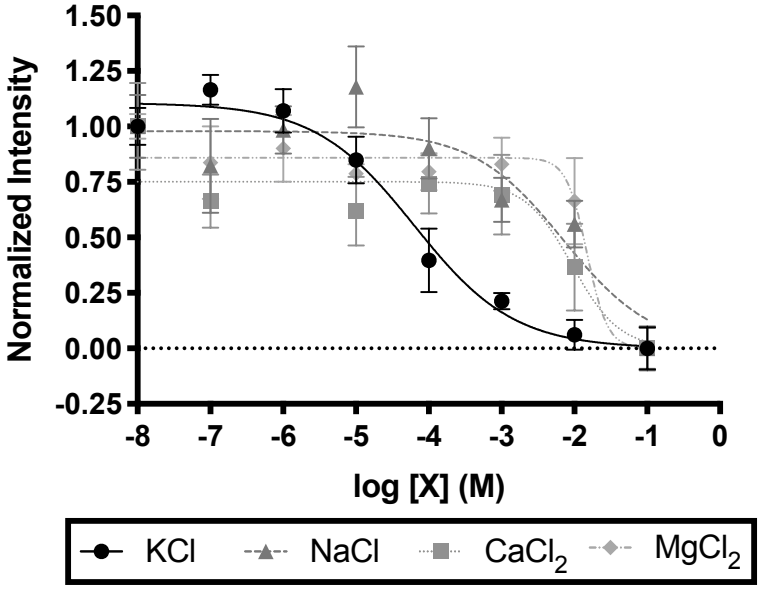

Figure 5.4 Normalized fluorescence intensity of UCNS response to NaCl, KCl, MgCl2 and CaCl2 solution buffered in HEPES/Tris (pH = 7.4).

As expected, the UCNS are reversible: demonstrated under controlled conditions using UCNS in 13 kD MWCO microdialysis fibers via confocal microscopy. Solutions of 10^{-8} M or 1 M KCl in HEPES/Tris (pH = 7.4) were added to the chamber slide wells containing fibers filled with UCNS. The fluorescence intensity at 400-450 nm (514 nm excitation) was measured to produce Figure 5.5. The 10^{-8} M to 1 M KCl cycles were repeated 3 times, with washes of HEPES/Tris buffer (pH = 7.4) in between each solution change. The signal intensity returns when the sensors are exposed to 10^{-8} M KCl after 1 M KCl exposure, so the UCNS are reversible, as expected based on the equilibrium-based sensing mechanism.[185] There is some loss of signal over the three cycles measured, which may be due to photobleaching (see Figure B.5).

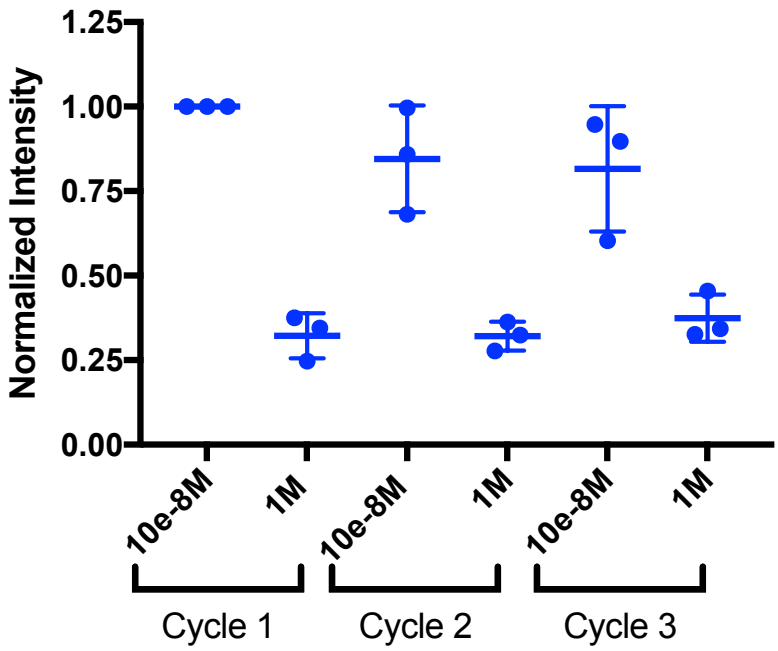

Figure 5.5 UCNS reversibility in dialysis tubes. Figure shows mean intensities of 3 trials of tubes for 3 washes of 0 M KCl and 3 washes of 1 M KCl demonstrating reversibility of the sensor mechanism. Error bars represent standard deviation.

We also determined the batch-to-batch variability between 4 sensor batches whose response curves are shown in Figure B.7. One-way ANOVA reveals no significant difference between the log of the response midpoint of each batch or the sensitivity (slope) of the response curve. This indicates that batches can be fabricated reproducibly as long as they are produced from the same initial optode. One point to note is that Galyean et al.[101] found that there was variance in Blueberry response between lots, which may account for variance between optodes that were synthesized with the Blueberry dye.

The shelf stability of the UCNS was determined based on both the potassium response curve as well as the nanosensor hydrodynamic diameter and zeta potential. All of these were monitored over 4 days and are shown in Figure B.3 and Table 5.1. The change in response midpoint observed coincides with a decrease in overall fluorescence intensity. By Day 4, there is only a

slight response to solutions of 0.1 M and 1 M KCl. It is believed that this is due to oxidative destruction of sensor components as the soybean oil loses its oxygen scavenging ability, or additive leakage, as the decrease in fluorescence intensity stabilizes by Day 3 but the change in response does not.

The only notable change in physical properties beyond the sensor response is an increase in hydrodynamic diameter by Day 4. The increase from approximately 105 nm to 124 nm is small but is statistically significant ($p < 0.05$). This may indicate that the nanoparticles are beginning to aggregate.

Table 5.1 Characterization of nanosensors on day 1, day 2, and day 4 with dynamic light scattering (DLS) and phase analysis light scattering (PALS).

	Eff. Diameter (nm)	Polydispersity	ζ Potential (mV)	Mobility ($\mu m\text{-}s^{-1}$/ $V\text{-}cm^{-1}$)	Log(EC_{50}) (M)
Day 1	105.6 ± 2.4	0.34 ± 0.01	-40.9 ± 1.8	-3.2 ± 0.1	-3.08 ± 0.15
Day 2	104.0 ± 5.9	0.33 ± 0.00_4	-46.2 ± 2.7	-3.6 ± 0.2	-3.01 ± 0.29
Day 4	123.8 ± 5.3	0.34 ± 0.00_4	-42.9 ± 3.4	-3.4 ± 0.3	-0.987 ± 0.15

The UCNS were compared with traditional downconversion nanosensors (KNS) in an *in vitro* biological system. Biofilms of *P. aeruginosa* strain PAO1 that express GFP were grown and incorporated either UCNS or KNS into their extracellular polymeric substance. The biofilms were imaged with confocal microscopy, and these images can be seen Figure 6. The emission spectra of the KNS, which overlaps with the GFP emission spectra, produces a significant amount of signal overlap that makes quantification of the KNS signal difficult. When the KNS are replaced with UCNS, the GFP and nanosensor signals can be imaged with minimal overlap.

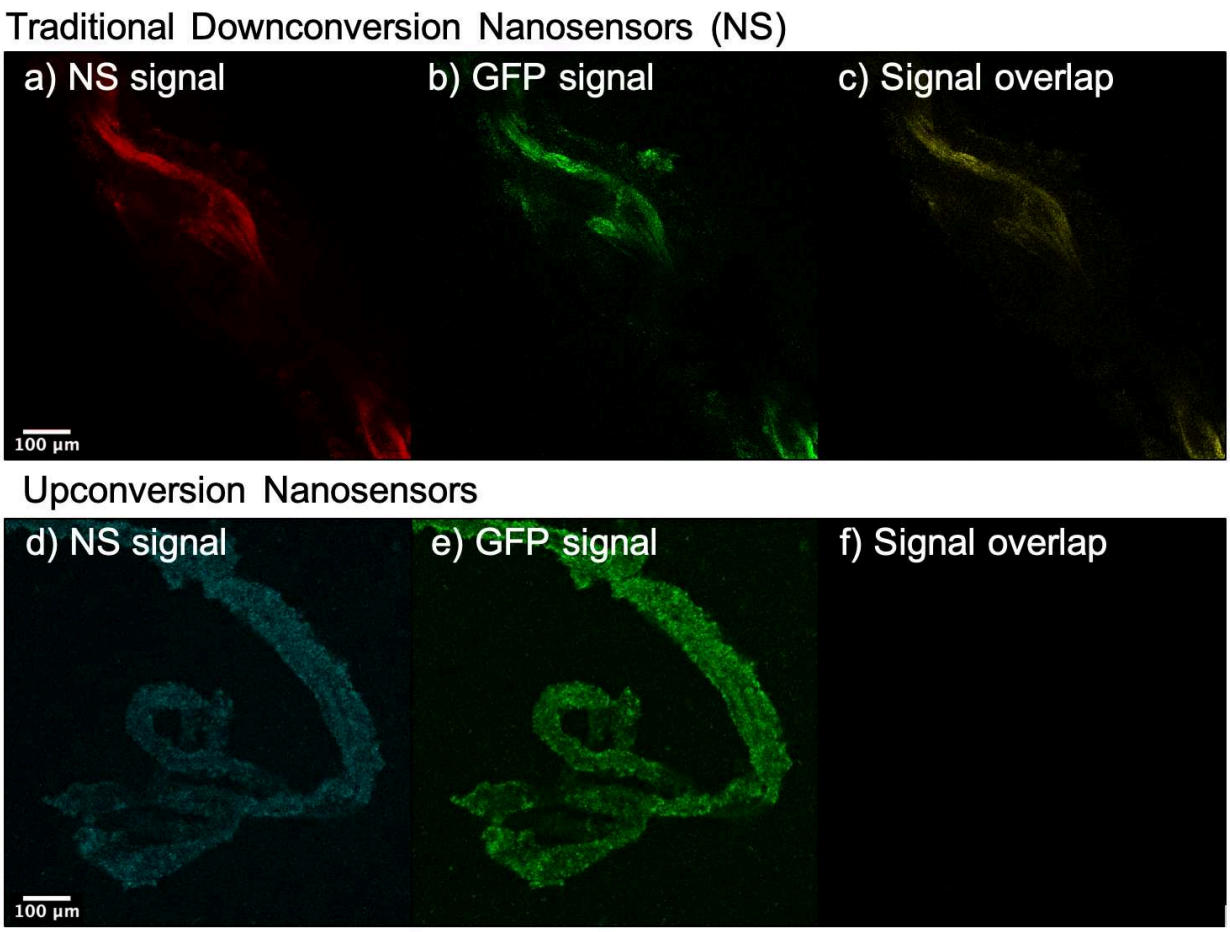

Figure 5.6 Top panel: Traditional downconversion nanosensors utilizing rhodamine B as one of the elements, embedded in a P. aeruginosa biofilm. a) Signal from the rhodamine B reporter, excited at 514nm and emission recorded over 535nm-632nm. b) Signal from GFP-expressing P. aeruginosa PAO1, excited at 488nm and emission recorded over 500-560nm. c) Signal overlap between GFP and rhodamine B, excited at 488nm and emission recorded over 540nm-590nm. Bottom panel: Upconversion nanosensors described in this manuscript embedded in a P. aeruginosa biofilm. d) Signal from PtOEP/DPA dye pair, excited at 514nm and emission recorded over 400nm-500nm. e) Signal from GFP-expressing P. aeruginosa PAO1 excited at 488nm and emission recorded over 500-600nm. f) Signal overlap between GFP and PtOEP/DPA dye pair, excited at 514nm and emission recorded over 490-515nm. This demonstrates that the upconversion signal successfully reduces the optical overlap.

5.5 Conclusions

Here, we have demonstrated a nanosensor platform to quantify potassium concentrations that incorporates triplet-triplet annihilation upconversion and a pH-sensitive quencher dye. These TTA-UC nanosensors are capable of sensing physiologically relevant K^+ concentrations, selective

against Na^+ and Ca^{2+}, reversible, and demonstrate a stable response for 3 days. Further work is needed to identify a reference dye that does not interact with the Blueberry dye or the TTA-UC process to allow for a ratiometric response. Because of the Blueberry dye's wide absorbance spectrum, an NIR or IR dye might make ratiometric measurements possible with low tissue interference. Alternatively, the pH dependent Blueberry dye might be replaced with a solvatochromic dye.[183] This would also eliminate any interference from pH changes within the system. This type of future work would allow for correction for environmental and nanosensor concentration changes and future *in vitro* and *in vivo* studies.

5.6 Acknowledgements

This work was supported by start up funds from Colorado School of Mines. Imaging experiments were performed in the University of Colorado Anschutz Medical Campus Advance Light Microscopy Core supported in part by NIH/NCATS Colorado CTSI Grant Number UL1 TR001082. Contents are the authors' sole responsibility and do not necessarily represent official NIH views.

CHAPTER 6

CONCLUSIONS AND FUTURE WORK

6.1 Conclusions

This thesis has described several advancements in monitoring bacterial biofilm dynamics. Investigating the movement and utilization of different metabolites within these complex microbial communities is crucial to expanding current understanding. In addition, these methods open up new avenues for development of clinical tools that can aid in improving outcomes related to biofilm infections. The oxygen nanosensors are not only a research tool that can elucidate 4D dynamics within live biofilms, but are also a promising clinical tool for testing the antibiotic susceptibility of biofilm-forming infections. The ability to use upconversion in a well-established system like ionophore-based optical sensors means that ion dynamics can now be monitored within biofilms without interference from common biological fluorescent reporters like GFP.

The scope of the work included here has been limited to the opportunistic pathogen *Pseudomonas aeruginosa*, but the technologies and methods developed here can be generalized to other species capable of forming a biofilm. In all cases, the engineering principles used in the rational design, analysis, and interpretation of these bioanalytical sensors remains the same.

6.2 Future Work

The works presented here are still the beginning of many other works in their respective fields. The following experiments are suggested as possible future work:

- *Bacterial response to nanoparticle size* – This work would aim to examine and control the interaction – specifically, uptake and sequestration - between bacteria in a biofilm and nanoparticles of varying sizes present in the growth media. Nanoparticles (and by extension, nanosensors) synthesized via nanoemulsion are produced as a wide distribution

of sizes, and there is some evidence that biofilm uptake of nanoparticles is primarily size-dependent.[186] This may affect the ensemble sensor response that is monitored and analyzed, and thus exploration of this would provide valuable insight. To achieve this, experiments to test viability and distribution of nanosensors with varying sizes would be performed in addition to experiments on how fractionation affects nanosensor response.

- *Oxygen consumption and antibiotic mechanism* – This work would aim to understand how the mechanism of action of different antibiotics affects oxygen dynamics within a biofilm. Different classes of antibiotics (e.g. cephalosporins, carbapenems, penicillins) produce either bactericidal or bacteriostatic activity using many different mechanisms, and bacterial response exhibits dependence on both concentration and exposure time. These can produce varying oxygen profiles that do not necessarily correspond to a traditional dose-response curve, especially during initial interrogation. Evaluation and analysis of these effects is necessary in order to use oxygen nanosensors as a general tool for evaluating antibiotic efficacy. Experiments would include time courses of serially-diluted antibiotics to understand kinetic activity of representative drugs from each class of antibiotics. In addition, extensive work would be done on a general method of automated data processing that yields consistent, reliable results.
- *Potassium transients in biofilms* – Another interesting avenue of investigation is the relationship of transient potassium gradients around biofilms and cellular motility. It has been established that *Bacillus subtilis* biofilms produce membrane potential oscillations by altering local K^+ concentrations. This attracts nearby planktonic bacteria to the biofilm in a way that appears to be species-independent. The suggested mechanism is that this signal affects the cell's motility and it responds by moving towards the signal source. In order to

validate this mechanism, it is necessary to establish a link between cell motility and speed and extracellular potassium concentration. Experiments would include time lapse imaging of planktonic bacteria and potassium nanosensors exposed to both solutions with static K^+ concentrations as well as artificially created K^+ concentration gradients. Comparison of motility between bacteria of different species as well as knockdowns of those species with reduced K^+ ion channel activity would be beneficial.

REFERENCES

1. Rong, G.; Corrie, S. R.; Clark, H. A., In Vivo Biosensing: Progress and Perspectives. *ACS Sensors* **2017,** *2* (3), 327–338.

2. Ruckh, T. T.; Clark, H. A., Implantable nanosensors: Toward continuous physiologic monitoring. *Analytical Chemistry* **2014,** *86* (3), 1314-1323.

3. Dai, Y. P.; Ji, Z. P.; Wang, C. Y.; Hu, X. Y.; Wang, G. X., Microcantilever Biosensors. *Progress in Chemistry* **2016,** *28* (5), 697-710.

4. Fogel, R.; Limson, J.; Seshia, A. A., Acoustic biosensors. In *Biosensor Technologies for Detection of Biomolecules*, Estrela, P., Ed. Portland Press Ltd: London, 2016; Vol. 60, pp 101-110.

5. Xu, P. C.; Li, X. X.; Yu, H. T.; Xu, T. G., Advanced Nanoporous Materials for Micro-Gravimetric Sensing to Trace-Level Bio/Chemical Molecules. *Sensors* **2014,** *14* (10), 19023-19056.

6. Munawar, A.; Ong, Y. R.; Schirhagl, R.; Tahir, M. A.; Khan, W. S.; Bajwa, S. Z., Nanosensors for diagnosis with optical, electric and mechanical transducers. *Rsc Advances* **2019,** *9* (12), 6793-6803.

7. Bakker, E.; Buhlmann, P.; Pretsch, E., Carrier-Based Ion-Selective Electrodes and Bulk Optodes. 1. General Characteristics. *Chem. Rev.* **1997,** *97* (8), 3083-3132.

8. Xie, X. J.; Bakker, E., Ion selective optodes: from the bulk to the nanoscale. *Analytical and Bioanalytical Chemistry* **2015,** *407* (14), 3899-3910.

9. Johnson, R. D.; Bachas, L. G., Ionophore-based ion-selective potentiometric and optical sensors. *Anal Bioanal Chem* **2003,** *376* (3), 328-41.

10. Yu, T.; Bishop, P. L., Stratification and oxidation-reduction potential change in an aerobic and sulfate-reducing biofilm studied using microelectrodes. *Water Environment Research* **2001,** *73* (3), 368-373.

11. Xie, X. J.; Zhai, J. Y.; Crespo, G. A.; Bakker, E., Ionophore-Based Ion-Selective Optical NanoSensors Operating in Exhaustive Sensing Mode. *Analytical Chemistry* **2014,** *86* (17), 8770-8775.

12. Mistlberger, G.; Crespo, G. A.; Bakker, E., Ionophore-Based Optical Sensors. In *Annual Review of Analytical Chemistry, Vol 7*, Cooks, R. G.; Pemberton, J. E., Eds. Annual Reviews: Palo Alto, 2014; Vol. 7, pp 483-512.

13. Abdelfattah, A. S.; Kawashima, T.; Singh, A.; Novak, O.; Liu, H.; Shuai, Y. C.; Huang, Y. C.; Campagnola, L.; Seeman, S. C.; Yu, J. N.; Zheng, J. H.; Grimm, J. B.; Patel, R.; Friedrich, J.; Mensh, B. D.; Paninski, L.; Macklin, J. J.; Murphy, G. J.; Podgorski, K.; Lin, B. J.; Chen, T. W.; Turner, G. C.; Liu, Z.; Koyama, M.; Svoboda, K.; Ahrens, M. B.; Lavis, L. D.; Schreiter, E. R., Bright and photostable chemigenetic indicators for extended in vivo voltage imaging. *Science* **2019,** *365* (6454), 699-+.

14. Peixoto, A. C.; Silva, A. F., 11 - Smart devices: Micro- and nanosensors. In *Bioinspired Materials for Medical Applications*, Rodrigues, L.; Mota, M., Eds. Woodhead Publishing: 2017; pp 297-329.

15. Wolfbeis, O. S., Luminescent sensing and imaging of oxygen: Fierce competition to the Clark electrode. *BioEssays* **2015,** *37* (8), 921-928.

16. Wang, X. D.; Wolfbeis, O. S., Optical methods for sensing and imaging oxygen: materials, spectroscopies and applications. *Chemical Society Reviews* **2014,** *43* (10), 3666-3761.

17. Venkatanarayanan, A.; Spain, E., 13.03 - Review of Recent Developments in Sensing Materials. In *Comprehensive Materials Processing*, Hashmi, S.; Batalha, G. F.; Van Tyne, C. J.; Yilbas, B., Eds. Elsevier: Oxford, 2014; pp 47-101.

18. Ferris, M. S.; Elms, M. K.; Cash, K. J., Enzyme-conjugated nanosensors with tunable detection limits for small biomolecule determination. *Aiche Journal* **2019,** *65* (9), 9.

19. Cash, K. J.; Clark, H. A., *In Vivo* Histamine Optical Nanosensors. *Sensors (Basel)* **2012,** *12* (9), 11922-11932.

20. Seiler, K.; Simon, W., Theoretical aspects of bulk optode membranes. *Anal. Chim. Acta* **1992,** *266*, 73-87.

21. Hall-Stoodley, L.; Costerton, J. W.; Stoodley, P., Bacterial biofilms: From the natural environment to infectious diseases. *Nature Reviews Microbiology* **2004,** *2* (2), 95-108.

22. Fischer, M.; Triggs, G. J.; Krauss, T. F., Optical Sensing of Microbial Life on Surfaces. *Applied and Environmental Microbiology* **2016,** *82* (5), 1362-1371.

23. Neu, T. R.; Lawrence, J. R., Innovative techniques, sensors, and approaches for imaging biofilms at different scales. *Trends in Microbiology* **2015,** *23* (4), 233-242.

24. Prevoteau, A.; Rabaey, K., Electroactive Biofilms for Sensing: Reflections and Perspectives. *Acs Sensors* **2017,** *2* (8), 1072-1085.

25. Yang, H. J.; Zhou, M. H.; Liu, M. M.; Yang, W. L.; Gu, T. Y., Microbial fuel cells for biosensor applications. *Biotechnology Letters* **2015,** *37* (12), 2357-2364.

26. Stewart, P. S.; Franklin, M. J., Physiological heterogeneity in biofilms. *Nature Reviews Microbiology* **2008,** *6* (3), 199-210.

27. Grote, J.; Krysciak, D.; Streit, W. R., Phenotypic Heterogeneity, a Phenomenon That May Explain Why Quorum Sensing Does Not Always Result in Truly Homogenous Cell Behavior. *Applied and environmental microbiology* **2015,** *81* (16), 5280-5289.

28. Magana, M.; Sereti, C.; Ioannidis, A.; Mitchell, C. A.; Ball, A. R.; Magiorkinis, E.; Chatzipanagiotou, S.; Hamblin, M. R.; Hadjifrangiskou, M.; Tegos, G. P., Options and Limitations in Clinical Investigation of Bacterial Biofilms. *Clinical Microbiology Reviews* **2018,** *31* (3), 49.

29. Wilking, J. N.; Zaburdaev, V.; De Volder, M.; Losick, R.; Brenner, M. P.; Weitz, D. A., Liquid transport facilitated by channels in *Bacillus subtilis* biofilms. *Proceedings of the National Academy of Sciences* **2013,** *110* (3), 848.

30. Xu, K. D.; Stewart, P. S.; Xia, F.; Huang, C. T.; McFeters, G. A., Spatial physiological heterogeneity in Pseudomonas aeruginosa biofilm is determined by oxygen availability. *Applied and Environmental Microbiology* **1998,** *64* (10), 4035-4039.

31. Stetter, J. R.; Li, J., Amperometric Gas Sensors: A Review. *Chemical Reviews* **2008,** *108* (2), 352-366.

32. Wei, Y.; Jiao, Y.; An, D.; Li, D.; Li, W.; Wei, Q., Review of Dissolved Oxygen Detection Technology: From Laboratory Analysis to Online Intelligent Detection. *Sensors (Basel, Switzerland)* **2019,** *19* (18), 3995.

33. Whalen, W.; Bungay, H.; Sanders, W., Microelectrode determination of oxygen profiles in microbial slime systems. *Environmental Science & Technology* **1969,** *3* (12), 1297.

34. Kiamco, M. M.; Atci, E.; Mohamed, A.; Call, D. R.; Beyenal, H., Hyperosmotic Agents and Antibiotics Affect Dissolved Oxygen and pH Concentration Gradients in Staphylococcus aureus Biofilms. *Appl Environ Microbiol* **2017,** *83* (6), in press.

35. Rincon, S. M.; Urrego, N. F.; Avila, K. J.; Romero, H. M.; Beyenal, H., Photosynthetic activity assessment in mixotrophically cultured Chlorella vulgaris biofilms at various developmental stages. *Algal Research* **2019,** *38*, 101408.

36. Moya, A.; Guimera, X.; del Campo, F. J.; Prats-Alfonso, E.; Dorado, A.; Baeza, M.; Villa, R.; Gabriel, D.; Gamisans, X.; Gabriel, G., Profiling of oxygen in biofilms using individually addressable disk microelectrodes on a microfabricated needle. *Microchimica Acta* **2015,** *182* (5-6), 985-993.

37. Moßhammer, M.; Strobl, M.; Kühl, M.; Klimant, I.; Borisov, S. M.; Koren, K., Design and Application of an Optical Sensor for Simultaneous Imaging of pH and Dissolved O2 with Low Cross-Talk. *ACS Sensors* **2016,** *1* (6), 681-687.

38. Staal, M.; Prest, E. I.; Vrouwenvelder, J. S.; Rickelt, L. F.; Kuhl, M., A simple optode based method for imaging O-2 distribution and dynamics in tap water biofilms. *Water Research* **2011,** *45* (16), 5027-5037.

39. Staal, M.; Borisov, S. M.; Rickelt, L. F.; Klimant, I.; Kühl, M., Ultrabright planar optodes for luminescence life-time based microscopic imaging of O2 dynamics in biofilms. *Journal of Microbiological Methods* **2011,** *85* (1), 67-74.

40. Sasaki, S.; Mochizuki, M.; Igarashi, M., Development of a Bioluminescent Bacteria Sheet for the Measurement of Oxygen Concentration. *Analytical Sciences* **2013,** *29* (2), 267-269.

41. Boyce, M. W.; Kenney, R. M.; Truong, A. S.; Lockett, M. R., Quantifying oxygen in paper-based cell cultures with luminescent thin film sensors. *Analytical and Bioanalytical Chemistry* **2016,** *408* (11), 2985-2992.

42. Acosta, M. A.; Ymele-Leki, P.; Kostov, Y. V.; Leach, J. B., Fluorescent microparticles for sensing cell microenvironment oxygen levels within 3D scaffolds. *Biomaterials* **2009,** *30* (17), 3068-3074.

43. Acosta Miguel, A.; Velasquez, M.; Williams, K.; Ross Julia, M.; Leach Jennie, B., Fluorescent silica particles for monitoring oxygen levels in three-dimensional heterogeneous cellular structures. *Biotechnology and Bioengineering* **2012,** *109* (10), 2663-2670.

44. Jewell, M. P.; Galyean, A. A.; Kirk Harris, J.; Zemanick, E. T.; Cash, K. J., Luminescent Nanosensors for Ratiometric Monitoring of Three-Dimensional Oxygen Gradients in Laboratory and Clinical *Pseudomonas aeruginosa* Biofilms. *Applied and Environmental Microbiology* **2019,** *85* (20), e01116-19.

45. Joshi, V. S.; Sheet, P. S.; Cullin, N.; Kreth, J.; Koley, D., Real-Time Metabolic Interactions between Two Bacterial Species Using a Carbon-Based pH Microsensor as a Scanning Electrochemical Microscopy Probe. *Analytical Chemistry* **2017,** *89* (20), 11044-11052.

46. Bause, S.; Decker, M.; Gerlach, F.; Nather, J.; Koster, F.; Neubauer, P.; Vonau, W., Development of an iridium-based pH sensor for bioanalytical applications. *Journal of Solid State Electrochemistry* **2018,** *22* (1), 51-60.

47. Gashti, M. P.; Asselin, J.; Barbeau, J.; Boudreau, D.; Greener, J., A microfluidic platform with pH imaging for chemical and hydrodynamic stimulation of intact oral biofilms. *Lab on a Chip* **2016,** *16* (8), 1412-1419.

48. Schlafer, S.; Baelum, V.; Dige, I., Improved pH-ratiometry for the three-dimensional mapping of pH microenvironments in biofilms under flow conditions. *Journal of Microbiological Methods* **2018,** *152*, 194-200.

49. Schlafer, S.; Dige, I., Ratiometric Imaging of Extracellular pH in Dental Biofilms. *Jove-Journal of Visualized Experiments* **2016,** (109), 7.

50. Dige, I.; Baelum, V.; Nyvad, B.; Schlafer, S., Monitoring of extracellular pH in young dental biofilms grown in vivo in the presence and absence of sucrose. *Journal of Oral Microbiology* **2016,** *8*, 8.

51. Guo, L. H.; Hu, W.; He, X. S.; Lux, R.; McLean, J.; Shi, W. Y., Investigating Acid Production by Streptococcus mutans with a Surface-Displayed pH-Sensitive Green Fluorescent Protein. *Plos One* **2013,** *8* (2), 10.

52. Chen, M.; Xin, X.; Liu, H. M.; Wu, Y. W.; Zhong, N. B.; Chang, H. X., Monitoring Biohydrogen Production and Metabolic Heat in Biofilms by Fiber Bragg Grating Sensors. *Analytical Chemistry* **2019,** *91* (12), 7842-7849.

53. Reyes-Romero, D. F.; Behrmann, O.; Dame, G.; Urban, G. A., Dynamic thermal sensor for biofilm monitoring. *Sensors and Actuators a-Physical* **2014,** *213*, 43-51.

54. Morais, F. M.; Buchholz, F.; Hartmann, T.; Lerchner, J.; Neu, T. R.; Kiesel, B.; Harms, H.; Maskow, T., Chip-calorimetric monitoring of biofilm eradication with bacteriophages reveals an unexpected infection-related heat profile. *Journal of Thermal Analysis and Calorimetry* **2014,** *115* (3), 2203-2210.

55. Mariana, F.; Buchholz, F.; Lerchner, J.; Neu, T. R.; Harms, H.; Maskow, T., Chip-calorimetric monitoring of biofilm eradication with antibiotics provides mechanistic information. *International Journal of Medical Microbiology* **2013,** *303* (3), 158-165.

56. deBeer, D.; Schramm, A.; Santegoeds, C. M.; Kuhl, M., A nitrite microsensor for profiling environmental biofilms. *Applied and Environmental Microbiology* **1997,** *63* (3), 973-977.

57. Hao, L.; Li, J.; Kappler, A.; Obst, M., Mapping of Heavy Metal Ion Sorption to Cell-Extracellular Polymeric Substance-Mineral Aggregates by Using Metal-Selective Fluorescent Probes and Confocal Laser Scanning Microscopy. *Applied and Environmental Microbiology* **2013,** *79* (21), 6524-6534.

58. Shumi, W.; Lim, J.; Nam, S. W.; Kim, S. H.; Cho, K. S.; Yoon, J.; Park, S., Fluorescence Imaging of the Spatial Distribution of Ferric Ions over Biofilms Formed by Streptococcus mutans under Microfluidic Conditions. *Biochip Journal* **2009,** *3* (2), 119-124.

59. Prindle, A.; Liu, J. T.; Asally, M.; Ly, S.; Garcia-Ojalvo, J.; Suel, G. M., Ion channels enable electrical communication in bacterial communities. *Nature* **2015,** *527* (7576), 59-63.

60. Bruni, G. N.; Weekley, R. A.; Dodd, B. J. T.; Kralj, J. M., Voltage-gated calcium flux mediates *Escherichia coli* mechanosensation. *Proceedings of the National Academy of Sciences* **2017,** *114* (35), 9445.

61. Das, S.; Sarkar, H. S.; Uddin, M. R.; Mandal, S.; Sahoo, P., A chemosensor to recognize N-acyl homoserine lactone in bacterial biofilm. *Sensors and Actuators B: Chemical* **2018,** *259*, 332-338.

62. Struss, A.; Pasini, P.; Ensor, C. M.; Raut, N.; Daunert, S., Paper Strip Whole Cell Biosensors: A Portable Test for the Semiquantitative Detection of Bacterial Quorum Signaling Molecules. *Analytical Chemistry* **2010,** *82* (11), 4457-4463.

63. Wang, X. C.; Wilson, S. C.; Hammond, M. C., Next-generation RNA-based fluorescent biosensors enable anaerobic detection of cyclic di-GMP. *Nucleic Acids Research* **2016,** *44* (17), 10.

64. Xie, Q. Y.; Zhao, F. L.; Liu, H. R.; Shan, Y. K.; Liu, F., A label-free and self-assembled electrochemical biosensor for highly sensitive detection of cyclic diguanylate monophosphate (c-di-GMP) based on RNA riboswitch. *Analytica Chimica Acta* **2015,** *882*, 22-26.

65. Dippel, A. B.; Anderson, W. A.; Evans, R. S.; Deutsch, S.; Hammond, M. C., Chemiluminescent Biosensors for Detection of Second Messenger Cyclic di-GMP. *ACS Chemical Biology* **2018,** *13* (7), 1872-1879.

66. Atci, E.; Babauta, J. T.; Ha, P. T.; Beyenal, H., A Fumarate Microbiosensor for Use in Biofilms. *Journal of the Electrochemical Society* **2017,** *164* (3), H3058-H3064.

67. Atci, E.; Babauta, J. T.; Sultana, S. T.; Beyenal, H., Microbiosensor for the detection of acetate in electrode-respiring biofilms. *Biosensors & Bioelectronics* **2016,** *81*, 517-523.

68. Liu, X.; Ramsey, M. M.; Chen, X.; Koley, D.; Whiteley, M.; Bard, A. J., Real-time mapping of a hydrogen peroxide concentration profile across a polymicrobial bacterial biofilm using scanning electrochemical microscopy. *Proceedings of the National Academy of Sciences* **2011,** *108* (7), 2668.

69. Koley, D.; Ramsey, M. M.; Bard, A. J.; Whiteley, M., Discovery of a biofilm electrocline using real-time 3D metabolite analysis. *Proceedings of the National Academy of Sciences* **2011,** *108* (50), 19996.

70. Krige, A.; Sjoblom, M.; Ramser, K.; Christakopoulos, P.; Rova, U., On-Line Raman Spectroscopic Study of Cytochromes' Redox State of Biofilms in Microbial Fuel Cells. *Molecules* **2019,** *24* (3), 14.

71. Schaule, G.; Flemming, H. C., microbial deterioration of materials - biofilm and biofouling - quantification of respiratory active bacteria in water and in biofilms by

means of a fluorescent redox dye. *Werkstoffe Und Korrosion-Materials and Corrosion* **1994,** *45* (1), 54-57.

72. Ibarlucea, B.; Rim, T.; Baek, C. K.; de Visser, J.; Baraban, L.; Cuniberti, G., Nanowire sensors monitor bacterial growth kinetics and response to antibiotics. *Lab on a Chip* **2017,** *17* (24), 4283-4293.

73. Ishiguro, K.; Washio, J.; Sasaki, K.; Takahashi, N., Real-time monitoring of the metabolic activity of periodontopathic bacteria. *Journal of Microbiological Methods* **2015,** *115*, 22-26.

74. Zhong, N.; Wu, Y.; Wang, Z.; Chang, H.; Zhong, D.; Xu, Y.; Hu, X.; Huang, L., Monitoring Microalgal Biofilm Growth and Phenol Degradation with Fiber-Optic Sensors. *Analytical Chemistry* **2019,** *91* (23), 15155-15162.

75. Paredes, J.; Becerro, S.; Arizti, F.; Aguinaga, A.; Del Pozo, J. L.; Arana, S., Interdigitated microelectrode biosensor for bacterial biofilm growth monitoring by impedance spectroscopy technique in 96-well microtiter plates. *Sensors and Actuators B-Chemical* **2013,** *178*, 663-670.

76. Nadell, C. D.; Drescher, K.; Foster, K. R., Spatial structure, cooperation, and competition in bacterial biofilms. *Nature Reviews Microbiology* **2016,** *14*, 589-600.

77. Hoiby, N.; Flensborg, E. W.; Beck, B.; Friis, B.; Jacobsen, S. V.; Jacobsen, L., Pseudomonas aeruginosa infection in cystic fibrosis. Diagnostic and prognostic significance of Pseudomonas aeruginosa precipitins determined by means of crossed immunoelectrophoresis. *Scand J Respir Dis* **1977,** *58* (2), 65-79.

78. Burns, J. L.; Ramsey, B. W.; Smith, A. L., Clinical manifestations and treatment of pulmonary infections in cystic fibrosis. *Advances in pediatric infectious diseases* **1993,** *8*, 53-66.

79. Hamed, K.; Debonnett, L., Tobramycin inhalation powder for the treatment of pulmonary Pseudomonas aeruginosa infection in patients with cystic fibrosis: a review based on clinical evidence. *Therapeutic Advances in Respiratory Disease* **2017,** *11* (5), 193-209.

80. Macia, M. D.; Rojo-Molinero, E.; Oliver, A., Antimicrobial susceptibility testing in biofilm-growing bacteria. *Clinical Microbiology and Infection* **2014,** *20* (10), 981-990.

81. Douterelo, I.; Jackson, M.; Solomon, C.; Boxall, J., Spatial and temporal analogies in microbial communities in natural drinking water biofilms. *Science of The Total Environment* **2017,** *581-582*, 277-288.

82. Besemer, K.; Singer, G.; Hödl, I.; Battin, T. J., Bacterial Community Composition of Stream Biofilms in Spatially Variable-Flow Environments. *Applied and Environmental Microbiology* **2009,** *75* (22), 7189.

83. Drennan, D. M.; Almstrand, R.; Ladderud, J.; Lee, I.; Landkamer, L.; Figueroa, L.; Sharp, J. O., Spatial impacts of inorganic ligand availability and localized microbial community structure on mitigation of zinc laden mine water in sulfate-reducing bioreactors. *Water Research* **2017,** *115*, 50-59.

84. Osmond, M.; Bernier, S. M.; Pantcheva, M. B.; Krebs, M. D., Collagen and collagen-chondroitin sulfate scaffolds with uniaxially aligned pores for the biomimetic, three dimensional culture of trabecular meshwork cells. *Biotechnology and Bioengineering* **2017,** *114* (4), 915-923.

85. Kim, R.; Wang, Y. L.; Hwang, S. H. J.; Attayek, P. J.; Smiddy, N. M.; Reed, M. I.; Sims, C. E.; Allbritton, N. L., Formation of arrays of planar, murine, intestinal crypts possessing a stem/proliferative cell compartment and differentiated cell zone. *Lab on a Chip* **2018,** *18* (15), 2202-2213.

86. Harris, D.; Ummadi, J. G.; Thurber, A. R.; Allau, Y.; Verba, C.; Colwell, F.; Torres, M. E.; Koley, D., Real-time monitoring of calcification process by Sporosarcina pasteurii biofilm. *Analyst* **2016,** *141* (10), 2887-2895.

87. Walters, M. C.; Roe, F.; Bugnicourt, A.; Franklin, M. J.; Stewart, P. S., Contributions of antibiotic penetration, oxygen limitation, and low metabolic activity to tolerance of Pseudomonas aeruginosa biofilms to ciprofloxacin and tobramycin. *Antimicrobial Agents and Chemotherapy* **2003,** *47* (1), 317-323.

88. Yu, S.; Wei, Q.; Zhao, T.; Guo, Y.; Ma, L. Z., A Survival Strategy for Pseudomonas aeruginosa That Uses Exopolysaccharides To Sequester and Store Iron To Stimulate Psl-Dependent Biofilm Formation. *Applied and Environmental Microbiology* **2016,** *82* (21), 6403.

89. Li, J.; Bishop, P. L., Time course observations of nitrifying biofilm development using microelectrodes. *J. Environ. Eng. Sci.* **2004,** *3*.

90. Billings, N.; Birjiniuk, A.; Samad, T. S.; Doyle, P. S.; Ribbeck, K., Material properties of biofilms-a review of methods for understanding permeability and mechanics. *Reports on Progress in Physics* **2015,** *78* (3).

91. Bungay, H.; Whalen, W.; Sanders, W., Microprobe techniques for determining diffusivities and respiration rates in microbial slime systems. *Biotechnology and bioengineering* **1969,** *11* (5), 765.

92. Hidalgo, G.; Burns, A.; Herz, E.; Hay, A. G.; Houston, P. L.; Wiesner, U.; Lion, L. W., Functional Tomographic Fluorescence Imaging of pH Microenvironments in Microbial Biofilms by Use of Silica Nanoparticle Sensors. *Applied and Environmental Microbiology* **2009,** *75* (23), 7426-7435.

93. Kenney, R. M.; Boyce, M. W.; Whitman, N. A.; Kromhout, B. P.; Lockett, M. R., A pH-Sensing Optode for Mapping Spatiotemporal Gradients in 3D Paper-Based Cell Cultures. *Analytical Chemistry* **2018,** *90* (3), 2376-2383.

94. Rivera, K. R.; Pozdin, V. A.; Young, A. T.; Erb, P. D.; Wisniewski, N. A.; Magness, S. T.; Daniele, M., Integrated phosphorescence-based photonic biosensor (iPOB) for monitoring oxygen levels in 3D cell culture systems. *Biosensors and Bioelectronics* **2018**.

95. Bland, E.; Burg, K. J. L., Fluorescence ratio imaging for oxygen measurement in a tissue engineered construct. *Journal of Histotechnology* **2013,** *36* (4), 119-127.

96. Rubol, S.; Freixa, A.; Sanchez-Vila, X.; Romaní, A. M., Linking biofilm spatial structure to real-time microscopic oxygen decay imaging. *Biofouling* **2018,** *34* (2), 200-211.

97. Kühl, M.; Rickelt, L. F.; Thar, R., Combined Imaging of Bacteria and Oxygen in Biofilms. *Applied and Environmental Microbiology* **2007,** *73* (19), 6289.

98. Holst, G.; Kohls, O.; Klimant, I.; König, B.; Kühl, M.; Richter, T., A modular luminescence lifetime imaging system for mapping oxygen distribution in biological samples. *Sensors and Actuators B: Chemical* **1998,** *51* (1), 163-170.

99. Cash, K. J.; Li, C.; Xia, J.; Wang, L. V.; Clark, H. A., Optical Drug Monitoring: Photoacoustic Imaging of Nanosensors to Monitor Therapeutic Lithium in Vivo. *Acs Nano* **2015,** *9* (2), 1692-1698.

100. Ruckh, T. T.; Skipwith, C. G.; Chang, W. D.; Senko, A. W.; Bulovic, V.; Anikeeva, P. O.; Clark, H. A., Ion-Switchable Quantum Dot Forster Resonance Energy Transfer Rates in Ratiometric Potassium Sensors. *Acs Nano* **2016,** *10* (4), 4020-4030.

101. Galyean, A. A.; Behr, M. R.; Cash, K. J., Ionophore-based optical nanosensors incorporating hydrophobic carbon dots and a pH-sensitive quencher dye for sodium detection. *Analyst* **2018,** *143*, 458-465.

102. Cash, K. J.; Clark, H. A., Phosphorescent Nanosensors for *In Vivo* Tracking of Histamine Levels. *Anal. Chem.* **2013,** *85* (13), 6312-6318.

103. Ferris, M. S.; Katageri, A. G.; Gohring, G. M.; Cash, K. J., A dual-indicator strategy for controlling the response of ionophore-based optical nanosensors. *Sensors and Actuators B: Chemical* **2018,** *256*, 674-681.

104. Paredes, R. M.; Etzler, J. C.; Watts, L. T.; Zheng, W.; Lechleiter, J. D., Chemical calcium indicators. *Methods* **2008,** *46* (3), 143-151.

105. Yang, Z. G.; Cao, J. F.; He, Y. X.; Yang, J. H.; Kim, T.; Peng, X. J.; Kim, J. S., Macro-/micro-environment-sensitive chemosensing and biological imaging. *Chemical Society Reviews* **2014,** *43* (13), 4563-4601.

106. Li, X.; Gao, X.; Shi, W.; Ma, H., Design Strategies for Water-Soluble Small Molecular Chromogenic and Fluorogenic Probes. *Chemical Reviews* **2014,** *114* (1), 590-659.

107. Fletcher, N. A.; Babcock, L. R.; Murray, E. A.; Krebs, M. D., Controlled delivery of antibodies from injectable hydrogels. *Materials Science and Engineering: C* **2016,** *59*, 801-806.

108. Baumann, R. P.; Penketh, P. G.; Seow, H. A.; Shyam, K.; Sartorelli, A. C., Generation of Oxygen Deficiency in Cell Culture Using a Two-Enzyme System to Evaluate Agents Targeting Hypoxic Tumor Cells. *Radiation Research* **2008,** *170* (5), 651-660.

109. Keizer, J., Nonlinear fluorescence quenching and the origin of positive curvature in Stern-Volmer plots. *Journal of the American Chemical Society* **1983,** *105* (6), 1494-1498.

110. Kirchner, S.; Fothergill, J. L.; Wright, E. A.; James, C. E.; Mowat, E.; Winstanley, C., Use of Artificial Sputum Medium to Test Antibiotic Efficacy Against Pseudomonas aeruginosa in Conditions More Relevant to the Cystic Fibrosis Lung. *Jove-Journal of Visualized Experiments* **2012,** (64), 7.

111. Lee, S.-K.; Okura, I., Photostable Optical Oxygen Sensing Material: Platinum Tetrakis(pentafluorophenyl)porphyrin Immobilized in Polystyrene. *Analytical Communications* **1997,** *34* (6), 185-188.

112. Lian, J.; Chan, R.; Lam, K.; Costerton, J. W., Production of mucoid microcolonies by Pseudomonas aeruginosa within infected lungs in cystic fibrosis. *Infection and Immunity* **1980,** *28*, 546-556.

113. Worlitzsch, D.; Tarran, R.; Ulrich, M.; Schwab, U.; Cekici, A.; Meyer, K. C.; Birrer, P.; Bellon, G.; Berger, J.; Weiss, T.; Botzenhart, K.; Yankaskas, J. R.; Randell, S.; Boucher, R. C.; Döring, G., Effects of reduced mucus oxygen concentration in airway Pseudomonas infections of cystic fibrosis patients. *The Journal of clinical investigation* **2002,** *109* (3), 317-325.

114. Zhang, C.; Li, B.; Tang, J.-Y.; Wang, X.-L.; Qin, Z.; Feng, X.-Q., Experimental and theoretical studies on the morphogenesis of bacterial biofilms. *Soft Matter* **2017,** *13* (40), 7389-7397.

115. Dietrich, L. E. P.; Okegbe, C.; Price-Whelan, A.; Sakhtah, H.; Hunter, R. C.; Newman, D. K., Bacterial Community Morphogenesis Is Intimately Linked to the Intracellular Redox State. *Journal of Bacteriology* **2013,** *195* (7), 1371.

116. Wade, K. C.; Benjamin, D. K., CHAPTER 37 - Clinical Pharmacology of Anti-Infective Drugs. In *Infectious Diseases of the Fetus and Newborn (Seventh Edition)*, Remington, J. S.; Klein, J. O.; Wilson, C. B.; Nizet, V.; Maldonado, Y. A., Eds. W.B. Saunders: Philadelphia, 2011; pp 1160-1211.

117. Hill, D.; Rose, B.; Pajkos, A.; Robinson, M.; Bye, P.; Bell, S.; Elkins, M.; Thompson, B.; MacLeod, C.; Aaron, S. D.; Harbour, C., Antibiotic susceptibilities of Pseudomonas aeruginosa isolates derived from patients with cystic fibrosis under aerobic, anaerobic, and biofilm conditions. *Journal of Clinical Microbiology* **2005,** *43* (10), 5085-5090.

118. Satlin, M. J.; Jenkins, S. G., 151 - Polymyxins. In *Infectious Diseases (Fourth Edition)*, Cohen, J.; Powderly, W. G.; Opal, S. M., Eds. Elsevier: 2017; pp 1285-1288.e2.

119. Hengzhuang, W.; Wu, H.; Ciofu, O.; Song, Z.; Hoiby, N., Pharmacokinetics/pharmacodynamics of colistin and imipenem on mucoid and nonmucoid Pseudomonas aeruginosa biofilms. *Antimicrob Agents Chemother* **2011,** *55* (9), 4469-74.

120. Stewart, P. S., Diffusion in biofilms. *Journal of Bacteriology* **2003,** *185* (5), 1485-1491.

121. Khan, Z. A.; Siddiqui, M. F.; Park, S., Current and Emerging Methods of Antibiotic Susceptibility Testing. *Diagnostics (Basel, Switzerland)* **2019,** *9* (2), 49.

122. Tacconelli, E.; Carrara, E.; Savoldi, A.; Harbarth, S.; Mendelson, M.; Monnet, D. L.; Pulcini, C.; Kahlmeter, G.; Kluytmans, J.; Carmeli, Y.; Ouellette, M.; Outterson, K.; Patel, J.; Cavaleri, M.; Cox, E. M.; Houchens, C. R.; Grayson, M. L.; Hansen, P.; Singh, N.; Theuretzbacher, U.; Magrini, N.; Aboderin, A. O.; Al-Abri, S. S.; Awang Jalil, N.; Benzonana, N.; Bhattacharya, S.; Brink, A. J.; Burkert, F. R.; Cars, O.; Cornaglia, G.; Dyar, O. J.; Friedrich, A. W.; Gales, A. C.; Gandra, S.; Giske, C. G.; Goff, D. A.; Goossens, H.; Gottlieb, T.; Guzman Blanco, M.; Hryniewicz, W.; Kattula, D.; Jinks, T.; Kanj, S. S.; Kerr, L.; Kieny, M.-P.; Kim, Y. S.; Kozlov, R. S.; Labarca, J.; Laxminarayan, R.; Leder, K.; Leibovici, L.; Levy-Hara, G.; Littman, J.; Malhotra-Kumar, S.; Manchanda, V.; Moja, L.; Ndoye, B.; Pan, A.; Paterson, D. L.; Paul, M.; Qiu, H.; Ramon-Pardo, P.; Rodríguez-Baño, J.; Sanguinetti, M.; Sengupta, S.; Sharland, M.; Si-Mehand, M.; Silver, L. L.; Song, W.; Steinbakk, M.; Thomsen, J.; Thwaites, G. E.; van der Meer, J. W. M.; Van Kinh, N.; Vega, S.; Villegas, M. V.; Wechsler-Fördös, A.; Wertheim, H. F. L.; Wesangula, E.; Woodford, N.; Yilmaz, F. O.; Zorzet, A., Discovery, research, and development of new antibiotics: the WHO priority list of antibiotic-resistant bacteria and tuberculosis. *The Lancet Infectious Diseases* **2018,** *18* (3), 318-327.

123. Hall, C. W.; Mah, T.-F., Molecular mechanisms of biofilm-based antibiotic resistance and tolerance in pathogenic bacteria. *FEMS Microbiology Reviews* **2017,** *41* (3), 276-301.

124. Bjarnsholt, T.; Ciofu, O.; Molin, S.; Givskov, M.; Høiby, N., Applying insights from biofilm biology to drug development — can a new approach be developed? *Nature Reviews Drug Discovery* **2013,** *12* (10), 791-808.

125. Martens, E.; Demain, A. L., The antibiotic resistance crisis, with a focus on the United States. *The Journal of Antibiotics* **2017,** *70* (5), 520-526.

126. Singh, P. K.; Schaefer, A. L.; Parsek, M. R.; Moninger, T. O.; Welsh, M. J.; Greenberg, E. P., Quorum-sensing signals indicate that cystic fibrosis lungs are infected with bacterial biofilms. *Nature* **2000,** *407* (6805), 762-764.

127. Forier, K.; Messiaen, A.-S.; Raemdonck, K.; Deschout, H.; Rejman, J.; De Baets, F.; Nelis, H.; De Smedt, S. C.; Demeester, J.; Coenye, T.; Braeckmans, K., Transport of nanoparticles in cystic fibrosis sputum and bacterial biofilms by single-particle tracking microscopy. *Nanomedicine* **2013,** *8* (6), 935-949.

128. Drenkard, E.; Ausubel, F. M., Pseudomonas biofilm formation and antibiotic resistance are linked to phenotypic variation. *Nature* **2002,** *416* (6882), 740-743.

129. Gellatly, S. L.; Hancock, R. E. W., Pseudomonas aeruginosa: new insights into pathogenesis and host defenses. *Pathogens and Disease* **2013,** *67* (3), 159-173.

130. Kerremans, J. J.; Verboom, P.; Stijnen, T.; Hakkaart-van Roijen, L.; Goessens, W.; Verbrugh, H. A.; Vos, M. C., Rapid identification and antimicrobial susceptibility testing reduce antibiotic use and accelerate pathogen-directed antibiotic use. *Journal of Antimicrobial Chemotherapy* **2008,** *61* (2), 428-435.

131. Matuschek, E.; Brown, D. F. J.; Kahlmeter, G., Development of the EUCAST disk diffusion antimicrobial susceptibility testing method and its implementation in routine microbiology laboratories. *Clinical Microbiology and Infection* **2014,** *20* (4), O255-O266.

132. Ceri, H.; Olson, M. E.; Stremick, C.; Read, R. R.; Morck, D.; Buret, A., The Calgary Biofilm Device: new technology for rapid determination of antibiotic susceptibilities of bacterial biofilms. *J Clin Microbiol* **1999,** *37* (6), 1771-6.

133. Moskowitz, S. M.; Foster, J. M.; Emerson, J.; Burns, J. L., Clinically Feasible Biofilm Susceptibility Assay for Isolates of *Pseudomonas aeruginosa* from Patients with Cystic Fibrosis. *Journal of Clinical Microbiology* **2004,** *42* (5), 1915.

134. Harrison, J. J.; Stremick, C. A.; Turner, R. J.; Allan, N. D.; Olson, M. E.; Ceri, H., Microtiter susceptibility testing of microbes growing on peg lids: a miniaturized biofilm model for high-throughput screening. *Nature Protocols* **2010,** *5* (7), 1236-1254.

135. Sondergaard, R. V.; Christensen, N. M.; Henriksen, J. R.; Kumar, E. K. P.; Almdal, K.; Andresen, T. L., Facing the Design Challenges of Particle-Based Nanosensors for

Metabolite Quantification in Living Cells. *Chemical Reviews* **2015,** *115* (16), 8344-8378.

136. Wang, C.; Li, X.; Zhang, F.; Vail, T.; Burton, J.; Bielska, B.; Li, S.; Milunic, D.; Bourdelle, P.; Vallejo, R.; Robinson, J. P.; Goldys, E. M.; Jin, D.; Shen, J.; Piper, J. A.; Jin, D. Y., Bioapplications and biotechnologies of upconversion nanoparticle-based nanosensors. *The Analyst* **2016,** *141* (12), 3601-3620.

137. Roussakis, E.; Li, Z.; Nichols, A. J.; Evans, C. L., Oxygen-Sensing Methods in Biomedicine from the Macroscale to the Microscale. *Angewandte Chemie International Edition* **2015,** *54* (29), 8340-8362.

138. Rong, G.; Kim, E. H.; Poskanzer, K. E.; Clark, H. A., A method for estimating intracellular ion concentration using optical nanosensors and ratiometric imaging. *Scientific Reports* **2017,** *7* (1), 10819.

139. Dubach, J. M.; Das, S.; Rosenzweig, A.; Clark, H. A., Visualizing sodium dynamics in isolated cardiomyocytes using fluorescent nanosensors. *Proc. Natl. Acad. Sci.* **2009,** *106* (38), 16145-16150.

140. Church, J.; Armas, S. M.; Patel, P. K.; Chumbimuni-Torres, K.; Lee, W. H., Development and Characterization of Needle-type Ion-selective Microsensors for in situ Determination of Foliar Uptake of Zn2+ in Citrus Plants. *Electroanalysis* **2018,** *30* (4), 626-632.

141. Cash, K. J.; Li, C.; Xia, J.; Wang, L. V.; Clark, H. A., Optical Drug Monitoring: Photoacoustic Imaging of Nanosensors to Monitor Therapeutic Lithium in Vivo. *ACS Nano* **2015,** *9* (2), 1692–1698.

142. Balaconis, M. K.; Clark, H. A., Biodegradable optode-based nanosensors for in vivo monitoring. *Anal. Chem.* **2012,** *84* (13), 5787-93.

143. Canovas, R.; Sanchez, S. P.; Parrilla, M.; Cuartero, M.; Crespo, G. A., Cytotoxicity Study of Ionophore-Based Membranes: Toward On Body and in Vivo Ion Sensing. *ACS Sensors* **2019,** *4* (9), 2524-2535.

144. Xie, X. J.; Zhai, J. Y.; Bakker, E., pH Independent Nano-Optode Sensors Based on Exhaustive Ion-Selective Nanospheres. *Analytical Chemistry* **2014,** *86* (6), 2853-2856.

145. Xie, X. J., Renovating the chromoionophores and detection modes in carrier-based ion-selective optical sensors. *Analytical and Bioanalytical Chemistry* **2016,** *408* (11), 2717-2725.

146. Du, X. F.; Yang, L. Y.; Hu, W. C.; Wang, R. J.; Zhai, J. Y.; Xie, X. J., A Plasticizer-Free Miniaturized Optical Ion Sensing Platform with Ionophores and Silicon-Based Particles. *Analytical Chemistry* **2018,** *90* (9), 5818-5824.

147. Arshad, F.; Pal, A.; Rahman, M. A.; Ali, M.; Khan, J. A.; Sk, M. P., Insights on the solvatochromic effects in N-doped yellow-orange emissive carbon dots. *New Journal of Chemistry* **2018,** *42* (24), 19837-19843.

148. Mei, S. L.; Wei, X.; Hu, Z.; Wei, C.; Su, D. L.; Yang, D.; Zhang, G. L.; Zhang, W. L.; Guo, R. Q., Amphipathic carbon dots with solvent-dependent optical properties and sensing application. *Optical Materials* **2019,** *89*, 224-230.

149. Zheng, M.; Li, Y.; Zhang, Y. J.; Xie, Z. G., Solvatochromic fluorescent carbon dots as optic noses for sensing volatile organic compounds. *Rsc Advances* **2016,** *6* (86), 83501-83504.

150. Zhou, J.; Liu, Z.; Li, F., Upconversion nanophosphors for small-animal imaging. *Chemical Society Reviews* **2012,** *41* (3), 1323-1349.

151. Liang, T.; Li, Z.; Song, D.; Shen, L.; Zhuang, Q.; Liu, Z., Modulating the Luminescence of Upconversion Nanoparticles with Heavy Metal Ions: A New Strategy for Probe Design. *Analytical Chemistry* **2016,** *88* (20), 9989-9995.

152. Peng, J.; Xu, W.; Teoh, C. L.; Han, S.; Kim, B.; Samanta, A.; Er, J. C.; Wang, L.; Yuan, L.; Liu, X.; Chang, Y. T., High-efficiency in vitro and in vivo detection of Zn2+ by dye-assembled upconversion nanoparticles. *Journal of the American Chemical Society* **2015,** *137* (6), 2336-2342.

153. Nagai, A.; Miller, J. B.; Kos, P.; Elkassih, S.; Xiong, H.; Siegwart, D. J., Tumor Imaging Based on Photon Upconversion of Pt(II) Porphyrin Rhodamine Co-modified NIR Excitable Cellulose Enhanced by Aggregation. *ACS Biomaterials Science & Engineering* **2015,** *1*, 1206-1210.

154. Zhu, X.; Su, Q.; Feng, W.; Li, F., Anti-Stokes shift luminescent materials for bio-applications. *Chem. Soc. Rev.* **2017,** *46* (4), 1025-1039.

155. Zhou, J.; Liu, Q.; Feng, W.; Sun, Y.; Li, F., Upconversion Luminescent Materials: Advances and Applications. *Chemical Reviews* **2015,** *115* (1), 395-465.

156. Xie, L. X.; Qin, Y.; Chen, H. Y., Polymeric Optodes Based on Upconverting Nanorods for Fluorescent Measurements of pH and Metal Ions in Blood Samples. *Analytical Chemistry* **2012,** *84* (4), 1969-1974.

157. Wu, J.; Qin, Y., Polymeric optodes based on upconverting nanorods for fluorescence measurements of Pb2+ in complex samples. *Sensors and Actuators B-Chemical* **2014,** *192*, 51-55.

158. Chen, G.; Qiu, H.; Prasad, P. N.; Chen, X., Upconversion Nanoparticles: Design, Nanochemistry, and Applications in Theranostics. *Chemical Reviews* **2014,** *114* (10), 5161-5214.

159. Ge, X.; Sun, L.; Ma, B.; Jin, D.; Dong, L.; Shi, L.; Li, N.; Chen, H.; Huang, W., Simultaneous realization of Hg2+ sensing, magnetic resonance imaging and upconversion luminescence in vitro and in vivo bioimaging based on hollow mesoporous silica coated UCNPs and ruthenium complex. *Nanoscale* **2015,** *7* (33), 13877-13887.

160. Xie, L. X.; Qin, Y.; Chen, H. Y., Direct Fluorescent Measurement of Blood Potassium with Polymeric Optical Sensors Based on Upconverting Nanomaterials. *Anal. Chem.* **2013,** *85* (5), 2617-2622.

161. Simon, Y. C.; Weder, C., Low-power photon upconversion through triplet-triplet annihilation in polymers. *Journal of Materials Chemistry* **2012,** *22* (39), 20817-20830.

162. Liu, Q.; Yin, B.; Yang, T.; Yang, Y.; Shen, Z.; Yao, P.; Li, F., A general strategy for biocompatible, high-effective upconversion nanocapsules based on triplet-triplet annihilation. *Journal of the American Chemical Society* **2013,** *135* (13), 5029-5037.

163. Wohnhaas, C.; Friedemann, K.; Busko, D.; Landfester, K.; Baluschev, S.; Crespy, D.; Turshatov, A., All Organic Nanofibers As Ultralight Versatile Support for Triplet-Triplet Annihilation Upconversion. *Acs Macro Letters* **2013,** *2* (5), 446-450.

164. Liu, Q.; Yang, T.; Feng, W.; Li, F., Blue-emissive upconversion nanoparticles for low-power-excited bioimaging in vivo. *Journal of the American Chemical Society* **2012,** *134* (11), 5390-5397.

165. Kwon, O. S.; Song, H. S.; Conde, J.; Kim, H. I.; Artzi, N.; Kim, J. H., Dual-color emissive upconversion nanocapsules for differential cancer bioimaging in vivo. *ACS Nano* **2016,** *10* (1), 1512-1521.

166. Liu, Y.; Su, Q.; Zou, X.; Chen, M.; Feng, W.; Shi, Y.; Li, F., Near-infrared: In vivo bioimaging using a molecular upconversion probe. *Chemical Communications* **2016,** *52* (47), 7466-7469.

167. Tian, B.; Wang, Q.; Su, Q.; Feng, W.; Li, F., In-vivo biodistribution and toxicity assessment of triplet-triplet annihilation-based upconversion nanocapsules. *Biomaterials* **2017,** *112*, 10-19.

168. Askes, S. H. C.; Leeuwenburgh, V. C.; Pomp, W.; Arjmandi-Tash, H.; Tanase, S.; Schmidt, T.; Bonnet, S., Water-dispersible silica-coated upconverting liposomes: can a thin silica layer protect TTA-UC against oxygen quenching? *ACS Biomaterials Science & Engineering* **2017**, acsbiomaterials.6b00678-acsbiomaterials.6b00678.

169. Wohnhaas, C.; Mailänder, V.; Dröge, M.; Filatov, M. A.; Busko, D.; Avlasevich, Y.; Baluschev, S.; Miteva, T.; Landfester, K.; Turshatov, A., Triplet-triplet annihilation upconversion based nanocapsules for bioimaging under excitation by red and deep-red light. *Macromolecular Bioscience* **2013,** *13* (10), 1422-1430.

170. Wohnhaas, C.; Turshatov, A.; Mailänder, V.; Lorenz, S.; Baluschev, S.; Miteva, T.; Landfester, K., Annihilation Upconversion in Cells by Embedding the Dye System in Polymeric Nanocapsules. *Macromolecular Bioscience* **2011,** *11* (6), 772-778.

171. Borisov, S. M.; Larndorfer, C.; Klimant, I., Triplet-triplet annihilation-based anti-stokes oxygen sensing materials with a very broad dynamic range. *Advanced Functional Materials* **2012,** *22* (20), 4360-4368.

172. Sahari, A.; Ruckh, T. T.; Hutchings, R.; Clark, H. A., Development of an Optical Nanosensor Incorporating a pH-Sensitive Quencher Dye for Potassium Imaging. *Anal. Chem.* **2015,** *87* (21), 10684--10687.

173. Ferris, M. S.; Behr, M. R.; Cash, K. J., An ionophore-based persistent luminescent 'Glow Sensor' for sodium detection. *RSC Advances* **2019,** *9* (56), 32821-32825.

174. Billingsley, K.; Balaconis, M. K.; Dubach, J. M.; Zhang, N.; Lim, E.; Francis, K. P.; Clark, H. A., Fluorescent Nano-Optodes for Glucose Detection. *Analytical Chemistry* **2010,** *82* (9), 3707-3713.

175. Dubach, J. M.; Balaconis, M. K.; Clark, H. A., Fluorescent Nanoparticles for the Measurement of Ion Concentration in Biological Systems. *J. Visualized Exp.* **2011,** (53), 1-5.

176. Islangulov, R. R.; Lott, J.; Weder, C.; Castellano, F. N., Noncoherent low-power upconversion in solid polymer films. *Journal of the American Chemical Society* **2007,** *129* (42), 12652-12653.

177. Monguzzi, A.; Tubino, R.; Meinardi, F., Upconversion-induced delayed fluorescence in multicomponent organic systems: Role of Dexter energy transfer. *Physical Review B - Condensed Matter and Materials Physics* **2008,** *77* (15).

178. Monguzzi, A.; Frigoli, M.; Larpent, C.; Tubino, R.; Meinardi, F., Low-power-photon up-conversion in dual-dye-loaded polymer nanoparticles. *Advanced Functional Materials* **2012,** *22* (1), 139-143.

179. Keivanidis, P. E.; Baluschev, S.; Miteva, T.; Nelles, G.; Scherf, U.; Yasuda, A.; Wegner, G., Up-Conversion Photoluminescence in Polyfluorene Doped with Metal(II)–Octaethyl Porphyrins. *Advanced Materials* **2003,** *15* (24), 2095-2098.

180. Galyean, A.; Behr, M.; Cash, K., Ionophore-based optical nanosensors incorporating hydrophobic carbon dots and a pH-sensitive quencher dye for sodium detection. *Analyst* **2018,** *143* (2), 458-465.

181. Shortreed, M.; Dourado, S.; Kopelman, R., Development of a fluorescent optical potassium-selective ion sensor with ratiometric response for intracellular applications. *Sensors and Actuators B* **1997,** *38-39*, 8-12.

182. Zhai, J. Y.; Xie, X. J.; Bakker, E., Solvatochromic Dyes as pH-Independent Indicators for Ionophore Nanosphere-Based Complexometric Titrations. *Analytical Chemistry* **2015,** *87* (24), 12318-12323.

183. Xie, X. J.; Szilagyi, I.; Zhai, J. Y.; Wang, L.; Bakker, E., Ion-Selective Optical Nanosensors Based on Solvatochromic Dyes of Different Lipophilicity: From Bulk Partitioning to Interfacial Accumulation. *Acs Sensors* **2016,** *1* (5), 516-520.

184. Marsico, F.; Turshatov, A.; Pekoz, R.; Avlasevich, Y.; Wagner, M.; Weber, K.; Donadio, D.; Landfester, K.; Baluschev, S.; Wurm, F. R., Hyperbranched Unsaturated Polyphosphates as a Protective Matrix for Long-Term Photon Upconversion in Air. *Journal of the American Chemical Society* **2014,** *136* (31), 11057-11064.

185. Mistlberger, G.; Crespo, G. A.; Bakker, E., Ionophore-Based Optical Sensors. *Annual Review of Analytical Chemistry* **2014,** *7* (1), 483-512.

186. Peulen, T.-O.; Wilkinson, K. J., Diffusion of Nanoparticles in a Biofilm. *Environmental Science & Technology* **2011,** *45* (8), 3367-3373.

APPENDIX A

SUPPLEMENTARY INFORMATION FOR CHAPTER 3

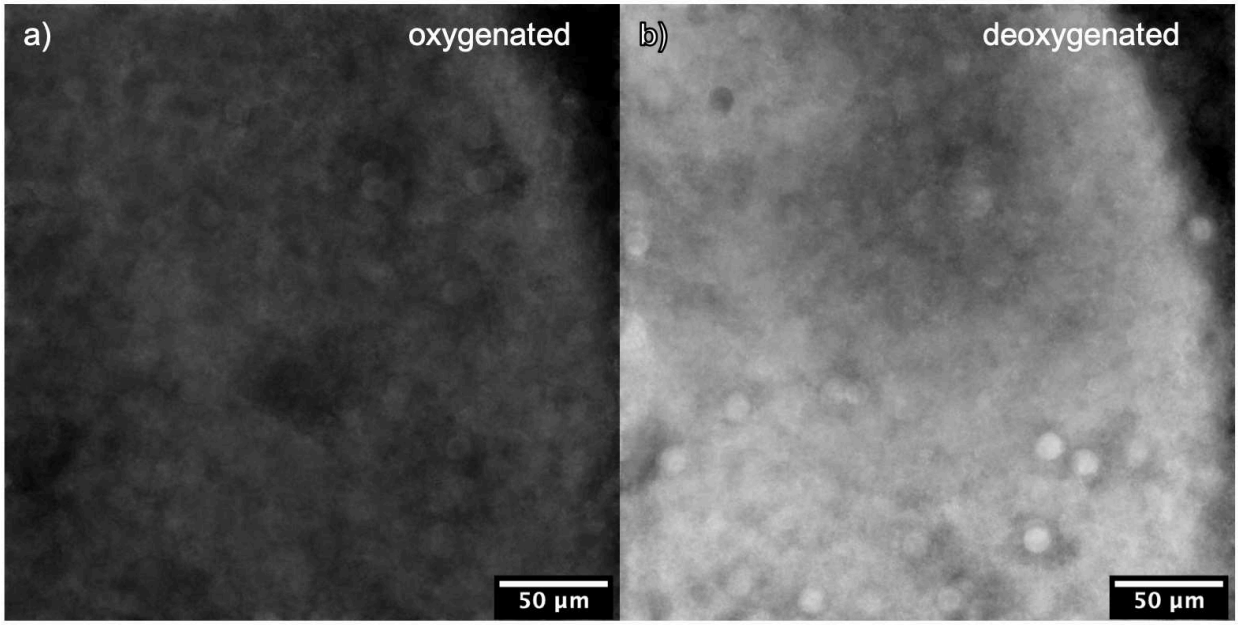

Figure A.1 O_2NS in an alginate hydrogel a) before and b) after deoxygenation with glucose and glucose oxidase. The ratiometric intensity increases as the oxygen concentration decreases. Image is of the edge of a circular hydrogel in PBS containing a) 10mM glucose and b) 10mM glucose + 2 IU/mL glucose oxidase.

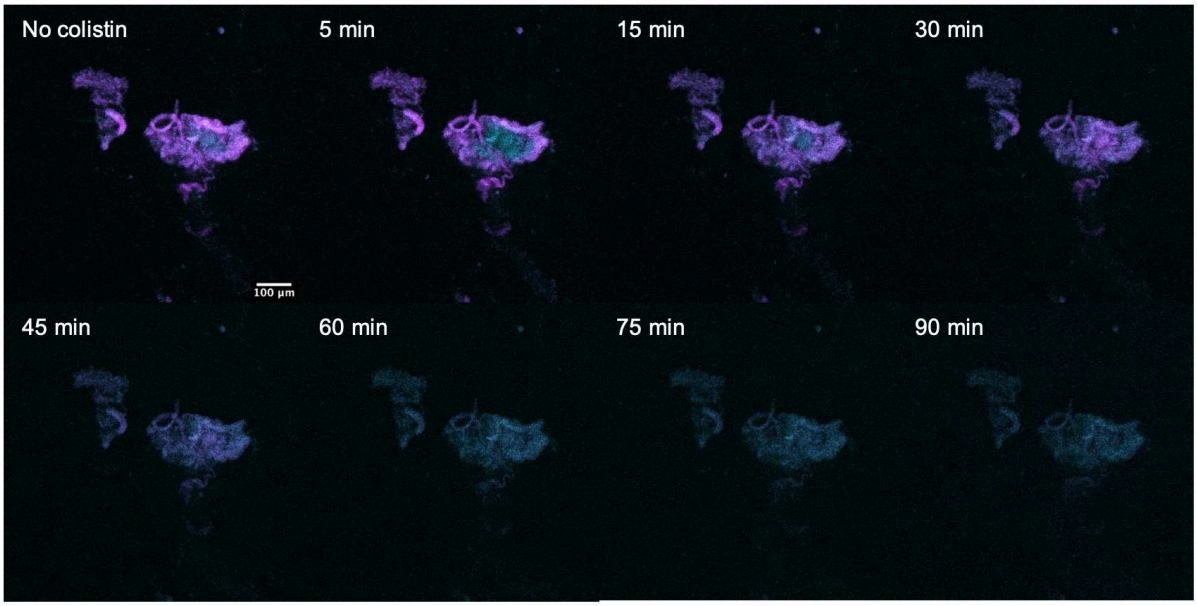

Figure A.2 Raw microscopy images of representative PAO1 biofilm analyzed in Figures 4, 5, and 6. These images are Z-projections of the 3-dimensional stack containing 2 channels. The pink channel is the O_2-sensitive PtTFPP channel and the cyan channel is the ratiometric DiA channel. Note that after addition of colistin, the PtTFPP channel decreases and is undetectable by eye by 60 min, while the DiA channel does not noticeably decrease until 90 min (presumably due to photobleaching after 90 min of continuous laser excitation).

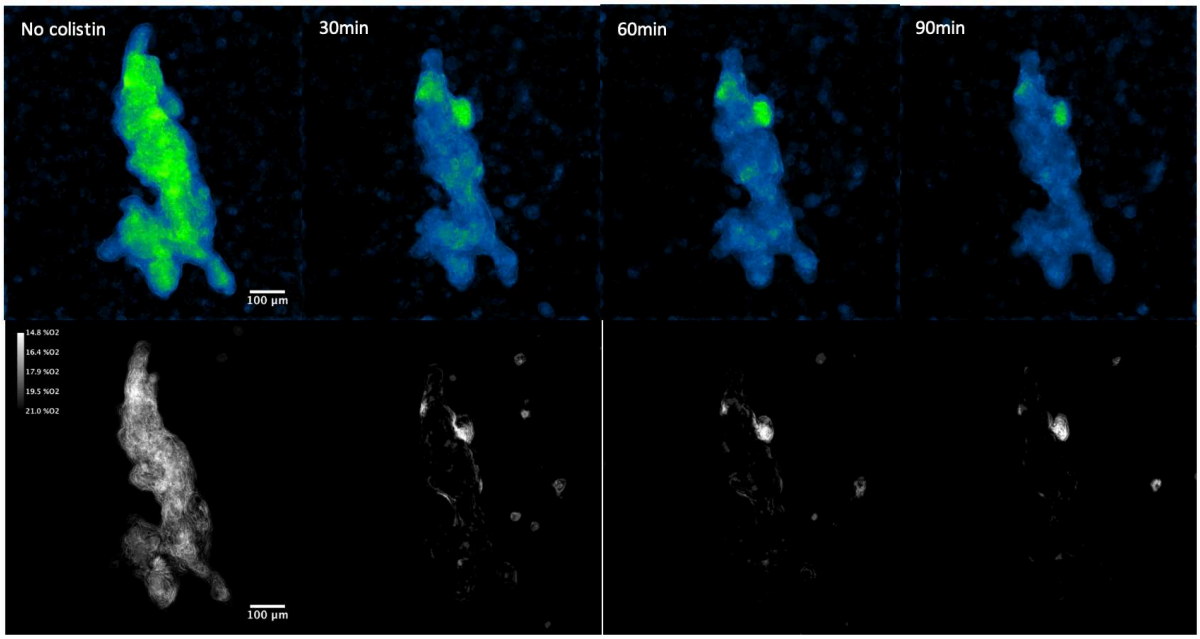

Figure A.3 Z-projections of average ratiometric intensity of O_2NS in CS1 over 90min after addition of colistin sulfate. Z-projections of average oxygen concentration for the same images.

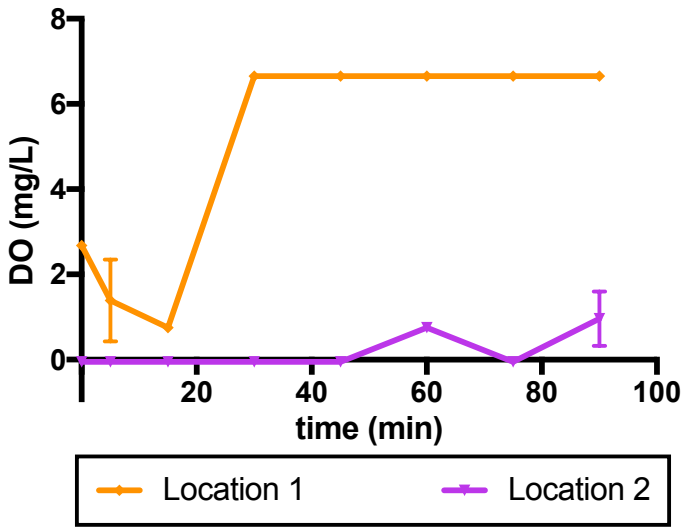

Figure A.4 Local oxygen concentration of two locations within the biofilm shown in Figure A.3 highlighting spatial variations in response to colistin.

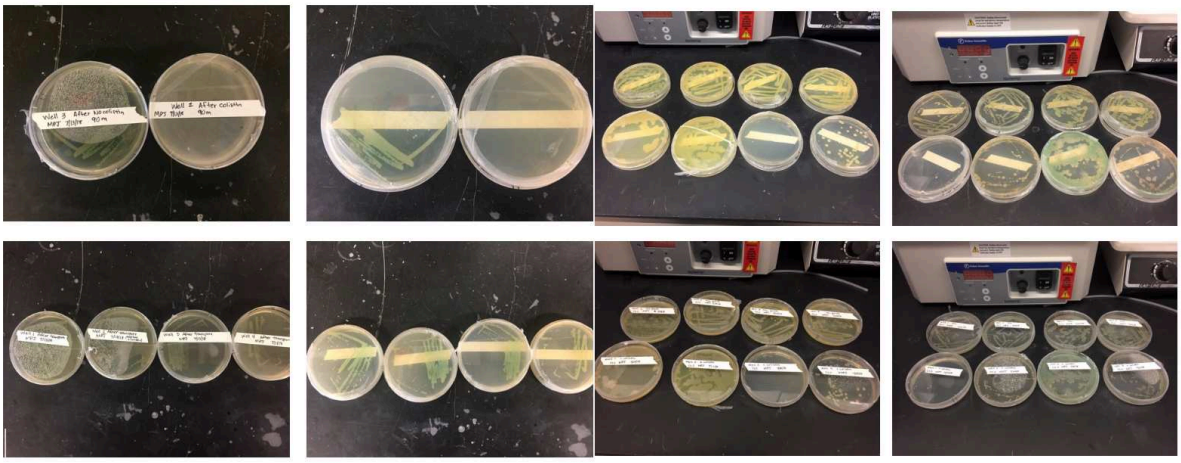

Figure A.5 PAO1 biofilm samples were plated before and after exposure to colistin sulfate. Lack of growth and color change in agar (due to pyocyanin presence) indicate antibiotic effectiveness. Clinical samples were also plated before and after exposure to colistin sulfate. Growth and color change in CS2 and CS3 are similar before and after exposure.

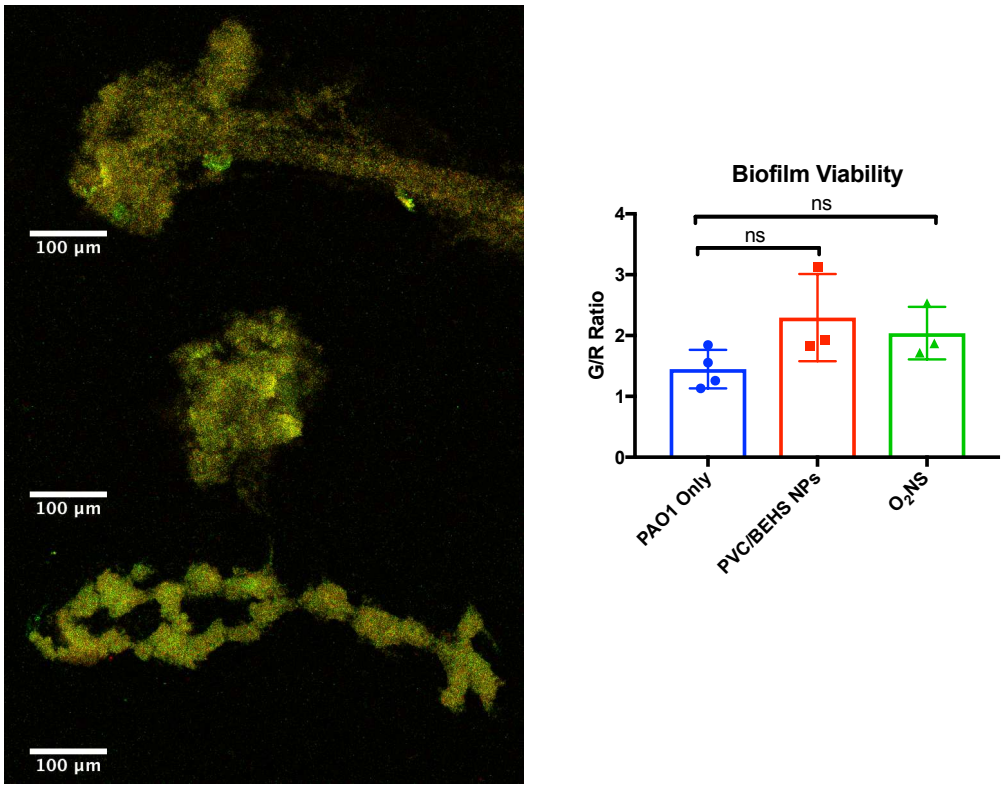

Figure A.6 Live/Dead Viability Staining of biofilms containing a) no nanosensors, b) polymeric nanoparticles without dye components, and c) oxygen nanosensors.

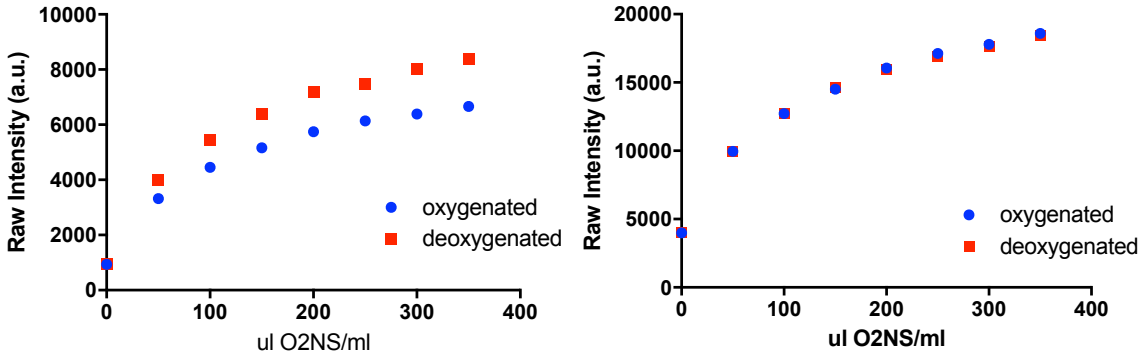

Figure A.7 Both the oxygen-sensitive PtTFPP (left) and reference DiA (right) signals exhibit concentration-dependent fluorescence intensity in LB media.

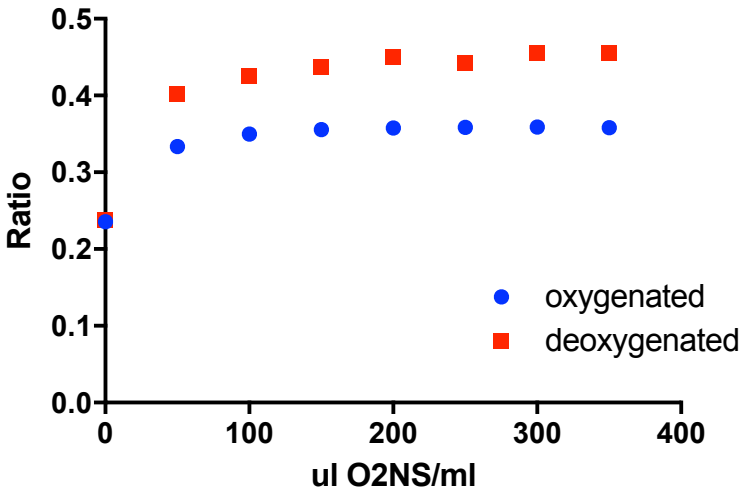

Figure A.8 Unlike the raw fluorescence signals, the ratio of the PtTFPP signal and the DiA signal (PtTFPP/DiA) is stable and not dependent on concentration of sensors in the media.

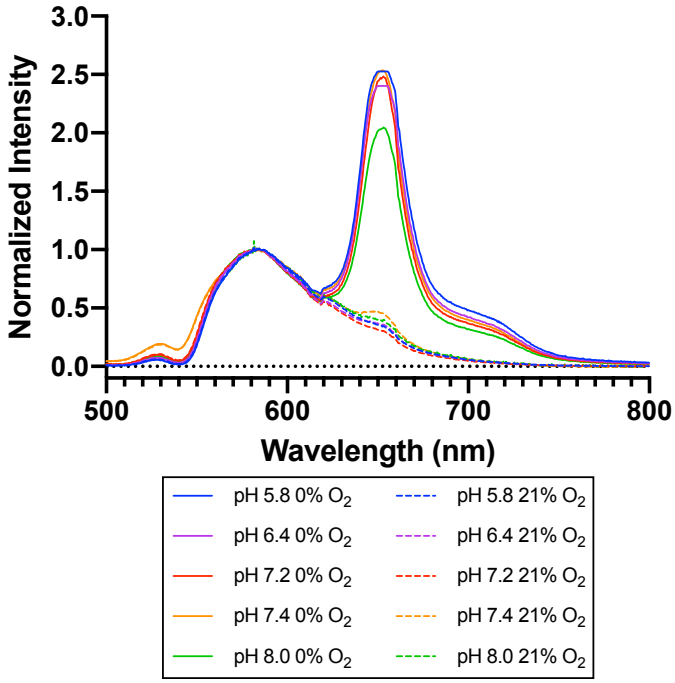

Figure A.9 Spectra of O_2NS in phosphate buffered solutions of varying pH at minimum and maximum oxygen concentrations. pH appears to have a minimal effect on the sensors brightness and response.

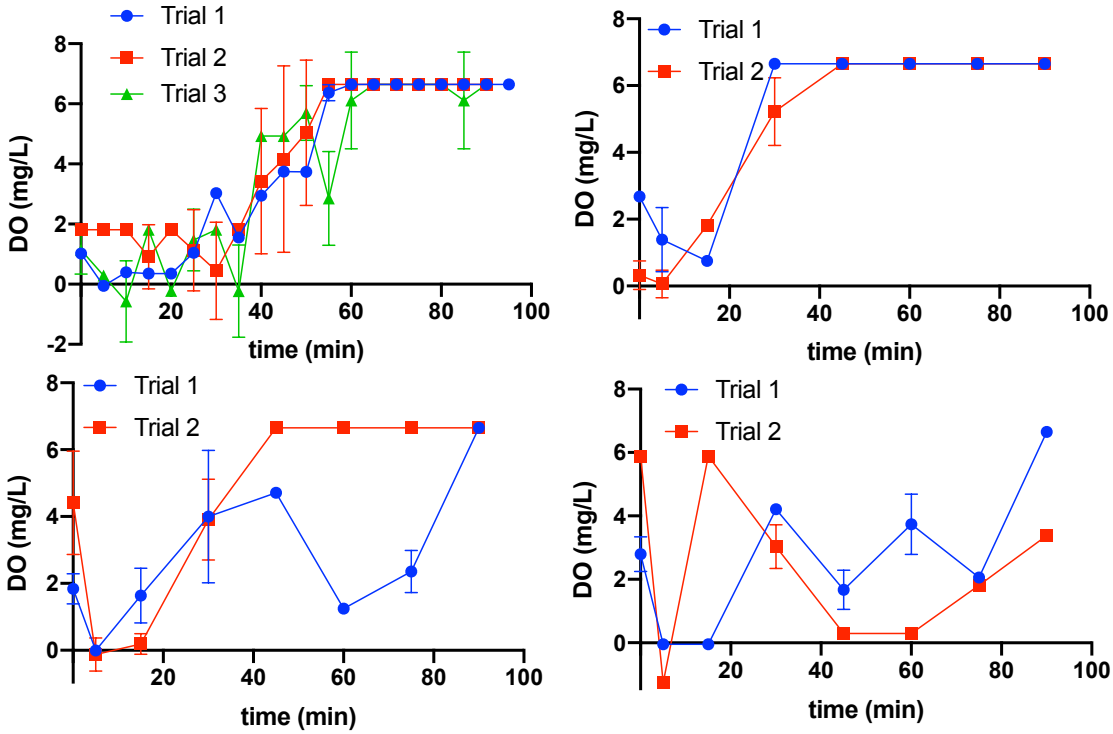

Figure A.10 Biological replicates of time-lapse data for a) PAO1 (n = 3), b) clinical strain 1 (n = 2), c) clinical strain 2 (n = 2), and d) clinical strain 3 (n = 2) presented in Figure 7. Error bars represent standard error of n = 9 pixels surrounding chosen location.

APPENDIX B

SUPPLEMENTARY INFORMATION FOR CHAPTER 5

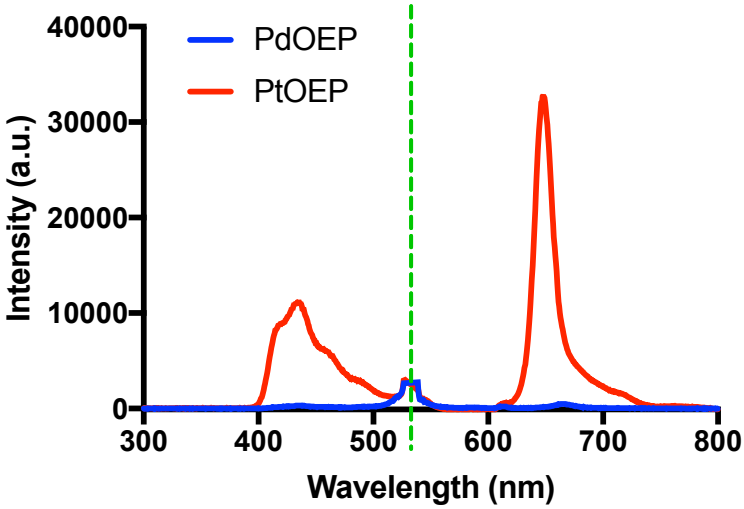

Figure B.1 Upconversion luminescence in PVC/plasticizer films containing either PtOEP and DPA or PdOEP and DPA. Both were excited at 532nm (dashed green line). PtOEP/DPA produced much more intense fluorescence in comparison to PdOEP/DPA.

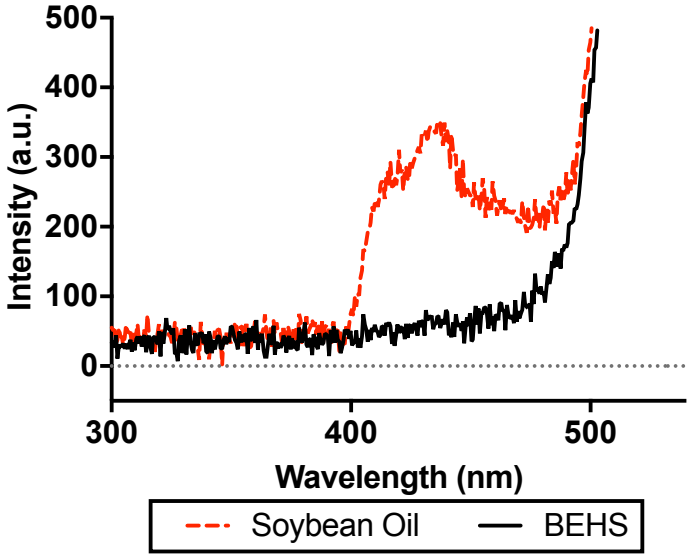

Figure B.2 Emission spectra for nanoparticles that utilize either soybean oil or BEHS as the plasticizer. Excitation at 532nm produces upconversion luminescence in nanoparticles plasticized with soybean oil, an oxygen scavenger, without purging the solution using N_2.

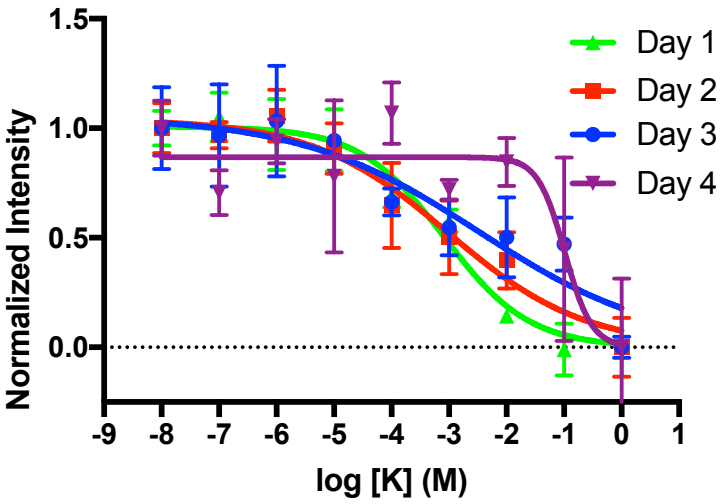

Figure B.3 Nanosensor response to K^+ over 4 days.

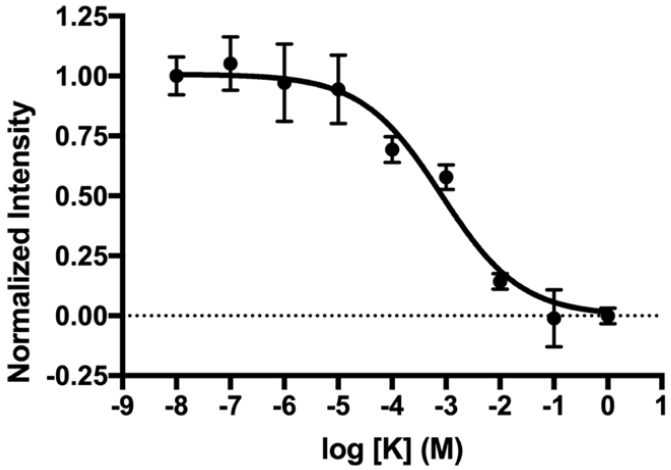

Figure B.4 Normalized fluorescence intensity of UCNS response to KCl solution buffered in HEPES/Tris (pH = 7.4). UCNS solutions were deoxygenated with N_2 for 20 minutes prior to measurement.

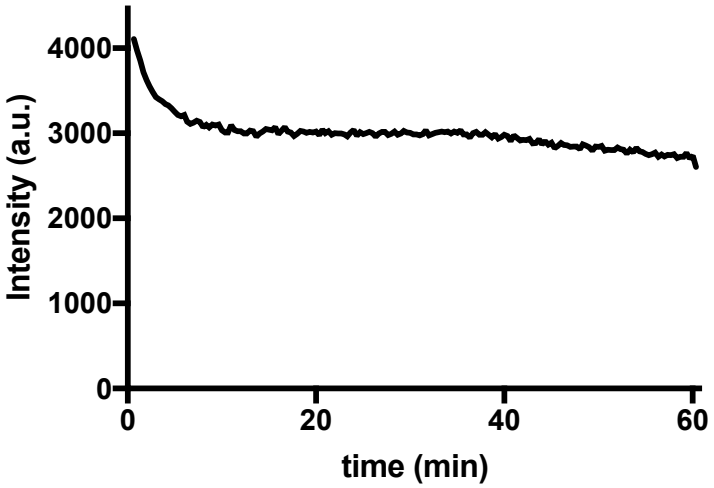

Figure B.5 Fluorescence intensity of UCNS over 60 minutes of continuous 532nm laser excitation (n=3). Image is presented here without error bars for clarity, but error bars representing SD are included in Figure B.6. Photostability of the UCNS was determined based on raw fluorescence intensity over 60 minutes when exposed to a 5mW cw 532nm laser. Measurements were taken every 20 seconds. The upconversion signal stabilizes after ~10 minutes demonstrating suitable photostability.

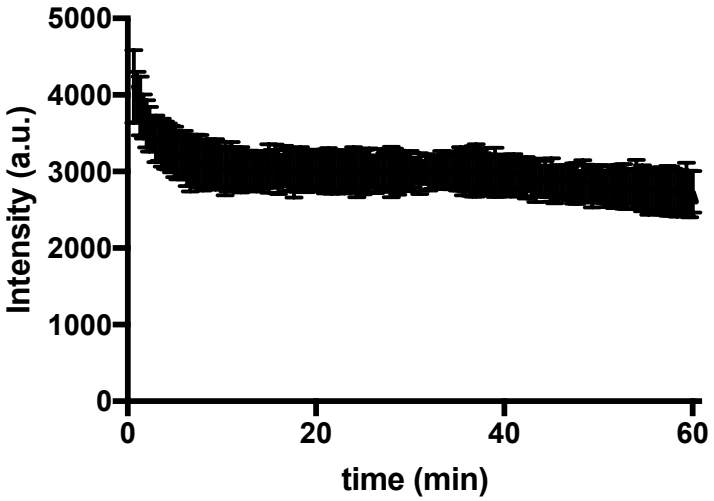

Figure B.6 Photostability of UCNS over 60 minutes of continuous laser excitation, error bars included (n = 3). Error bars represent standard deviation.

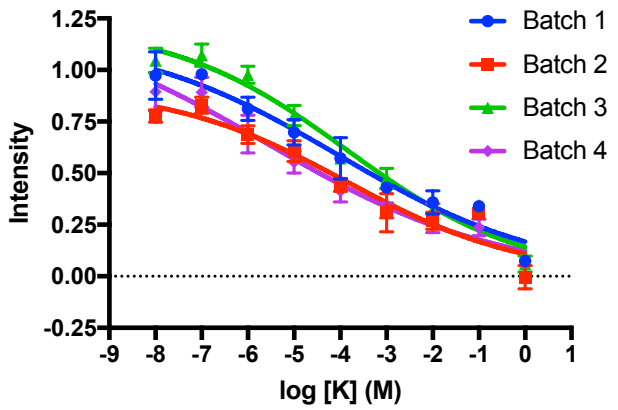

Figure B.7 Batch-to-batch variability of UCNS. Each batch was produced from the same initial optode mixture.

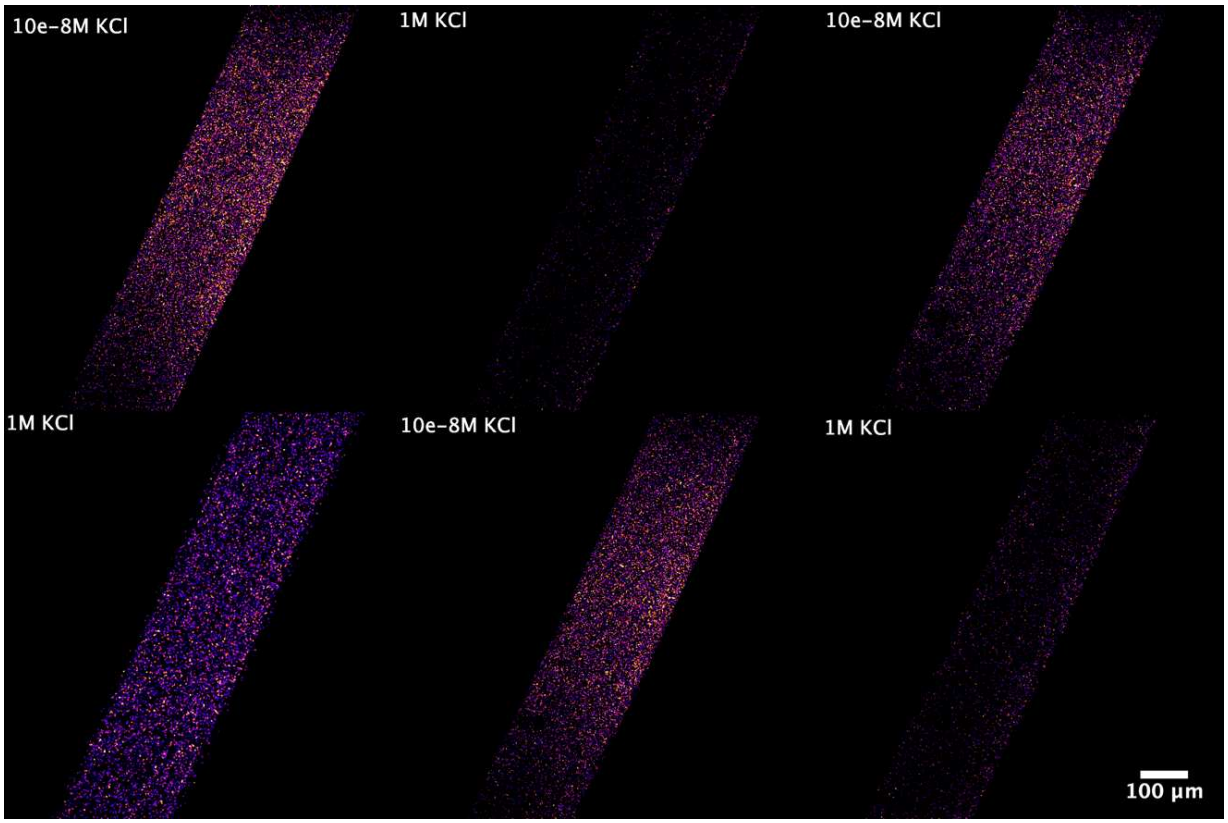

Figure B.8 Confocal microscopy images of UCNS in a microdialysis tube under repeated cycles of high and low potassium solutions.

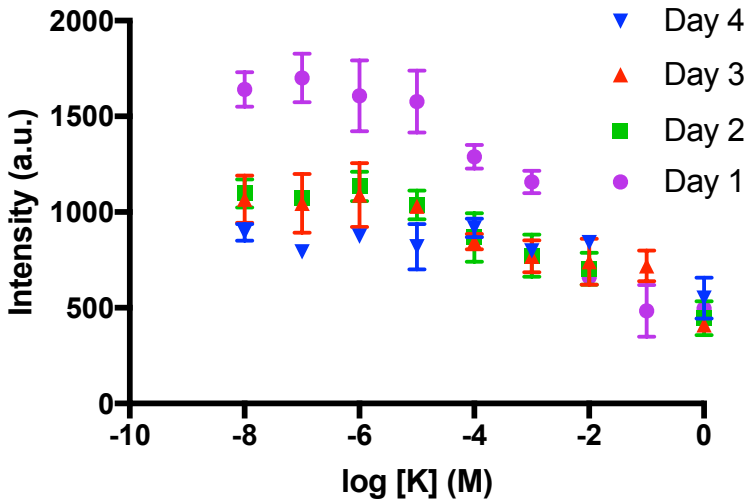

Figure B.9 Raw intensity lifetime data.

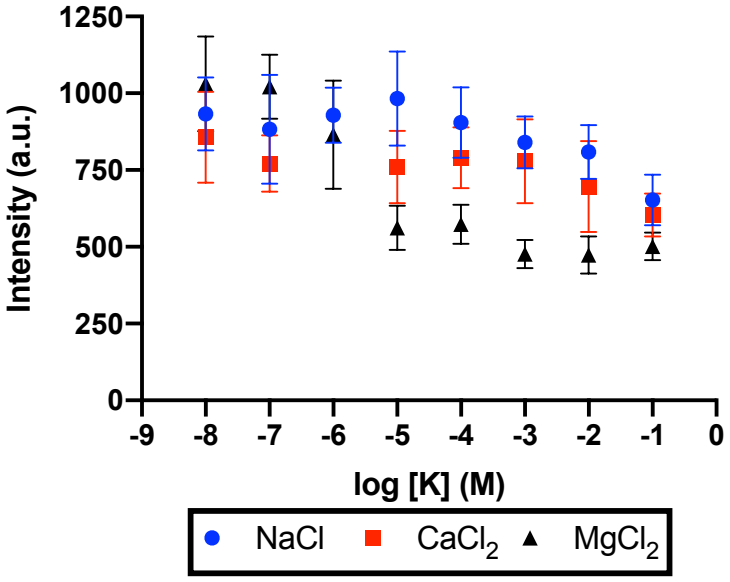

Figure B.10 Raw selectivity data.

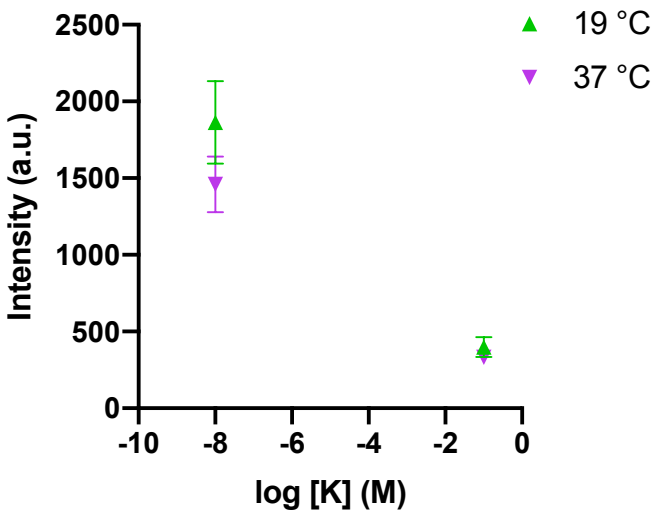

Figure B.11 Temperature sensitivity data. Increased temperatures appear to decrease the TTA-UC fluorescence at low concentrations of K^+. However, there is no significant difference between the fluorescent intensity at high concentrations of K^+ as the signal is already fully gated by the Blueberry dye.

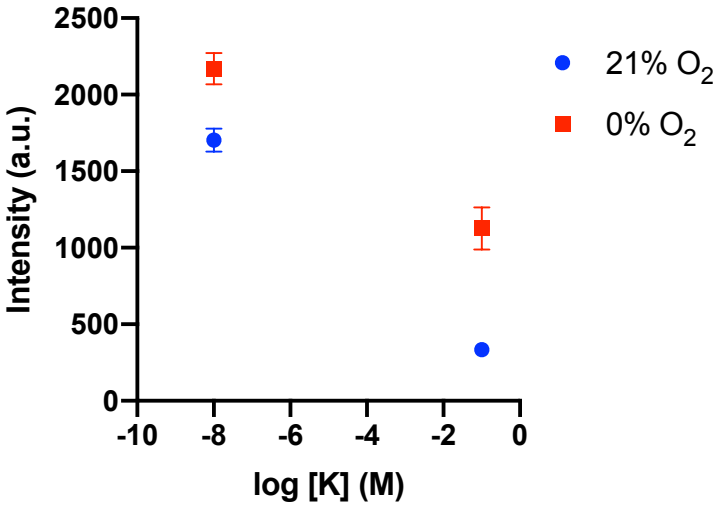

Figure B.12 Oxygen sensitivity data.